EXPERIMENTAL CHARACTERIZATION OF ROUGHNESS AND FLOW INJECTION EFFECTS IN A HIGH REYNOLDS NUMBER TURBULENT CHANNEL

THESIS

A thesis submitted in partial fulfillment
of the requirements for the degree of
Master of Science in Mechanical Engineering in the
College of Engineering at the University of Kentucky

By

Mark A. Miller

University of Kentucky

Director: Dr. Sean C.C. Bailey, Professor of Mechanical Engineering

Lexington, Kentucky

2013

ABSTRACT OF THESIS

EXPERIMENTAL CHARACTERIZATION OF ROUGHNESS AND FLOW INJECTION EFFECTS IN A HIGH REYNOLDS NUMBER TURBULENT CHANNEL

A turbulent channel flow was used to study the scaling of the combined effects of roughness and flow injection on the mean flow and turbulence statistics of turbulent plane Poiseuille flow. It was found that the additional momentum injected through the rough surface acted primarily to enhance the roughness effects and, with respect to the mean flow, blowing produced similar mean flow effects as increasing the roughness height. This was not found to hold for the turbulence statistics, as a departure from Townsend's hypothesis was seen. Instead, the resulting outer-scaled streamwise Reynolds stress for cases with roughness and blowing deviated significantly from the roughness only condition well throughout the inner and outer layers. Investigation into this phenomena indicated that suppression of the large-scale motions due to blowing may have been contributing to this deviation.

KEYWORDS: Turbulence, Flow Injection,
High-Reynolds Number, Surface Roughness, Channel Flows

Mark A. Miller

July 23, 2013

EXPERIMENTAL CHARACTERIZATION OF ROUGHNESS AND FLOW INJECTION EFFECTS IN A HIGH REYNOLDS NUMBER TURBULENT CHANNEL

By

Mark A. Miller

Dr. Sean C.C. Bailey
Director of Thesis

Dr. James M. McDonough
Director of Graduate Studies

July 23, 2013

ACKNOWLEDGMENTS

I would like to thank my mother and father, who have been a constant source of inspiration, guidance, and support throughout my life.

I would also like to thank my advisor, Dr. Bailey who has provided me with opportunities to challenge and develop myself as a researcher over the past two years.

There are also numerous others who also assisted me along the way. The very knowledgeable Herb Mefford who provided me with assistance when building new contraptions for the lab. Also my lab mates who were always willing to have an extended coffee break.

Lastly, I would like to acknowledge the groups who financially supported my two years of work, NASA Office of the Chief Technologist Space Technology Research Fellowship (grant number NNX12AN20H) and Commonwealth of Kentucky funding in association with a NASA EPSCoR award (grant number NNX10AV39A).

TABLE OF CONTENTS

LIST OF TABLES

LIST OF FIGURES

Nomenclature

$\Delta k_x \phi_{uu}^+$ Difference between two pre-multiplied power spectral density values, scaled with viscous units

Δp Pressure drop across rough surface used to calculate pressure loss coefficient

ΔU^+ Roughness function for rough-wall turbulent flow

δ Outer-flow length scale

δ^+ Viscous length

$\dot{V}_{inj}$ Flow rate of gas injected through rough surface

ℓ Hot-wire probe sensing length

ℓ^+ Hot-wire probe sensing length scaled with viscous units

κ von Kármán constant for the log law of the wall

λ Streamwise wavelength

λ_{2D} Two-dimensional roughness density

λ_{3D} Three-dimensional roughness density

$\langle U \rangle$ Area-averaged or bulk velocity

ν Kinematic viscosity

$\overline{u^2}$ Time-averaged velocity fluctuations

$\overline{u^4}$ Fourth-order velocity variance

$\overline{u^3}$ Third-order velocity variance

$\overline{U}$ Time-averaged Velocity

$\overrightarrow{V}$ Velocity vector in Cartesian space

ϕ_{uu} Streamwise power spectral density

ϕ_{uu}^+ Streamwise power spectral density scaled with viscous units

ρ Density

τ_w Wall shear stress

A Horizontal area of roughness element group

A_i Surface areas of control volume with $i \quad \forall \quad i = 1, 2, 3, 4$

B Additive constant for the log law of the wall

$BR\%$ Ratio of injected gas velocity to the maximum measured channel velocity expressed as a percent

BR Ratio of the injected gas velocity to the maximum measured channel velocity

$C(k^+, L_i^+)$ Integration term for the law of the wall in turbulent, rough-walled flow

C_f Coefficient of friction based on bulk velocity

$C_{f_{blowing}}$ Coefficient of friction corrected for blowing effects

D Pipe diameter

d Diameter of hot-wire probe sensing element

f Streamwise frequency

$F(\eta)$ Functional form of the velocity dependency in the outer-layer

F_u Flatness or kurtosis factor

F_x Forces in the streamwise direction

$G(Y^+, k^+, L_i^+)$ Functional form of the inner-scaled velocity dependency in the near-wall region

h Channel half-height

k Roughness height

k^+ Roughness Reynolds number

k_s Equivalent sand-grain roughness height

k_s^+ Sand-grain roughness Reynolds number

$k_x\phi_{uu}$ Pre-multiplied streamwise power spectral density

k_x Streamwise wavenumber

$K_{roughness}$ Pressure loss coefficient for rough surface

L_i Relevant roughness length scales other than roughness height

L_x Roughness characteristic length in the streamwise direction

L_z Roughness characteristic length in the spanwise direction

n Number of roughness elements in horizontal area A

P_i Pressure forces on control volume with $i \quad \forall \quad i = 1, 2$

Re	Reynolds number
Re_b	Bulk Reynolds number based on the area-averaged velocity
S_u	Skewness factor
T	Measurement acquisition time
$u(t)$	Time-varying velocity
U^+	Mean velocity scaled with viscous units
$u^{'}$	Time-varying velocity fluctuations
u^{2+}	Time-averaged Reynolds stress
U_τ	Friction Velocity
U_m	Maximum velocity in channel
U_∞	Free-stream velocity
U_{cl}	Velocity at geometric centerline of channel
U_{inj}	Velocity of gas injected through rough surface by blowing rig
w	Width of control volume
x	Streamwise direction, measured from inlet of test section
Y	Wall-normal direction minus roughness zero plane displacement
y	Wall-normal direction, measured normal from wall location of measurements
Y^+	Wall-normal direction minus the zero plane displacement and scaled with viscous units
y^+	Wall-normal direction scaled with viscous units
y_0	Zero-plane displacement due to roughness
y_h	Hot-wire home position
y_m	Location of maximum streamwise velocity
y_s	Hot-wire safe location relative to rough wall
y_{m_i}	Location of maximum streamwise velocity at control surface index $i \quad \forall \quad i = 1, 2$
u^{3+}	Third-order velocity variance scaled with viscous units
u^{4+}	Fourth-order velocity variance scaled with viscous units
L	Outer length scale

Chapter 1

Introduction

It is important to expand our knowledge base of turbulent flow behavior, because despite over a century of work in turbulent flows it is still considered the "last unsolved mystery of classical mechanics". Unlike laminar flow, no current complete analytical theory exists for turbulent flow and it is therefore much more difficult to study. It is a commonly held belief that the Navier-Stokes equations contain the solutions to turbulent flow, but numerical methods to completely resolve these highly non-linear equations are still in their infancy. This is particularly true for flows with high Reynolds number where the separation of physical and temporal scales introduces significant challenges in fully resolving all relevant scales. It is therefore of vast importance to continue to develop our understanding of turbulent flows by combining the best numerical simulations with new, high-Reynolds number turbulent flow studies. This will allow for new insight into previously unexplored phenomena and with many applications of industrial and research interests, it would appear that fundamental turbulence research is full of potential benefits.

As discussed in the following section, the work in this thesis is concerned with application of roughness and flow injection boundary conditions to a turbulent flow. A potential application of this work is the fluid-mechanical environment of an ablative thermal protection system (TPS), or heat shield. These ablative TPS are used on re-entry vehicles to protect the cargo of a space-faring capsule upon re-entry to a planet's atmosphere. The aero-heating environment experienced by these heat shields is extreme, and presents many challenges to the designer of a TPS. Complications arise from the broad range of flow conditions the craft undergoes during re-entry, from the non-continuum flow in the outer atmosphere, through a hypersonic, high-heating environment, all the way to subsonic speeds near the earth's surface. It is these

difficulties that make modeling such flow fields a complex and expensive task. To aid in our understanding of these flows, it is preferable to break the problem down into manageable problems. For the purposes of this thesis, we have focused on the near-wall effects of roughness of the heat shield and flow injection due to ablation gases. Heat-shield roughness is commonly the result of removal of material from the heat-shield itself due to charring of the surface and mechanical erosion through particle spallation, both of which cause drastic increases in the heat flux to the surface and must be accounted for in any modeling effort. However, current turbulence models are poor at capturing the effects of an arbitrary surface roughness and in the case of TPS design, a simple augmentation factor is usually employed which is empirically derived based on the expected roughness geometry during flight. With regard to the effects of ablation gases, the interactions with turbulent flow are perhaps even less understood than that of roughness. The main effect of injecting gas into the boundary layer is to reduce heat flux through the boundary layer by addition of a relatively "cooler" gas at the surface. Also known as film cooling, flow injection is a phenomena often encountered in situations where heat flux to the wall is undesirable. However, flow injection has its own effects on the mean flow, one of which is the addition of instability in the flow as momentum is moved farther away from the wall and an increased likelihood of flow separation from the wall.

The combination of roughness and blowing is therefore very complex due to the complications listed above and further described in Chapter 2. To aid in understanding the fluid-mechanical effects present, the current set of experiments used a subsonic research facility and well-understood instrumentation techniques to provide insight into this flow type. It is the goal of this research to provide feedback to the TPS designer and aid in our understanding of the complicated interactions of these phenomena while building upon the current knowledge base and indicating where future research will be most beneficial.

Chapter 2

Background

2.1 Basic Turbulence Theory

There are a number of early works which are often credited with the development of turbulence theory. Perhaps the most recognized are the experiments by Osborne Reynolds [55]. His experiments involved a carefully constructed glass pipe with the ability inject dye into the flow. Reynolds had control over the pipe diameter, flow velocities, and fluid viscosities and made the very important observation of transition from laminar to turbulent flow. He discovered that this happened for roughly the same value of a dimensionless parameter, known today as the Reynolds number

$$Re = \frac{UL}{\nu} \tag{2.1}$$

where U is the velocity, L is a characteristic length, and ν the kinematic viscosity. As Osbourne also deduced, the Reynolds Number is a measure of the ratio of inertial forces to viscous forces and provides a way to gage the relative importance of these two forces in any type of flow. Reynolds went on to develop these ideas in a later paper [56] in which he decomposed the flow into the mean and fluctuating parts (the Reynolds equations) and introduced the idea of turbulent kinetic energy, which represented a transfer of energy from the mean flow to turbulence. The Reynolds equations represent a tool for understanding the energy content of turbulence, and to this day experimental fluid measurements still characterize flows based on the behavior of the Reynolds stresses. Reynolds decomposition is built around breaking

the time varying velocity into time-averaged and fluctuating components such that

$$u(t) = \overline{U} + u^{'} \tag{2.2}$$

where $u(t)$ is the time-varying velocity, $\overline{U}$ represents the time-averaged velocity, and $u^{'}$ the fluctuating velocity about the mean. Reynolds decomposition of the flow into these two quantities was a breakthrough in the analytical approach to turbulence.

Later, an important work was published by Ludwig Prandtl [53]. For the first time, this paper described the boundary layer, the development of drag, flow separation and the concept of aircraft stall. Prandtl's boundary layer theory had the important contribution of separating the flow into two regions, the inner- or viscous region and the outer- or inviscid region. Later, Prandtl wrote what is considered to be a canonical work in turbulence [51]. In it he analyzed the limit of very high Reynolds number, and found that the inner layer (where $y/L << 1$) depends only on the kinematic viscosity, ν, and the wall shear stress, τ_w. From this a velocity scale can be constructed

$$U_\tau = \sqrt{\tau_w/\rho} \tag{2.3}$$

where ρ is the fluid density and the resulting velocity is known as the friction velocity. This scale is very important in turbulent flows as it allows for an inner length scale to be developed known as the viscous length

$$\delta^+ = \frac{\nu}{U_\tau} \tag{2.4}$$

and the Reynolds number based on these is

$$\frac{\delta^+ U_\tau}{\nu} = 1. \tag{2.5}$$

The distance from the wall can also be normalized by these viscous scales

$$y^+ = \frac{y}{\delta^+} = \frac{U_\tau y}{\nu}. \tag{2.6}$$

From this point forward, the usual notation for viscous scaling can be adopted, which utilizes the + superscript to identify terms non-dimensionalized using U_τ and δ^+. Furthermore, to indicate the ratio of the outer and inner length scales, a friction Reynolds number can be defined with the friction velocity, and the outer length scale (boundary layer thickness, δ for boundary layers; radius, R for pipes; and half-height, h for channels) to produce the friction Reynolds number

$$Re_\tau = \left(\frac{y}{\delta^+}\right) / \left(\frac{y}{L}\right) = \frac{LU_\tau}{\nu}. \tag{2.7}$$

Prandtl argued that the inner layer (at very high Reynolds numbers) depends only on these viscous scales, and the functional form of the velocity gradient depends only on the ratio of the friction velocity and the wall distance, times some function of wall distance normalized by δ^+ [51] . Theodore von Kármán expanded these ideas to develop the logarithmic law of the wall in his 1930 paper [28, 50] which is applicable at the outer part of the inner layer where viscosity has a small effect, and the dependence on the viscous length vanishes from the law of the wall,

$$\frac{dU^+}{dy^+} = \frac{1}{\kappa y^+} \tag{2.8}$$

where κ is the von Kármán constant, and can be integrated to produce the logarithmic law of the wall

$$U^+ = \frac{1}{\kappa} \ln y^+ + B \tag{2.9}$$

where B is an integration constant.

The inner and outer layers can be broken down based on the approximate wall

distance as in table 2.1.

Table 2.1: Separation of wall regions in channel flows [50]

Inner Layer	$y^+ < 5$	Viscous sublayer
$y/h < 0.1$	$y^+ < 50$	Viscous wall region
	$5 < y^+ < 30$	Buffer layer
Outer Layer	$y^+ > 30$, $y/h < 0.3$	Log-law region
$y^+ > 50$	$y^+ > 50$, $y/h < 0.1$	Overlap region

2.2 Turbulence and Roughness

Turbulent flow interactions with roughness have been studied extensively for over a century [26]. The role of roughness has been very important in the development of turbulent theory, specifically with regard to engineering-type flows (such as duct, pipe, and channel flow) where roughness is often encountered. Perhaps one of the most well known, and earliest works on this subject was that by Johann Nikuradse [45]. In this set of roughness experiments, carefully sifted sand was used to coat the inside of pipes to produce a very uniform roughness pattern. This allowed Nikuradse to develop an idea of the effects of roughness on the mean flow quantities and the wall shear stress. To this day, many turbulent flow types are characterized by their "equivalent sand grain roughness", k_s, in reference to Nikuradse's original classification of flow modifications based on the wall shear stress and the sand grain size. This section will review the relevant facets of turbulent flow interactions with roughness. The number of studies in this field is very large, and a full review is not attempted in this thesis. Instead, a brief review of the notation used for roughness, the effects on the time-averaged statistics, and a review of the most relevant literature is discussed in the following.

2.2.1 Roughness Geometry

One of the major difficulties in rough wall studies, and one of the main sources of confusion when comparing data, is accurately defining the roughness geometry. The geometrical feature with the largest effect on the flow is arguably the roughness height, k. This parameter is the one most often reported in the literature. However, there are numerous other important lengths, denoted L_i, which affect the flow behavior. Often a density is defined based on the frontal area of a roughness element(s) per ground area the element(s). For three-dimensional roughness this term can be written as

$$\lambda_{3D} = \frac{nkL_z}{A} \tag{2.10}$$

where n is the number of roughness elements in the horizontal area, A and L_z is the spanwise spacing of the roughness elements. For two-dimensional roughness the equation becomes

$$\lambda_{2D} = \frac{k}{\lambda} \tag{2.11}$$

where λ is the element spacing or "wavelength" in the streamwise direction. These dimensionless aspect ratios have been used to quantify the fully-rough flow behavior near the roughness elements themselves and the resulting mean-flow quantities discussed in section 2.2.2. These simple aspect ratios are only one way of classify roughness elements, as numerous L_i can be chosen to make other values whose effects on the mean flow have to be investigated separately. This has led to numerous studies to determine the "most relevant" roughness scales. Various correlations have been developed for three-dimensional (for example [15, 54, 61]) and two dimensional roughness patterns (see [47, 54]). While these correlations can guide the design of an experiment, very minute differences in roughness elements and experimental facilities can drastically affect the resulting flow field. This has led to the expansive body

of research on roughness, as new experiments must be performed on new roughness geometries and flow conditions.

One length scale which has been deemed essential to classifying a rough-walled flow is the viscous scaled roughness height, or roughness Reynolds number

$$k^+ = \frac{kU_\tau}{\nu} \tag{2.12}$$

which is the ratio of the roughness height to viscous effects, and as demonstrated in the following section, is the driving parameter for characterizing mean flow behavior when roughness is present. This parameter is the most often cited in the literature, as it has first order effects on the flow behavior which dominate the other roughness length scales. This will be further discussed in section 2.2.2.

2.2.2 Roughness effects on the mean flow

In flows with rough-wall boundaries, the mean flow behavior is displaced away from the wall by an amount $0 < y_0 < k$, known as the zero-plane displacement, where $y_0 = 0$ for a smooth surface. There have been multiple attempts to define y_0 (see [54] for a listing), but an exact definition is elusive and thus different methods are typically employed dependent on the type of roughness. A best practice is to always include y_0 in the experimental results so its effect on the mean profiles can be judged. The error in determining y_0 is often negligible when experiments are concerned with the outer flow (or even the log layer when viewing high Reynolds number data) as any small shift in the profile has minimal effect on the outer layer. For the purposes of this thesis, the shift is incorporated into the profile via

$$Y = y + y_0. \tag{2.13}$$

The mean flow effects of roughness can be derived based on an asymptotic match-

ing analysis as done in the roughness review paper by Michael Raupach [54]. This leads to two velocity dependencies, the first of which is the defect law which is valid in the outer layer, and depends only on an outer length-scale L

$$\frac{U(Y) - U_\infty}{U_\tau} = F(Y/L) \tag{2.14}$$

and the second is for the inner layer which only depends on the viscous scaled terms

$$(U(Y))^+ = G(Y^+, k^+, L_i^+) \tag{2.15}$$

In the overlap region both of these laws must hold, and the gradients of each function are matched

$$\frac{Y}{U_\tau}\frac{dU}{dY} = Y^+\frac{dG}{dY^+} = \eta\frac{dF}{d\eta} = \kappa^{-1}. \tag{2.16}$$

Integration of this function gives the law of the wall for turbulent, rough-walled flow

$$U^+ = \frac{1}{\kappa} lnY^+ + C(k^+, L_i^+) \tag{2.17}$$

where the integration term, C, is dependent on the roughness length scales. The main effect of roughness is to alter the log-law constant, which is more readily seen in the commonly used form of the log-law for roughness

$$U^+ = \frac{1}{\kappa} lnY^+ + B - \Delta U^+(k^+, L_i^+) + W(Y/L) \tag{2.18}$$

where the term ΔU^+ is the roughness function, and has zero value for smooth walls. The outer layer deviation from the log-law is given by the wake function, $W(Y/L)$. The effect of the roughness function is described as the shift between the smooth and rough wall velocity profiles on a semi-logarithmic, inner-scaled mean profile plot [54].

This assumes that the functional dependence of equations 2.14 and 2.15 hold. Namely that an overlap layer exists between the inner and outer layers which depends solely on the wall distance, Y.

To ensure that the dependencies of equations 2.14 and 2.15 hold, the outer length scale must be much larger than the viscous scales and the roughness heights. This is the core assumption behind the often cited wall-similarity hypothesis for roughness. Namely, that the outer layer is unaffected by the presence of roughness at high Reynolds numbers except for determining U_τ, Y, and the boundary layer thickness δ. As noted by Raupach [54], the wall similarity hypothesis is an extension of Reynolds number similarity for smooth walled flows. Wall similarity is often referred to as Townsend's hypothesis as it uses many of the arguments of Albert Townsend [46, 65]. Essentially, Townsend's hypothesis postulates that at high Re, and outside the viscous sublayer, the time-averaged statistics of a turbulent flow are unaffected by viscous scaling, δ^+. The scales k and L_i are also irrelevant in the outer layer. As summarized by Raupach [54]:

"Therefore, wall similarity holds for *relative mean* motion at all heights above the roughness sublayer. Since the turbulence maintains and is maintained by the mean velocity profile, it is unlikely that surface length scales which are irrelevant for the mean velocity profile are important for the dominant turbulent motions."

It is generally accepted that similarity holds in rough-walled flow except for the viscous or roughness sublayer (near the roughness elements themselves). Following the derivation in [54], analysis of the effects of roughness at high Reynolds number, and away from the wall, given the viscosity independence of the flow and equation 2.14, the law of the wall in terms of an equivalent sand grain roughness, k_s can be found

$$k_s = \frac{32.6\nu}{U_\tau} e^{-\kappa\left(B-\Delta U^+\right)}. \tag{2.19}$$

This length allows for a quick comparison of the roughness function and wall shear

of some new roughness elements to that of the sand-grain roughness of Nikuradse [45], essentially establishing a baseline case of comparison. This new length-scale also gives way to definition of the sand-grain roughness Reynolds number

$$k_s^+ = \frac{k_s U_\tau}{\nu} = 32.6 e^{-\kappa\left(B - \Delta U^+\right)}, \tag{2.20}$$

which is separate from the Reynolds number based on the actual roughness height, k^+, in that it cannot be determined without knowing ΔU^+ (except for the obvious case of sand-grain roughness where $k^+ = k_s^+$). A rough-walled flow can then be classified based upon the value of k_s^+ into one of three flow regimes:

1. $k_s^+ < 5$ The surface is considered to be aerodynamically smooth, as roughness of this height causes no appreciable shift in ΔU^+.

2. $5 < k_s^+ < 70$ The flow exhibits transitional behavior, meaning the form drag on the roughness elements is significant, but viscous drag is still important.

3. $k_s^+ > 70$ The flow is fully rough, and drag is produced primarily through form drag on the roughness elements. The flow obeys Reynolds number similarity.

As noted previously, these classifications were originally developed using sand-grain roughness, and the actual location of the transition zone ($5 < k_s^+ < 70$) depends on λ_{2D} or λ_{3D}. The main issue with using k_s to classify roughness effects is that sand-grain roughness itself is poorly geometrically defined, and thus it is difficult to physically scale k_s. This leads to additional confusion when comparing sand-grain studies to geometrically well-defined studies such as hemisphere or cone arrays. The effect of the ground-breaking and detailed work of Nikuradse can not be denied, however all subsequent roughness studies have been stuck with the precedent of using a poorly defined roughness geometry for comparison.

Another important aspect of rough-walled flow is the mutual sheltering of roughness elements which occurs in fully rough flow. Typically, mutual sheltering occurs when a stable permanent vortex forms in-between the roughness elements and effectively isolates the roughness from the mean flow. This condition is preceded by an unstable vortex shedding regime where mean flow separates from the wall somewhere near a roughness element, and re-attaches before the next roughness element. These two regimes can be classified based on the ratio of k_s/k, which increases linearly with λ_{2D} and λ_{3D} until some critical value, and then decreases linearly with λ_{2D} and λ_{3D}. This critical value indicates the onset of mutual sheltering of the roughness elements. This means that the flow behavior can potentially be predicted with some accuracy given λ_{2D} or λ_{3D} and often this is done to set the value of k_s *a priori* [15]. Obviously, this method is more accurate with a well defined geometry such as 2-D square bars or sinusoidal, "wavy", roughness as less length-scales are present compared to 3-D roughness and several correlations exist [54]. Generally for $\lambda_{2D} > 0.2$ mutual sheltering effects are seen over the roughness elements [61]. The results for 3-D roughness are more scattered as aspect ratios other than λ_{3D} have an effect on k_s, whereas for 2-D roughness it appears λ_{2D} does a decent job at predicting the equivalent sand-grain roughness.

2.2.3 Turbulence Statistics

The wall-similarity hypothesis also applies to the dominant turbulent motions, which are independent of the roughness geometry as well at high Re [54]. This independence implies that the basic structure of turbulence is preserved regardless of roughness geometry. This is perhaps particularly interesting because it indicates that single-point turbulence statistics should collapse regardless of roughness geometry and Reynolds number (provided Re is large enough). There is lingering debate on whether this is true, as some researchers argue that the turbulent motions are independent of the

roughness [2, 34, 54, 59] while a few have proposed that roughness effects extend into the outer layer [32, 36]. The differences seen in these studies have been somewhat reconciled by the review paper of Javier Jiménez [26] who argues that a value of $L/k > 40$ would be required for wall-similarity to hold. Furthermore, little is known concerning the makeup or organization of the dominant motions present in a turbulent flow, and even less still about the motions in the roughness sublayer, despite the vast amount of experimental, analytical, and numerical analysis applied to this problem. Knowledge of these motions would allow for determination of any modifications in the presence of roughness, and the resulting impact on wall similarity. Therefore work on characterizing turbulent structure modifications due to roughness and comparisons to the smooth-wall cases must be carried out. Furthermore, with regard to the time-averaged turbulence statistics, wall-similarity dictates that collapse will be seen across the Reynolds stresses, and higher order moments (provided the Reynolds number is high enough for the flow to be fully rough) with the smooth-wall case, except very near the wall.

2.3 Turbulence and Flow Injection

As with surface roughness, the effects of momentum injection or "blowing" through a surface have received significant attention due to their relevance in applications such as turbine blade transpiration cooling, flow separation control, and turbulence mode modulation. Studies incorporating blowing boundary conditions typically focus on either blowing introduced locally through a slot or series of holes [9, 19, 33] or uniformly across the surface [11, 14, 63] through a porous medium or smooth plate with an array of holes. Generally, blowing has been found to decrease skin friction through reduction of the mean shear at the surface. Studies of blowing effects primarily focus on boundary layers, although channel flow studies have also been conducted using direct numerical simulation at low Reynolds numbers [11, 29, 44, 58, 63, 66]

with blowing found to enhance turbulent motions within the channel and increase Reynolds shear stress.

Depending entirely upon the method of injection, the modifications to the mean flow behavior vary widely. Generally, for zero-pressure gradient boundary layers, the effects of blowing on the mean velocity defect plot ($(U_{\text{inf}} - U)^+$ vs y/L) have been found to be independent of blowing rate [6]. Some approximation can be made for wall similarity with respect to the mean flow, as noted in [31], where a modified form of the law of the wall is given for boundary layers with a small amount of upstream flow injection

$$U^+ = \frac{1}{\kappa} ln(y^+) + B + KU^+_{inj} \tag{2.21}$$

where U^+_{inj} is the injection velocity scaled in viscous units and K is weakly dependent on U^+_{inj}. Kornilov recommends a value of $K = 9.6$ for turbulent boundary layers with injection. The form of equation 2.21 is very similar to the log-law of the wall for rough walled flows, equation 2.18. With the KU^+_{inj} term acting similarly to the roughness function, ΔU^+ in that it causes a shift in the inner-scaled mean velocity profile. However, instead of the roughness case where momentum is removed from the mean flow, blowing serves to add momentum and generally causes a positive shift in the profile.

Although flow injection has a similar (but opposite in sign) effect on the mean flow as compared to roughness for localized injection, there remain other effects which are specific to blowing which limit the analogy with roughness effects. The method of flow injection can significantly affect the resulting flow structure and thus caution is warranted before applying Townsend's hypothesis. When injection is localized through a slot or porous strip, the turbulence structures appear to re-adapt to a state which is approximately similar to the state prior to injection [19, 33]. In the region of flow injection, significant modification to the Reynolds stresses are typically seen, which is unsurprising because the boundary conditions are supplying extra

momentum to the flow. For flows where the injection is uniform across the surface, a slightly different picture has been observed. Upon initially encountering injection, the flow will take several development lengths to adjust to the new boundary conditions. This is followed by a region of relatively stable flow behavior in which the flow appears to reach a fully developed state [11]. However, this is a very different condition to that of Reynolds number similarity in that the turbulence statistics vary quite significantly from the smooth-wall boundary condition.

Another difficulty arises when considering uniform flow injection for external and internal flows. As seen in smooth wall studies [42], the coherent motions of internal flows such as pipes and channels may be significantly different than boundary layer-type flows. This would indicate that the disparate structures in external and internal flows react differently to uniform flow injection, and again suggests that application of Townsend's hypothesis may not be valid. Only recently has work begun on characterizing the structural differences of flows with injection [58]. Understanding the coherent motion similarities and differences between internal and external flows will undoubtedly aid in understanding the limitations of Townsend's hypothesis for flow injection cases.

2.4 Turbulent Interactions With Roughness and Flow Injection

In comparison to the quantity of research focused on the separate effects of roughness or blowing on turbulent wall-bounded flow, there have been relatively few examining their combined effects [20, 21, 57, 67]. These studies limited their investigation to mean flow properties, with only the work by Schetz and Nerney (1977) providing any turbulence statistics [57]. Generally, it has been observed that applying roughness and blowing theory independently to predict their combined effects on the flow results

in poor matching of the empirical data. Due to the diversity of these investigations, conducted over a range of subsonic to supersonic flows and for various geometries (including axi-symmetric bodies, slender cones, and flat plates), there is little consensus as to what these combined effects are. For example, an additional ΔU^+ shift due to blowing was observed in the mean flow by Voisinet (1974) [67], however Schetz and Nerney observed no such shift. Furthermore, prior studies were largely limited to mean flow properties, with little-to-no information available about how these combined effects act to modify the turbulence, with the exception of Schetz and Nerney who observed that blowing will increase the turbulence intensity near the wall. This is consistent with the observations described in Section 2.3 when blowing is present over a smooth surface. An additional point of confusion is the effect of roughness geometry. The work by Healzer et al. (1974) used copper balls of $k = 1.27$ mm (which is the ball diameter) sintered into a packed array [20]. Schetz and Nerney used a sintered metal surface as well but with much smaller roughness height of $k = 0.07$ mm. Voisinet employed an entirely different approach by using a wire mesh, which is geometrically very different from a sintered surface and perhaps just as difficult to characterize accurately. Roughness heights of $k = 0.1, 0.33, 1.25$ mm are given for the three meshes used. Finally, Holden (1988) does not give a precise value for k in his report, but does mention using spherical roughness elements [21].[1] Regardless of the roughness geometry used, the trend among these studies is that roughness acts as a momentum sink in the flow and blowing acts as a momentum source. Using the notation of the previous sections, the effects of roughness and blowing can be balanced in the mean flow by altering ΔU^+ and KU^+_{inj}.

The lack of data may be unsurprising, as the effects of roughness and blowing are poorly understood individually, making their combined effect very complex. How-

[1] Holden's report may not have included the roughness geometry used in his study due to restraints on releasing classified information as the work was funded through the Air Force Office of Scientific Research [21]. Despite this, it does make Holden's point in his literature review section regarding the faults of using ill-defined surface geometry rather strange.

ever, it is valid to argue that many systems of engineering and scientific interest contain these effects. One of the more prominent being thermal ablative heat shields, which contain surface roughness due to charing of the heat shield and mechanical erosion from particle spallation with blowing arising from resin which pyrolyzes and is then out-gassed through the ablator structure. In addition to the applicability to char-roughened ablative heat shields, a basic understanding of the flow structure modifications due to roughness and blowing could be useful for reducing losses in transpiration cooled equipment such as turbine blades. Furthermore, empirical blowing and roughness data can be used to validate CFD code which implements these as boundary conditions.

Thus, with the numerous applications of these studies, and the relatively few sets of empirical data, it appears as though experimental results in this area are necessary as the bulk of the work completed on surface roughness and blowing interactions is not cohesive and covers a broad range of flow conditions. This is less of an issue in the roughness and blowing cases individually as much work has been completed on these topics. There have also been no concise experiments performed (either in a compressible or incompressible environment) which investigate the modifications to the higher-order turbulence statistics and the associated turbulent motions due to roughness and blowing. This would allow for further insight into the applicability of Townsend's hypothesis. With these deficiencies in mind, the current work aims to fill some of the gaps left by previous work and hopefully provide insight into this unique flow environment.

Chapter 3

Experiment Design

The experiments were conducted in the Turbulent Channel Flow Facility (TCFF) in the University of Kentucky Experimental Fluid Dynamics Lab (EFDL). This is the same facility used in the studies by Estejab (2011) [16], but with modifications to allow for roughness and flow injection in the test section. The channel has a half height of $h = 50.8$ mm and an aspect ratio of 9:1 to ensure quasi-2D flow at the centerline [68]. The TCFF is powered by a 5.2 kW centrifugal blower which drives the flow through conditioning, development, and test sections at area averaged, or bulk, velocities up to $\langle U \rangle = 30$ m/s; producing Reynolds numbers up to $Re_b = h\langle U \rangle/\nu = 102,000$ or $Re_\tau = hU_\tau/\nu = 4200$ for the smooth-walled cases. Data from Estejab [16] is used here as the smooth-wall comparison cases for similar Reynolds numbers. A schematic of the smooth-wall channel facility used can be seen in figure 3.1

To ensure a fixed turbulent transition location a boundary layer trip consisting of a 50 mm wide section of 120 grit sand paper followed by a 100 mm wide section of 60 grit sandpaper was located at the development section inlet. The distance from the channel inlet to the test section is $246h$, allowing the turbulence to reach a fully developed state [40]. The test section is $24h$ long, with an instrumentation access point located at its mid-point. Following the test section, an additional $12h$ long conditioning section ensures a consistent pressure gradient inside the test section.

For this set of experiments, the top surface of the downstream end of the TCFF test section was replaced with a $24h$ long section of nominally 2-D, sinusoidal roughness. To force flow through the rough surface, an apparatus was designed and constructed to produce backplane pressure on the surface. Further details on the blowing rig and rough surface are provided in Section 3.1. In order to properly characterize the flow injection a blowing ratio was defined

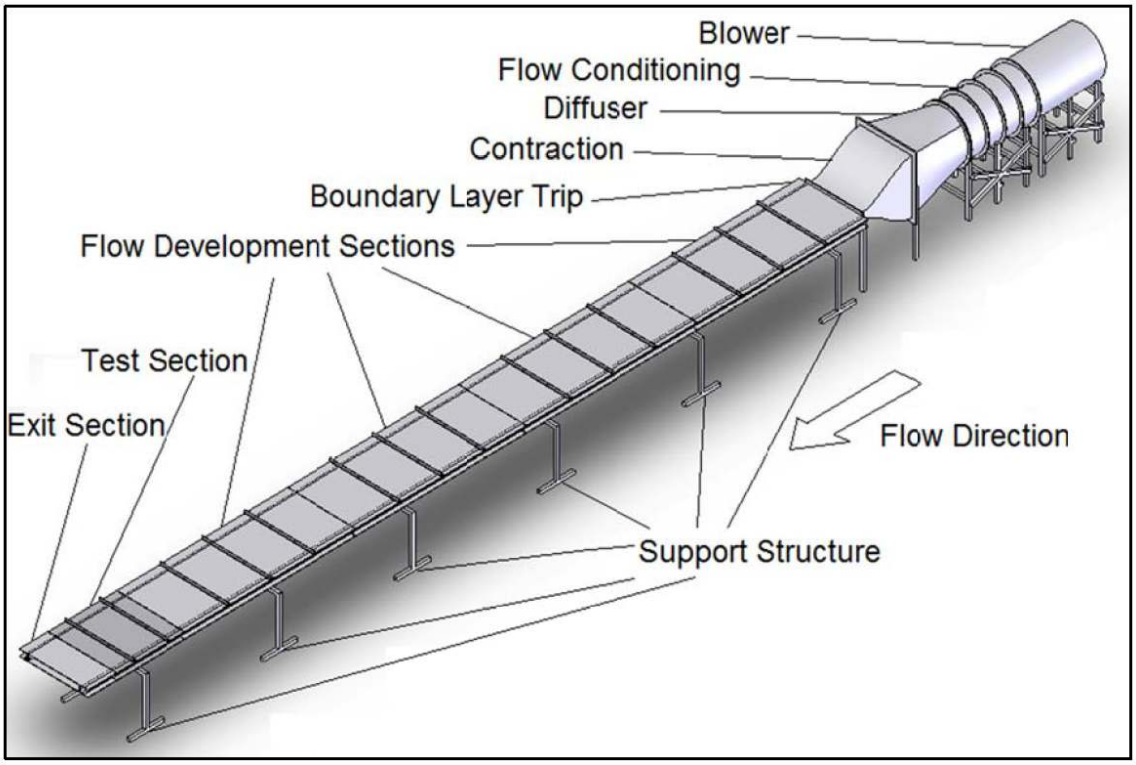

Figure 3.1: Schematic of smooth-wall channel facility before modification for use in current studies.

$$BR = \frac{U_{inj}}{U_m} \tag{3.1}$$

Where U_{inj} is the velocity of the injected air, and U_m is the maximum measured velocity in the channel, at wall normal location y_m. Because the centerline velocity, U_{cl} varied with blowing rate when tunnel speed was kept constant, the maximum velocity proved to be a better method of reducing the blowing ratio and accounted for any asymmetry in the flow due to blowing. Generally, this asymmetry was small, with the value of U_m differing by less than 2% from U_{cl} in both location and magnitude. This is also the typical way of characterizing blowing ratios in DNS channel flow studies with transpiration [11].

3.1 Flow Injection Rig

In order to accurately capture the effect of flow injection, the key parameter to measure is the flow injection velocity across the surface. If using gas from a pressurized cylinder, the method can be straightforward as compressed gas flow meters are commercially available and relatively inexpensive. Originally, this method was considered, however a reliable source of dry, room-temperature, compressed air was not readily available so the decision was made to use a series of small fans to pressurize the flow chamber. With this decision made, the other aspects of the blowing rig were designed with several key parameters in mind, listed here in order of priority:

1. Distribute the backplane pressure on the rough surface evenly so as to ensure a consistent average blowing rate across the entire roughness.

2. Provide a means of accurately determining the injection velocity.

3. Support the rough surface in the channel while keeping the surface as planar with respect to the channel floor as possible.

4. The rough surface mounting method must be such that new roughnesses can be switched into the blowing rig with relative ease if desired.

The blowing rig itself went through two design iterations. One of the main reasons for this is a desire to attain higher blowing ratios than the original blowing rig would allow. The other reason is related to measurement of the injection velocity. This quantity was measured originally with a loss coefficient, and then later by a more reliable Venturi-type flow meter. Both designs of the blowing rig will be discussed in the following and the benefits to each as well as the methodology used to actually calculate the blowing ratio will be demonstrated. The original blowing rig design will be referred to as V.1 and the new blowing rig will be referred to as V.2.

3.1.1 Blowing Rig V.1

For the first iteration of the blowing rig, ten 14 Watt Sofasco SF12038 high-flow AC fans were wired with a controller to vary the fan speed and control the blowing rate. To reduce any non-uniformity caused by the fans, a series of screens were installed inside the blowing rig. The interior geometry of the blowing rig box was 0.4572 m tall by 0.889 m wide, by 1.143 m long. The box was composed of three main sections, the topmost of which contained the blowing fans and was 152.4 mm in height. The second section was 203.2 mm in height, and the third section was 101.6 mm in height. Between each section was a conditioning screen designed to break down instabilities due to the fans in a controlled manner, and spacing between screens was at least sixty times the mesh size [35]. The first, coarse grid was located after the topmost section and consisted of a woven polypropylene mesh (McMaster-Carr part number 9275T38) with mesh size of $M = 3.4$ mm. Following this the flow was allowed to develop over a distance of 153.2 mm before entering an aluminum honeycomb flow straightener (Bellcomb Industries part number BSP245C) of thickness 25.4 mm, average hexagonal cell size of width 50.8 mm. Directly after the flow straightener, the flow entered a second flow conditioning screen of mesh size $M = 1.25$ mm (McMaster-Carr part number 87655K132). Finally, the flow developed an additional 101.6 mm before encountering the rough surface.

The box itself was constructed of 1 mm thick 3003 Aluminum sheet metal for light weight and ease of machining. All sections of the box were formed using a sheet-metal bender, with each vertical section composed of C-shaped channels pop-riveted together at the ends. The spanwise side sections supported the box across the channel. The streamwise side sections of the box were attached to the spanwise sections with an L-shaped, pop-riveted bracket. For smooth-wall turbulence studies, the TCFF test section has a plexiglass top which bolts to the test section side-walls. The same bolt-hole configuration was employed on the box to mount the bottom of

the box to the test section. The rough surface was mounted to the 3.81 cm lip around the edge of the box. This lip was necessary for mounting of the rough surface and for situating the rig above the test section, but it reduced the interior dimensions of the flow injection area (0.889 $\times$ 1.143 m versus the test section dimensions of 0.9144 $\times$ 1.2192 m). Thus the rough surface had an unblown section in the streamwise direction of 12.7 mm on each side, and 38.1 mm on the entrance and exit to the test section. Due to the small relative size of these unblown sections compared with the total flow injection area, the effect of these unblown sections is considered negligible.

This first version of the blowing rig used a loss coefficient method to determine the flow rate through the screen. The blowing rig was constructed with a set of pressure taps around the perimeter of the bottom two sections. Using the lowest set of pressure taps and the static pressure ports in the channel, the pressure drop across the rough surface could be determined using the loss coefficient [64].

$$K_{roughness} = \frac{\Delta p}{1/2 \rho U^2} \tag{3.2}$$

where $K_{roughness}$ is the pressure loss coefficient, Δp the pressure drop across the screen (measured at static ports PR2 and PC1 in figure 3.3), and U the mean velocity. The pressure loss coefficient for the rough surface was determined by an external set of experiments performed in a pipe flow facility also located in the EFDL. This pipe was constructed specifically to determine the loss coefficient of various screens and provided a novel way of determining the very low flow rates experienced when using the rough surface in the TCFF. The pipe was constructed of smooth PVC, with a diameter, D = 50.8 mm. The pipe was pressurized at one end and the flow rate regulated with a ball valve. The flow entered the pipe and was allowed to develop along a length of $295D$ after which the test section is located. The insertion of a porous test specimen was performed with specially designed plugs which positioned

the test specimen in the pipe but did not allow for pressurized gas to escape the pipe. This test section was followed by a further $100D$ of pipe to allow for pressure measurements after the test article. The pipe was fitted with pressure taps according to the recommendations of Tavoularis (2005) [64] which allowed determination of the pressure drop across the test article. The velocity profile at the pipe outlet was also measured using a Pitot-static tube mounted on a traverse. For various inlet pressures, the pressure drop across the sample and mean exit velocity were recorded and used to generate the loss coefficient, $K_{roughness}$.

Figure 3.2: Upstream view of TCFF with blowing rig V.1 installed above test section

Several of the issues regarding the use of a pressure loss coefficient are evident in figure 3.4. The first of which is that to measure a significant amount of velocity at the end of the pressure drop pipe, a high pressure had to be applied to the test article. This meant that the run cases later performed in the TCFF were outside the calibration points and thus subject to a significant amount of uncertainty. Also, the large pressure drop required indicates that the flow after the test piece was subject to a large amount of non-uniformity, and that the rough surface was highly non-porous. Equation 3.2 was originally developed for screens and other highly porous samples [64].

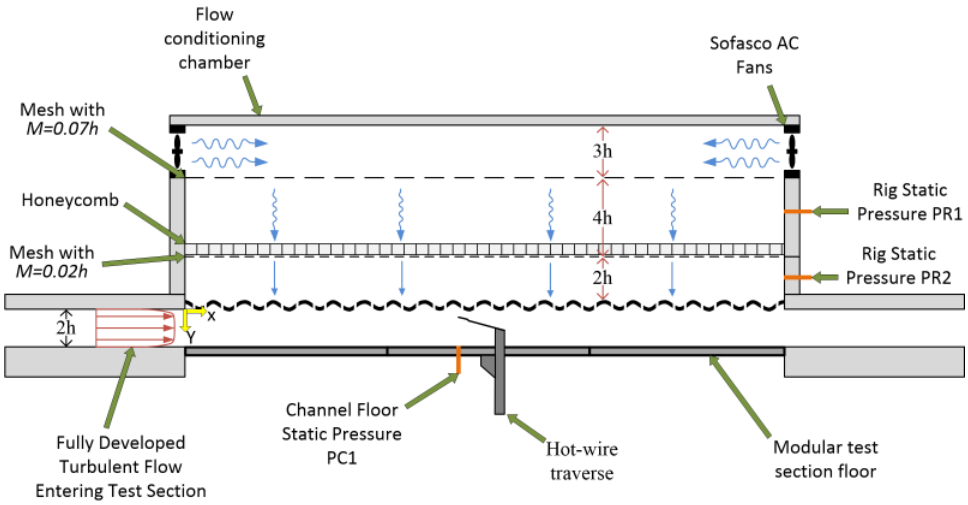

Figure 3.3: Schematic of blowing rig V.1

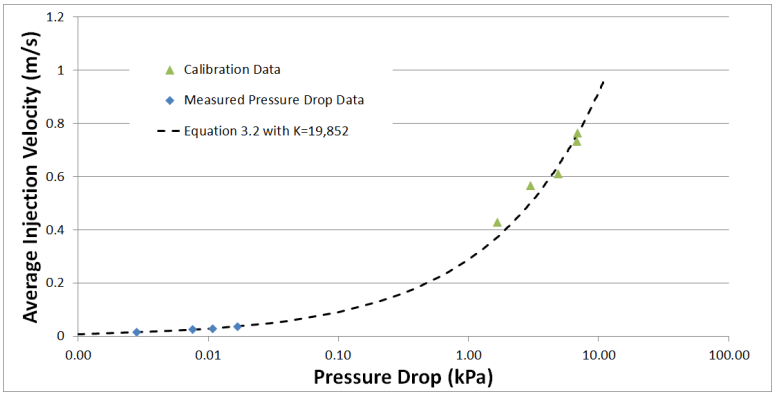

Figure 3.4: Plot of calibration points for determining $K_{surface} = 19,852$ for the rough surface, and the resulting equation 3.2, $U_{inj} = \sqrt{(2\Delta P)/(19,852\rho)}$. The actual pressure drops measured during test runs in the TCFF are also plotted for a test case at $Re_h \approx 35,000$.

To confirm the flow rates calculated using equation 3.2, the Sofasco fans factory flow rate curve was compared to the results acquired for flow rates inside the channel using $K_{roughness}$. The highest measured static pressure difference between the blowing rig and the channel was 16.7 Pascals (0.067 inches of water column) and equated to a calculated blowing rate of 2.28 m^3/min (80.7 CFM). This is in line with the factory specifications of the Sofasco fans which are reported to have a maximum flow rate of 0.24 m^3/min (8.5 CFM) per fan at low static pressures, which results in a flow rate of 2.4 m^3/min and is very close to the calculated value. Despite this encouraging

result supporting our technique of measuring U_{inj}, the two issues regarding the use of a loss coefficient were the main motivators for implementing a higher confidence method of measuring the injection velocity.

3.1.2 Blowing Rig V.2

From the beginning, the second version of the blowing rig was designed to more easily measure U_{inj}. It was decided that a venturi-type flow meter would provide the best accuracy, ease of use, and lowest pressure drop compared with other conventional flow measurement devices such as variable-area vanometers, or orifice plates. Because no high pressure air source was available, and because the blowing fans on V.1 of the blowing rig were only able to produce the small pressure drop seen in figure 3.4, a new source of injection air was required. A centrifugal blower (McMaster-Carr part number 1963K15) was chosen because it could supply a relatively large flow rate of 5.7 $m^3/minute$ (200 CFM) at a large static pressure of 350 Pascals (1.4 inches of water column). This was nearly double the flow rate of the Sofasco fans which was measured to be 2.28 m^3/s (80.7 CFM) at 16.7 Pascals (0.067 inches of water column). The new blower was over-sized to allow for a wide range of BR to be investigated. It was estimated using $K_{surface}$ that a blowing rate of $BR = 0.016$ or 1.6 % of the maximum channel velocity could be achieved for $Re_h \approx 35,000$, as opposed to the previous maximum value of 0.35 % using the Sofasco fans.

Because the injected flow now came from a single source, and had to be measured at a single location prior to entering the blowing rig, several modifications to the blowing rig were necessary. The centrifugal blower was fitted external to the tunnel with a reducing section which took the square exit of the blower down to a three-inch diameter tube. This tube was fitted to a flexible section of the same diameter, approximately 1 meter in length, to eliminate any blower vibrations from reaching the blowing rig. The tube was connected to a section of Schedule 40 black steel threaded

pipe, size 3 NPT with a nominal inner diameter of 76.2 mm (3 inches). Then the flow traveled through 5 pipe diameters of straight section before entering the venturi meter which was threaded to accept the pipe. Following the meter, an elbow was included which re-directed the air into a fixed pattern diffuser (McMaster-Carr part number 1837K21) mounted on top of the blowing rig. The diffuser evenly distributed the flow into the blowing rig. These modifications can be seen in figure 3.5 and in the schematic diagram of figure 3.6. The rest of the blowing rig, including the flow conditioning screens, were left intact in V.2, with the only modification being to block off the Sofasco fans and pressure ports.

Figure 3.5: Overview of blowing rig V.2

Following the construction of blowing rig V.2, a series of smoke-flow visualization studies were performed to asses the uniformity of the injected gas velocity over the rough surface. It was found that at multiple tunnel speeds, the blowing rig performed well at distributing the flow into the channel. The resulting images from these tests are available in appendix 5.1.

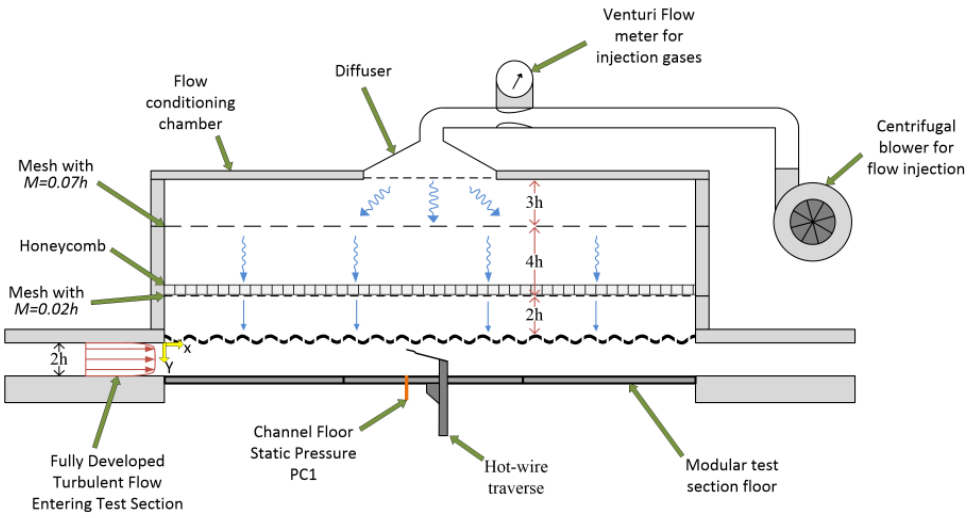

Figure 3.6: Schematic of blowing rig V.2

3.2 Rough Surface and Modular Test Section Floor

The rough surface used for this set of studies is an acoustic panel with a nominally two-dimensional, sinusoidal roughness pattern. The roughness elements are spaced with a streamwise length of $L_x = 7$ mm and amplitude of $k = 1$ mm. The surface had micro-cracked pores distributed uniformly across its surface, which allowed for evenly distributed blowing. This surface is an acoustic panel known as "Millennium Metal" manufactured by American Acoustical Products[1] and acquired for use here because of its very uniform surface roughness. An image of this surface is included in figure 3.7.

In addition to the modifications mentioned previously for blowing rig V.2, the test section floor was also adapted to include a modular floor design. This floor allowed easy and accurate positioning of the measurement station at multiple streamwise locations. An image of this is included in figure 3.8.

The dimensions of the new floor allowed measurements to be taken at numerous streamwise positions, but for this study three positions were chosen and are given in

[1]Additional information is available at www.aapusa.com/millennium_metal.html

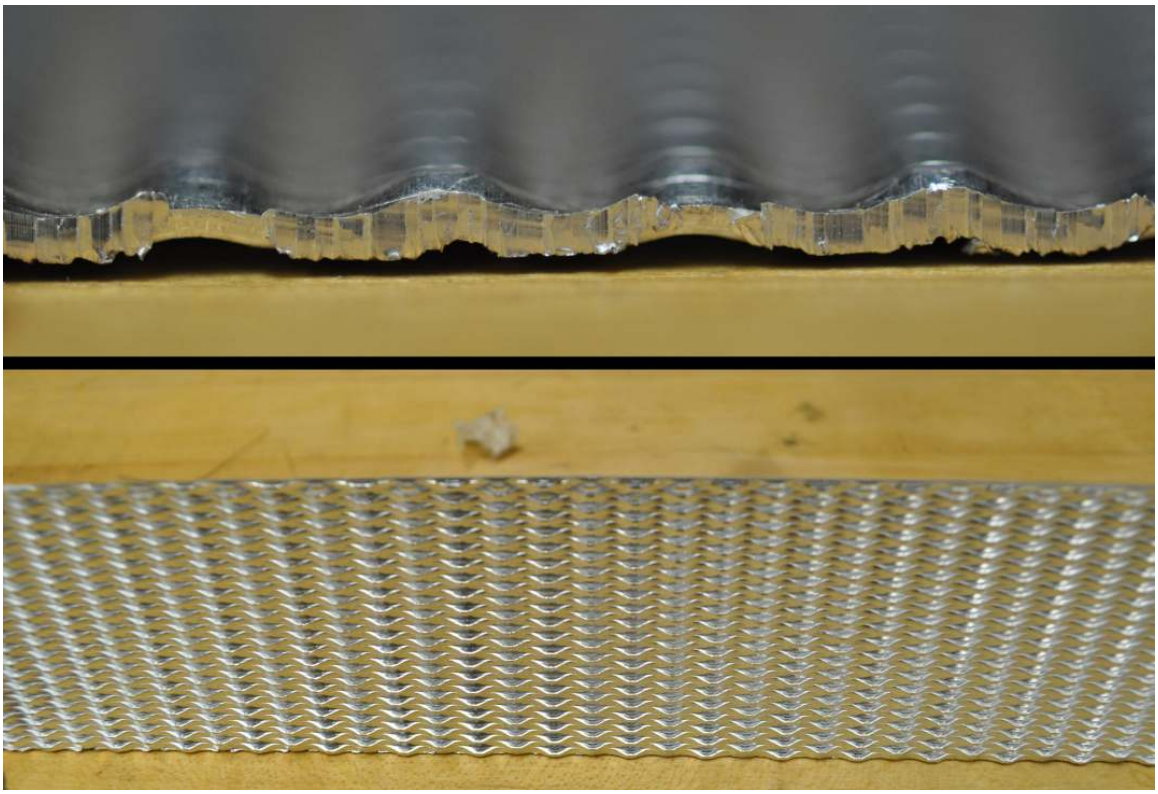

Figure 3.7: Image of surface roughness.

Figure 3.8: New modular test section floor, with measurement instrumentation plug holder at three streamwise positions (actual instrumentation plug not pictured).

terms of the streamwise distance from the inlet of the test section, $x = 16.7$ cm, $x = 57$ cm, and $x = 103.1$ cm, which correspond to stations closest to the inlet, center, and outlet.

3.3 Data Acquisition Techniques

Due to the unique requirements of measuring the wall-normal profiles on a rough surface, a methodology was developed which produced repeatable wall-normal profiles.

The main mode of data collection was with hot-wire anemometers using the same basic interface as that outlined in Estejab [16]. The instrumentation control system is summarized in the flow-chart of figure 3.9.

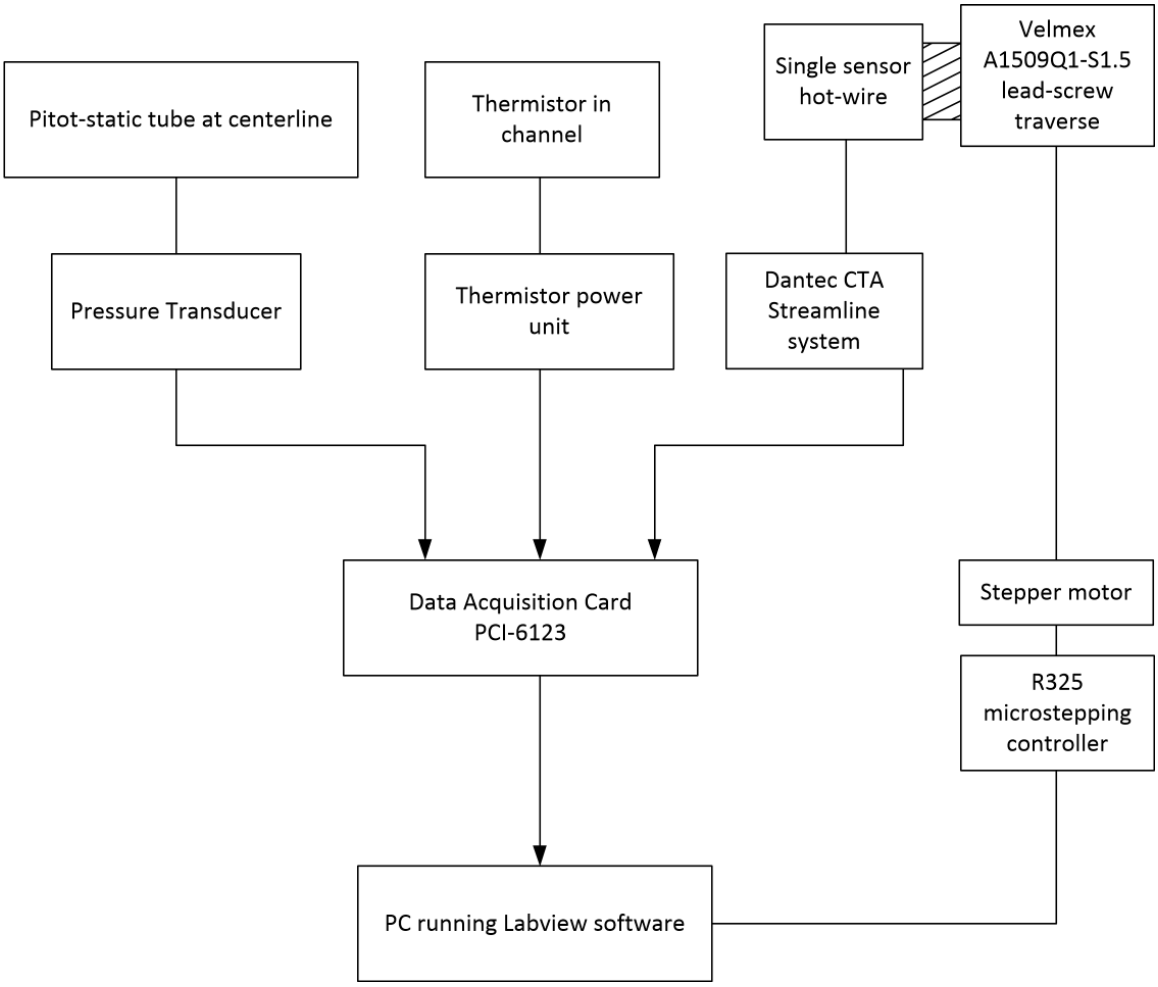

Figure 3.9: Diagram illustrating instrumentation connections used for measurement of wall-normal velocity profiles and calibration.

3.3.1 Pressure Measurement

A Pitot-static tube (Dywer model 167-6) measured the centerline velocity used to calibrate the hot-wire anemometer. The Pitot tube was fixed at the channel centerline and had a diameter of 3.2 mm and a 0.15 mm insertion length. The streamwise aligned element of the tube was 50.8 mm in length.

To determine the static pressure in the channel test section, two static ports were machined into the surface of the instrumentation plug located 25.4 mm downstream from the tip of the Pitot tube and spaced 25.4 mm apart to average any pressure variations caused by the presence of the Pitot tube. The static ports had a diameter of 1.3 mm for a depth of 9.5 mm and were then mated to threaded barbed hose fittings mounted exterior to the channel with a matching diameter of 1.3 mm and a length of 14.2 mm. This produced a length to diameter ratio of 18.

Pressure measurements were acquired using a NIST calibrated Omega PX653-03D5V differential pressure transducer with a 0-746.5 Pascal range.

3.3.2 Venturi Flow Meter

The Venturi flow meter was a Dwyer Instruments Inc. unit (part number 2000-10-VF4) and was delivered with a calibrated pressure gage. The attached gage output both pressure and flow rate increments for each differential pressure. The meter was calibrated up to pressures of 2490.889 Pascals and flow rates of 5.6634 m^3/s. In parallel with the calibrated meter, a second pressure transducer was connected (NIST calibrated Omega PX653-0.5BD5V differential pressure transducer with a $\pm$124.544 Pascal range), and a series of injection velocities were tested. The flow rate was then calculated from the differential pressure and with an application of Bernoulli's equation and compared with the calibrated pressure gage scale. The results indicated that the gage assumed a fully developed turbulent profile, which is in accordance with the factory requirements of a development length before the flow enters the gage. The factor between the calculated flow rates and calibrated pressure gage was 1.2. This allowed for a much more accurate pressure transducer to be used to determine the injection velocity via

$$\dot{V}_{inj} = 1.2 \times A_{g_1} \sqrt{\frac{2\Delta P}{\rho\left((A_{g_1}/A_{g_2})^2 - 1\right)}} \tag{3.3}$$

where $\dot{V}_{inj}$ is the injection gas flow rate, A_{g_i} is the area at the inlet ($i = 1$) and reduced area section ($i = 2$), and ΔP is the pressure drop measured.

3.3.3 Hot-Wire Probes

Single-component velocity hot-wire probes were constructed by soldering Wollaston wire onto Auspex boundary layer type hot-wire prongs. The wire was then etched using a 15 % nitric acid / water solution to expose the 2.5 μm diameter Platinum core wire. A micro-positioner was used to maneuver the wire inside a small bubble of acid formed at the tip of a syringe. Using this method, hot-wires of various lengths can be constructed with great accuracy. For this set of tests, all wires were constructed with a length of $\ell = 0.5$ mm.

The spatial filtering effects of hot-wire anemometers have been studied extensively (see, for example [10, 25, 48, 62]). Typically, if the viscous scaled wire length is $\ell^+ = \ell U_\tau/\nu < 20$, the wire can be considered free of spatial filtering effects. Therefore, any data taken with hot-wires which do not fulfill this requirement must be analyzed with the effects of spatial filtering in mind. Another important factor when choosing the wire geometry is the aspect ratio, $\ell/d > 200$. This parameter controls end-conduction effects. For hot-wires outside these nominal parameters, several correction methods have been developed [23, 25, 39, 60, 62]. However, the basis of these correctional methods relies on assumptions or empirical data made for smooth-wall turbulent flows and therefore they are not directly applicable to the roughness and blowing cases and will not be applied to the data sets in this thesis.

To measure wall-normal profiles of the fluctuating streamwise component of velocity, the single-sensor hot wire probe was mounted on an custom-built traversing system. This system was comprised of multiple components. The linear motion of the probe was provided by a Velmex A1509Q1-S1.5 lead-screw type traverse with a 1 mm per rotation pitch. The lead screw was driven by a Lin Engineering 417/15/03

high-accuracy stepper motor attached through a timing belt with a 2:1 increase in diameter. This motor was controlled using a Lin Engineering R325 micro-stepping controller with resolution of 5 nm per step. To verify the position of the traverse, an Acu-Rite SENC50 E 5/M DD9 0.5 A156 quadrature linear encoder was mounted on the traverse. This system had a 500 nm resolution and stated accuracy of $\pm$ 3 μm. The encoder signal was read by the data acquisition system after first being fed through a USDigital LS7184 quadrature clock converter microchip which then was combined into a single clock pulse signal with a companion TTL direction signal. Thus the probe position could be known with high relative accuracy between points of measurement.

The entire traversing mechanism is mounted on a 152.4 mm (6 inch) diameter instrumentation plug. This plug has additional ports for the centerline Pitot tube and the thermistor probe. Prior to a run, a probe is mounted on the traverse in a reverse orientation from the smooth-wall configuration. This step is necessary because the roughness measurements are performed on the top surface of the channel instead of the bottom. Setting the zero location of the probe was a critical step in the instrumentation process because it allowed the probe to return to a known "home" position, y_h, and then moved back to the centerline, after each run for calibration. Since probe contact with the wall was undesirable, an electrical contact limit switch was designed into the positioning apparatus. The switch carried a 5 Volt signal which was grounded once a bar on the moving portion of the traverse contacted a micrometer mounted on the fixed section of the lead screw drive. By carefully adjusting the micrometer while monitoring the probe position with a Titan Tool Supply Z-axis ZDM-1 measuring microscope, the limit switch could accurately be set to trigger at a specific wall-normal position with $\pm$ 5 μm accuracy.

In roughness studies, the actual wall location is typically offset by an amount y_0 known as the zero-plane displacement [54]. The value of y_0 is typically smaller

than the roughness height itself, k. As y_0 can be determined *a posteriori*, it was therefore not essential to accurately determine the exact wall distance as all probes were traversed to within a single roughness height. The first set of data acquired inside the channel with blowing rig V.1 traversed the probe until destructive contact was made with the wall. While this method did return the exact wall location, it had the negative side effect of requiring many probes to be constructed, which may introduce small probe-to-probe variations. Additionally, a second calibration could not be performed to check the probe drift over the run time (this time was considerable at low speeds, typically 5 hours). Therefore, for the second set of runs with V.2 of the blowing rig, a new method was developed to ensure the probe was traversed within the roughness elements, but remained intact after a run.

The new method involved a line-of-sight tool constructed with a mirror and prism mounted on an adjustable traverse. The unit is placed inside the channel with a section of the modular floor which does not contain the instrumentation plug, removed for access. The user then manually increments the probe into the roughness, using the tool to check if the probe tip is within the roughness elements. Once the user is confident the probe is inside the roughness, the distance from the probe home location to the new, "safe" location is recorded as y_s. The advantage of this method lies in the *in situ* method of setting the zero, with all instrumentation attached in position for a run. It does have the unfortunate consequence of user dependence on final probe location, however, due to the probe homing method, consistency between runs is ensured regardless of the value of y_s chosen.

Hot-wire probe power was provided by a Dantec Dynamics Streamline$^{\text{TM}}$system at an overheat ratio of 1.6. The probe was calibrated before and after each profile measurement at the centerline of the channel using the Pitot probe and wall-pressure tap combination to verify the absence of temperature drift in the HWA probe. The calibration data was fitted using a fourth-order polynomial following correction of the

voltage for flow temperature variation [27]. Details on error sources related to this calibration technique are available in Appendix 5.3.

3.3.4 Data Acquisition

The core of the data acquisition system was a National Instruments PCI-6123 data acquisition card mounted in a desktop PC. This particular card could sample up to 8 analog data channels at 500 kHz and 16-bit resolution simultaneously. In addition to the analog inputs, the card had 8 digital input/output lines and two 24-bit counter-timers which were used for experiment control. All inputs and outputs to the card were completed through a National Instruments BNC-2110 connector block.

Hot-wire profile data were first filtered internally at 30 kHz by the Dantec Dynamics Streamline^{TM}unit and then digitized at 60 kHz by the NI PCI-6123. The acquisition time, T, for each run was adjusted based on the Reynolds number expected to capture at least 100 instances of the largest structures (estimated as $\mathcal{O}(20h)$ [42]) in order to ensure converged statistics. Wall normal profiles were constructed by traversing the probe from within the trough of the roughness element at $y = y_s$ to $y = 1.1h$.

Pressure transducer voltage and thermistor controller voltage were also digitized simultaneous to the hot-wire by the NI PCI-6123. These were sampled at a rate of 10 kHz after filtering by a Krohn-Hite Corporation Model 3905A multichannel filter at a rate of 5 kHz.

3.4 Measurement Procedures

The primary data set acquired for this thesis was taken with blowing rig V.2 and the modular floor design. The bulk of the data investigates matched BR cases across multiple Re, with other runs designed to study specific effects such as very high BR or streamwise development length. During the course of this research wall-normal

profiles of the streamwise velocity were acquired at a multitude of different run conditions. The main goal of this set of experiments was to isolate the effects of roughness relative to roughness and blowing while also investigating their combined effects when subject to changes in Reynolds number, blowing ratio, and streamwise measurement location. The key parameters of this data set are listed in the tables of Section 3.4.

The test cases can be broken down into two large groups based on streamwise location of the measurement. The first set of data is only at the test section center ($x = 57$ cm) and the other set at the inlet ($x = 16.7$ cm) and exit ($x = 103.1$ cm) of the test section. Group one data is summarized in table 3.1 and contains roughness-only runs for the full set of Re investigated, and roughness/blowing runs for the three lowest Re. Group two data in tables 3.2 and 3.3 involve data taken at the inlet and exit of the test section, mainly to investigate the streamwise development of the flow.

The experimental procedures for these runs were imperative to acquiring reliable data sets. Therefore great care was taken in the procedures developed specifically for this set of tests. The primary parameter was determination of the wall location which required two important parameters. The first was setting the "home" location, y_h, of the wire and the second was setting the safe wall distance, y_s, that dictated the distance the wire traveled from the home position into the roughness. The method for setting y_h and y_s are detailed in Section 3.3.3. Prior to inserting a new hot-wire into the TCFF test section, y_h was set external to the tunnel and the value recorded. Then the probe was inserted into the test section. The safe distance was then set with the optical tool. The value of y_s was measured again when any changes to the streamwise measurement location were required. Great care was taken to ensure the hot-wire was inside the roughness elements at the beginning of all measurements. The confirmation of this procedure came in the hot-wire mean flow results. Typically the first few data points acquired by the hot-wire reported negative or zero velocity indicating that the probe was in a recirculation zone behind a roughness element.

Due to the directional sensitivity of the hot-wire probe response, these points were discarded in later analysis.

Prior to starting a run, the injection velocity, U_{inj} was set using an adjustable flap on the inlet to the flow injection centrifugal fan. The flap was opened or closed until the correct injection velocity was reached. It was often a trial and error process to set BR however, as U_m was not known exactly prior to a run. All blowing ratios were checked after a run with the actual U_m and were found to deviate very little from the estimated values. The difference between estimated and actual BR was always less than 1 %.

Before beginning a run, calibration of the hot-wire was performed *in situ* with the probe in the geometric center of the channel. A pitot-static tube was located at the centerline which acquired the mean velocity over a period of 30 to 60 seconds depending on the channel speed (lower calibration speeds required a higher acquisition time) and then this velocity was used to calibrate the mean signal of the hot-wire probe. The number of calibration points depended on the actual run speed. At the lowest run speeds a minimum of 8 different velocities were acquired, and 14 at the highest run speeds.

Directly after calibration, the run was initiated. Each profile was gathered over a series of 70 points, although some points were later removed due to the recirculation zones as described earlier. An acquisition time, T was also selected for each point. An automated Labview^{TM}program read in the profile measurement locations from file and automatically adjusted the probe location between velocity readings. The encoder position was also recorded after moving the probe and was used as the actual wall position of the probe in post-processing. After a run ended, the "home" position was used to re-align the probe with the channel centerline and another calibration was immediately performed.

Table 3.1: Run cases for data gathered at center ($x = 57$ cm) of test section.
NOTE:(†) runs were performed with blowing rig V.1.

Case	Tunnel Freq. (Hz)	U_m (m/s)	U_τ (m/s)	Re_b	Re_τ	$\dot{V}_{injected}$ (m^3/min)	BR (%)	ℓ^+	ΔU^+	y_0 (μm)	k^+	k_s^+	T (sec.)
1	10	3.876	0.196	11,449	659.0	0	0	6.49	1.32	140	12.97	9.73	220
2	10	4.016	0.214	11,666	719.5	0.250	0.102	7.08	3.12	270	14.16	19.63	220
3	10	4.025	0.22	11,664	739.6	0.319	0.130	7.28	3.52	150	14.56	22.95	220
4	10	4.029	0.223	11,495	749.7	0.398	0.162	7.38	3.92	145	14.76	26.82	220
5	10	4.061	0.23	11,552	773.3	0.451	0.182	7.61	4.32	-30	15.22	31.35	
6	10	4.133	0.26	11,092	874.1	1.133	0.450	8.60	7.77	190	17.21	120.4	220
7	10	4.124	0.265	10,859	890.9	1.416	0.563	8.77	8.92	150	17.54	188.54	220
8	10	4.139	0.27	10,629	907.7	1.841	0.729	8.93	9.47	100	17.87	233.65	220
9	23.3	10.721	0.618	31,366	2,078	0	0	20.45	6.92	150	40.90	86.43	220
10	23.3	10.677	0.65	30,714	2,185	0.651	0.100	21.51	8.02	530	43.02	132.7	200
11	23.3	10.679	0.67	30,592	2,253	0.844	0.130	22.17	8.52	550	44.34	161.3	200
12	23.3	10.642	0.695	30,088	2,337	1.036	0.160	23.00	9.42	600	46.00	229.1	200
13 †	23.3	10.603	0.66	30,234	2,219	0.937	0.145	19.66	8.52	-348	43.68	161.3	200
14 †	23.3	10.373	0.68	29,240	2,286	1.535	0.243	20.25	9.42	-145	45.00	229.1	200
15 †	23.3	10.623	0.72	29,427	2,421	2.286	0.353	21.44	10.42	-8	47.65	338.4	200
16	38	18.472	1.131	53,399	3,801	0	0	37.41	9.46	850	74.82	232.7	90
17	38	18.404	1.25	52,518	4,203	1.133	0.101	41.36	11.02	840	82.73	427.7	90
18	38	18.495	1.30	53,471	4,371	1.416	0.126	43.02	11.62	790	86.04	540.4	90
19	38	18.527	1.32	52,284	4,438	1.841	0.163	43.68	11.97	790	87.36	619.4	90
20	52	26.361	1.60	76,380	5,379	0	0	52.95	10.22	1000	105.89	313.0	90
21	63	32.680	2.00	95,382	6,724	0	0	66.18	10.72	1300	132.36	380.4	90

Table 3.2: Run cases for data gathered at $x = 16.7$ cm. NOTE: the wall shear stress for these cases was attempted, but due to the developing nature of the flow, is subject to considerable error compared with the other cases which displayed a much more established log-layer.

Case	Tunnel Freq. (Hz)	U_m (m/s)	U_τ (m/s)	Re_b	Re_τ	$\dot{V}_{injected}$ (m^3/s)	BR	ℓ^+	ΔU^+	y_0 (μm)	k^+	k_s (mm)	T (sec.)
22	38	18.464	1.1	53,753	3,698	0	0	36.40	7.92	170	72.80	127.7	90
23	38	18.144	1.2	53,649	4,034	1.133	0.101	39.71	12.42	100	79.42	738.3	90
24	38	18.219	1.3	53,711	4,371	1.416	0.127	43.02	13.17	100	86.04	989.1	90
25	38	18.200	1.4	53,422	4,707	1.841	0.166	46.33	13.42	100	92.65	1,090	90

Table 3.3: Run cases for data gathered at $x = 103.1$ cm.

Case	Tunnel Freq. (Hz)	U_m (m/s)	U_τ (m/s)	Re_b	Re_τ	$\dot{V}_{injected}$ (m^3/s)	BR	ℓ^+	ΔU^+	y_0 μm	k^+	k_s	T (sec.)
26	10	4.049	0.20	11,879	672.4	0	0	6.62	1.29	750	13.24	9.62	220
27	10	4.280	0.24	11,341	806.9	1.133	0.434	7.94	6.92	480	15.88	86.43	220
28	10	4.313	0.26	11,154	874.1	1.416	0.539	8.60	8.27	600	17.21	146.3	220
29	10	4.486	0.28	11,499	924.6	1.841	0.673	9.10	9.32	830	18.20	220.4	220
30	38	18.788	1.23	53,456	4,135	0	0	40.7	10.60	920	81.40	363.0	90
31	38	19.345	1.39	53,972	4,673	1.133	0.096	46.0	12.27	780	91.99	696.3	90
32	38	19.384	1.47	53,727	4,956	1.416	0.120	48.8	13.07	900	97.55	951.3	90
33	38	19.362	1.50	53,162	5,043	1.841	0.156	49.6	13.47	880	99.27	1,112	90
34	63	33.344	2.2	95,963	7,396	0	0	72.8	12.02	1,050	145.6	631.6	90

Table 3.4: Smooth-wall comparison cases at center of test section ($x = 57$ cm).

Case	Tunnel Freq. (Hz)	U_m (m/s)	U_τ (m/s)	Re_b	Re_τ	ℓ^+	T (sec.)
35s	10	4.209	0.198	12,403	665.7	5.90	220
36s	33	15.881	0.651	47,981	2,189	21.33	180
37s	45	22.987	0.895	69,586	3,009	29.32	90
38s	63	33.344	1.258	101,234	4,229	41.21	90

3.5 Wall Shear Stress

Direct measurement of wall shear stress to determine U_τ was not possible in the present case. Therefore, for this set of experiments, the so-called "Clauser chart" method was used to determine the friction velocity [12]. This method has precedence in rough-walled turbulent boundary layers [17, 32, 38, 48, 59], but it has been noted to lack agreement with other methods [1]. This has resulted in multiple improvements upon the basic Clauser method [1, 49] being proposed. However, the structure of any of these methods relies on universality of the velocity-defect law. For the purposes of these experiments at the lower Reynolds numbers ($Re_\tau < 3000$), the method described in Perry et al. (2009)[48] was modified by utilizing the streamwise Reynolds stress to determine y_0 whereby a value was chosen so that each profile tends towards zero at the same location as the smooth wall cases at similar values of Re_τ. This method proved very reliable at producing values of y_0 which also collapsed the mean profile data. An iterative procedure was then used to determine U_τ by matching the slope of the mean velocity profile in the logarithmic region to that of the smooth-walled case. At higher Re_τ the near-surface peak in streamwise Reynolds stress was not sufficiently resolved to extrapolate the profile. However, it was assumed that the log region in the mean flow was large enough in this high-Re range to fit the profiles accurately using equation 3.4 with a von Kármán constant of $\kappa = 0.39$ and log-law additive constant of $B = 4.42$ [43].

$$U^+(y) = \frac{1}{\kappa} ln(y^+) + B - \Delta U^+(k^+, L^+) \tag{3.4}$$

3.5.1 Validation of Clauser Chart

To validate the results obtained with the Clauser chart method described above, a simple control volume momentum balance was performed on the mean flow which

took into account the entrance and exit mass flux to the test section and the measured pressure drop along the test section. A diagram of this approach is shown in figure 3.10.

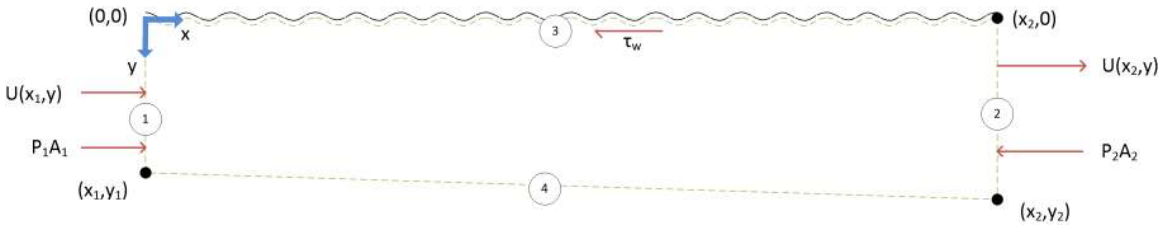

Figure 3.10: Diagram of control volume inside channel test section with roughness and blowing. The spanwise direction of the control volume is into and out of the paper with unit width, w

To complete this control-volume analysis, several simplifying assumptions had to be made. Namely, that no flow crossed the mean streamlines from the inlet and outlet locations of maximum velocity. This makes up the bottom of the control volume, surface 4, in figure 3.10. No mass crosses this boundary, and no forces act on it. Furthermore, the control volume is placed infinitely close to the roughness at surface 3, so that the only effect on the flow is the wall shear force. The pressure gradient in the channel is represented as a pressure acting on the control volume at surfaces 1 and 2. The y-momentum equation is of little use here as no forces act in that direction besides the mass addition due to blowing. However, all mass must leave the control volume via surface 2, so the effect of blowing is accounted for by the measured velocity profiles at 2.

$$\Sigma F_x = -\tau_w A_3 - P_2 A_2 + P_1 A_1 = \int_{CS} \overrightarrow{V} \rho \overrightarrow{V} \cdot \hat{n} dA \tag{3.5}$$

$$= \rho \left[\int_{A_1} U_1(y)(U_1(y) \cdot \hat{n}_1) dA_1 + \int_{A_2} U_2(y)(U_2(y) \cdot \hat{n}_2) dA_2 \right] \tag{3.6}$$

$$= \rho w \left[\int_0^{y_{m_2}} U_2^2 dy - \int_0^{y_{m_1}} U_1^2 dy \right] \tag{3.7}$$

$$\vdots \tag{3.8}$$

$$\tau_w = \frac{-1}{x_2} \left[\rho \int_0^{y_{m_2}} U_2^2 dy - \rho \int_0^{y_{m_1}} U_1^2 dy + P_2 y_{m_2} - P_1 y_{m_1} \right] \tag{3.9}$$

Here U_1 and U_2 are the entrance and exit velocity profiles, respectively. All terms are assumed not to vary in the z or spanwise direction near the centerline. Thus, the profiles become a function of x and y only. To acquire the pressure drop at the entrance (P_1) and exit (P_2), a series of experiments were carried out in which the channel test section was modified to accept two Dwyer pitot-static tubes (part number 166-12-CF). These pitot-static tubes were fitted in the side-wall of the channel at the centerline. Each probe was carefully aligned to read the streamwise dynamic pressure with the static pressure ports in the same streamwise location as the point of the hot-wire measurements. Furthermore, the tubes were 304.8 mm long and thus the sensing tip was inside the middle 1/3 of the channel.

With the use of these pitot-static tubes, and the static ports on the floor in the center of the test section, the pressure gradient could be found at three different locations in the test section. This allowed the analytical model derived in equation 3.9 to be compared with the values from the Clauser-chart method between any two of the three locations. Because the flow was not sufficiently developed at the inlet to the test section ($x = 16.7$ cm) these points are ignored.

Determination of the wall shear using equation 3.9 is shown in figure 3.11 along with the Clauser chart values averaged between the center and exit. There was significant scatter in the calculated values of U_τ, and only two points are available for each Reynolds number. This was most likely due to the very small pressure measurements which were typically less than 15 Pascals. The benefit of this analysis is that it confirms the Clauser chart values should increase with increased blowing. In fact, for the low Re cases, the calculated U_τ appear to follow the Clauser U_τ well.

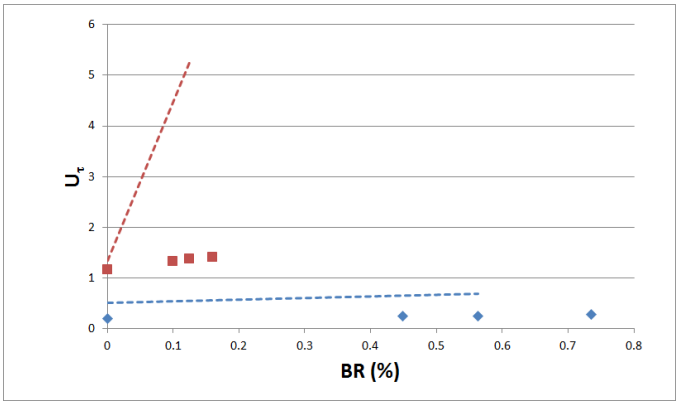

Figure 3.11: Calculated and Clauser chart friction velocity comparison. U_τ found between center (x = 57 cm) and rear (x = 103.1 cm) of test section is shown as dashed lines. The blue points are for $Re_\tau \approx 700$ and the red points are $Re_\tau \approx 4000$.

Chapter 4

Results and Discussion

The bulk of this chapter focuses on the matched blowing ratio cases. These provide the most direct comparison of blowing effects across a range of Reynolds numbers. Also included are several test cases to study the limits of wall similarity with respect to increasing BR and streamwise flow development. All cases have been summarized in table 4.1, along with the symbol designation used in Section 4.1. The results are broken down into three main sections, time averaged statistics are presented in Section 4.1, the frequency spectra are presented in Section 4.2, limitations on self-similarity due to blowing are presented in Section 4.3, and analysis of streamwise flow development is presented in Section 4.4.

4.1 Time-Averaged Statistics

Observing the time-averaged statistics for the roughness and combined roughness/blowing effects allows for direct comparison of modifications to the flow structure. The first section, Section 4.1.1, contains the wall-normal, streamwise, time-averaged statistics such as the coefficient of friction, roughness function, and velocity profiles for each run condition. This is followed by a section discussing the turbulence statistics in Section 4.1.2, which contains the Reynolds stress plots and higher-order statistics such as the skewness, kurtosis, and third-order moments.

Table 4.1: Symbols for Blowing Rate according to Reynolds number at $x = 57$ cm. NOTE:(†) runs were performed with blowing rig V.1.

Case	Tunnel Freq. (Hz)	Re_τ	BR (%)	Symbol
1	10	659	0	◇
2	10	719.5	0.1	□
3	10	739.6	0.13	△
4	10	749.7	0.16	○
5	10	773.3	0.18	☆
6	10	874.1	0.43	▷
7	10	890.9	0.56	+
8	10	907.7	0.73	◁
9	23.3	2,078	0	◇
10	23.3	2,185	0.1	□
11	23.3	2,253	0.13	△
12	23.3	2,337	0.16	○
13 †	23.3	2,219	0.145	☆
14 †	23.3	2,286	0.24	▷
15 †	23.3	2,421	0.35	+
16	38	3,801	0	◇
17	38	4,203	0.1	□
18	38	4,371	0.13	△
19	38	4,438	0.16	○
20	52	5,379	0	◇
21	63	6,724	0	◇
35s	10	665.7	0	× or −
36s	33	2,189	0	× or −
37s	45	3,009	0	× or −
38s	63	4,229	0	× or −

4.1.1 Mean Flow

The variation of the friction coefficient as a function of bulk Reynolds number is presented in figure 4.1. In this case, the friction coefficient is defined as

$$C_f = \frac{\tau_w}{(0.5\rho\langle U\rangle^2)} \tag{4.1}$$

where τ_w is the wall shear stress, ρ is the density, and $\langle U \rangle$ is the area-averaged or bulk velocity

$$\langle U \rangle = \frac{1}{y_m} \int_0^{y_m} U(y) dy \tag{4.2}$$

where y_m is the wall-normal location of the maximum velocity. The bulk velocity was calculated in this way to account for any slight asymmetry in the mean velocity profile which was induced by roughness and/or blowing. By definition, for the smooth wall cases, $y_m = h$ and the bulk velocity returns to its usual form. Generally, the asymmetry present in the roughness and blowing cases was small, with $U_m = U(y_m)$ found to be within 2 % of $U_{cl} = U(h)$ in location and value.

With respect to the values of C_f seen in figure 4.1, the deviation of C_f for the $BR = 0\%$ condition from the smooth-wall curve follows typical surface roughness behavior. The lowest Reynolds number measured appears to be transitional and the highest Reynolds numbers measured are approaching fully rough conditions. Interestingly, for non-zero BR, the skin friction was observed to increase with increasing BR and the Reynolds number behavior of C_f is similar to that expected for increasing roughness effects. This result is in contrast to results from other blowing studies with smooth-walls as well as prior work on turbulent boundary layers with roughness and blowing [21, 57, 67], where any amount of flow injection was observed to reduce skin friction when roughness was present. One potential explanation for this deviation from prior results is the surface geometry. In the present study, the roughness is nominally two-dimensional, whereas prior work focused exclusively on three-dimensional roughness geometries such as mesh roughness and sintered metal surfaces. The near-wall flow of two-dimensional roughness can be expected to be composed of relatively spanwise-coherent shear-layers separating from the roughness elements. The addition of momentum transfer from the blowing could disrupt these shear layers, resulting in enhanced momentum transfer with the surface.

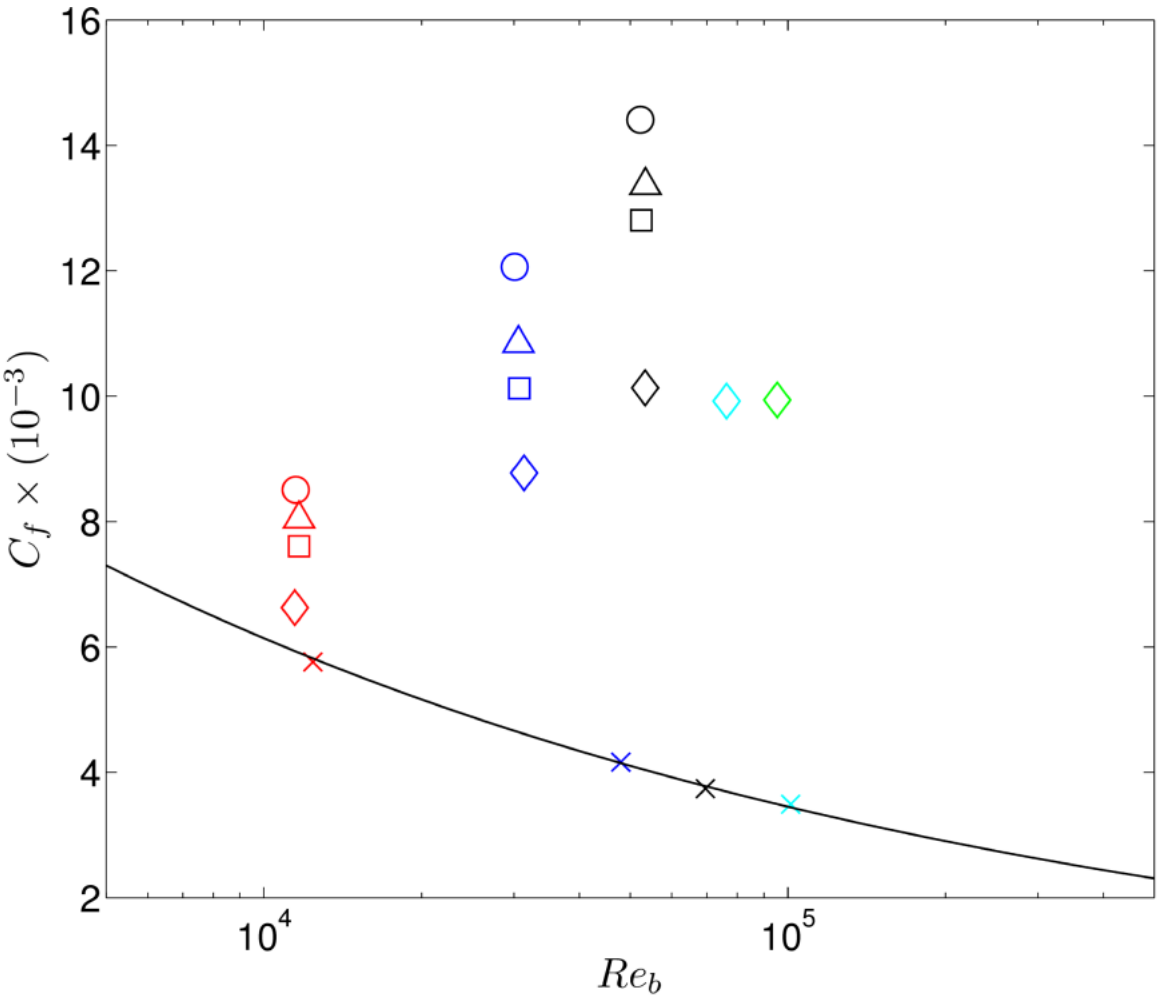

Figure 4.1: *Coefficient of friction as a function of bulk Reynolds number for matched BR. Symbols as in table 4.1. The solid black line is the smooth-wall correlation of Dean (1978) [13]* $0.073(2Re_b)^{-0.25}$

Symbols as in table 4.1.

The mean velocity plots are first presented for matched blowing ratios, across all Reynolds number, and at $x = 57$ cm. Scaling first with outer flow variables is shown in figure 4.2. In this plot the defect of the mean flow due to the roughness is clearly evident. This plot also gives a general sense of the flow behavior in the outer-layer due to roughness and blowing over a two-dimensional roughness. Additional bias of the flow away from the wall is seen, which is a result reproduced if an increase in k^+ is made due to either larger Re or change in roughness element height, k. This leads to the preliminary observation that the effect of blowing is to act as additional

roughness with respect to the mean flow.

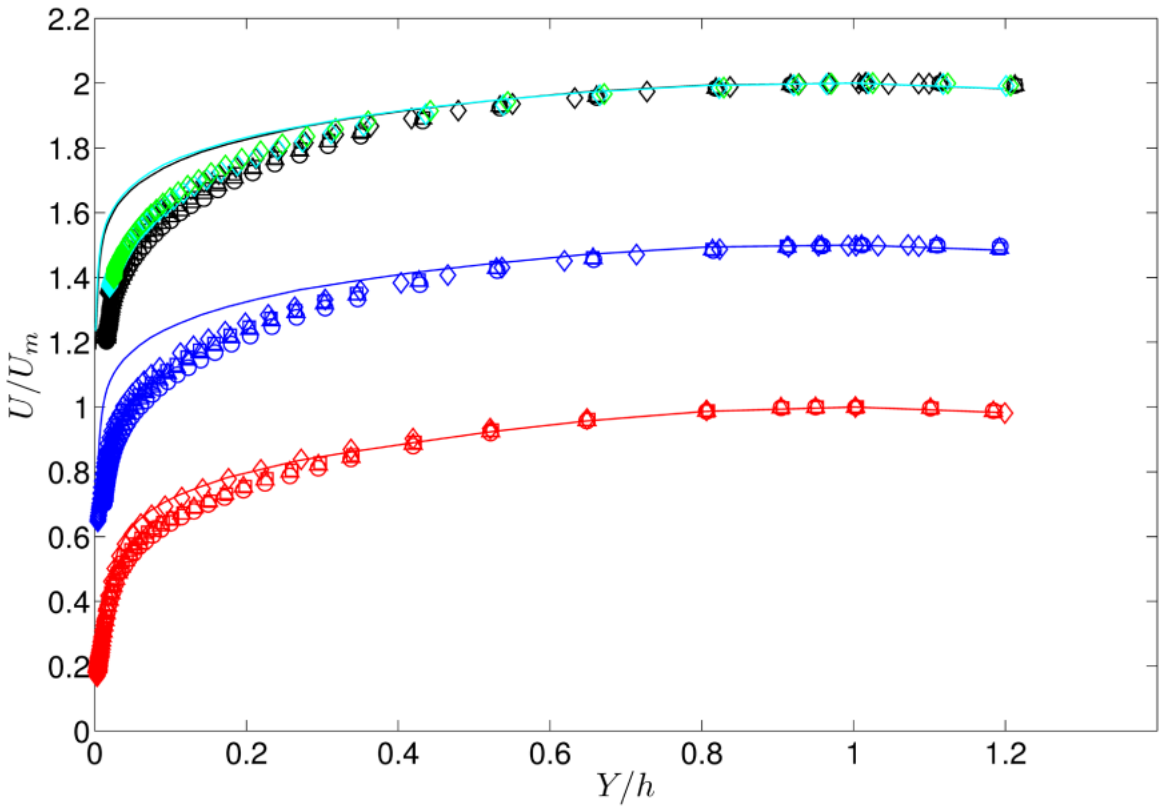

Figure 4.2: *Outer-scaled mean velocity profiles for the matched BR run cases. Solid lines indicate smooth-wall cases at matched* Re_τ*. The* $Re_\tau = 2000$ *cases (blue) are offset by 0.5 units on the y axis, and* $Re_\tau = 3000$ *and greater cases (black, cyan, and green) are offset by 1 unit for clarity. Symbols as in table 4.1.*

The scaling parameter chosen for the outer flow is U_m, which is the maximum velocity at some distance away from the roughness, y_m, is typically not at the geometric centerline of the channel. The wall scaling parameter remains the nominal channel half-height, $h = 50.8$ mm, instead of y_m. For the smooth-wall cases, $y_m \equiv h$, and scaling with h allows for a direct comparison of the rough and rough/blowing cases to the smooth-wall cases as well as insight into the asymmetry of the flow. As noted for figure 4.1, the asymmetry due to roughness and blowing is not large and is not readily apparent in figure 4.2.

Next, the inner-scaled mean velocity plots are presented in figure 4.3. Due to the methodology used to determine U_τ, the inner-scaled mean plots reflect the inde-

pendence of the outer layer on the wall boundary conditions for all blowing ratios investigated.

Focusing on the $BR = 0$ cases, the expected increase in ΔU^+ with increasing Reynolds number is apparent. This corresponds to the increase in wall shear stress due to increasing k^+. Furthermore, upon the addition of blowing a further increase in ΔU^+ at fixed Reynold number is seen. Thus, as with the outer-scaled flow and C_f behavior, the impact of blowing on the mean flow appears to be an increase in roughness effects.

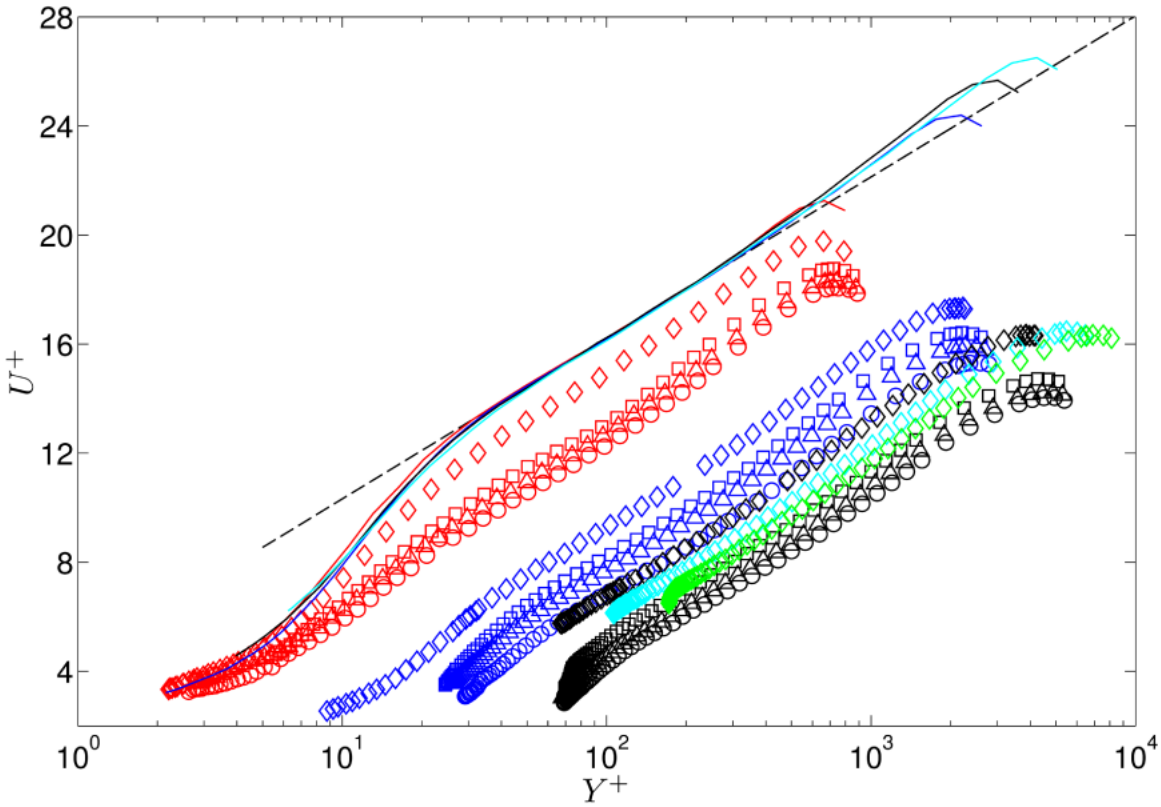

Figure 4.3: *Inner-scaled velocity plot for matched blowing ratios. Symbols as in table 4.1.*

Further reflecting the behavior of blowing on the mean flow, the defect-scaled plots are presented in figure 4.4. Collapse among all smooth, rough, and rough with blowing cases is evident across all Reynolds numbers. The effects of blowing and roughness appear confined to the near-wall region, with these boundary conditions

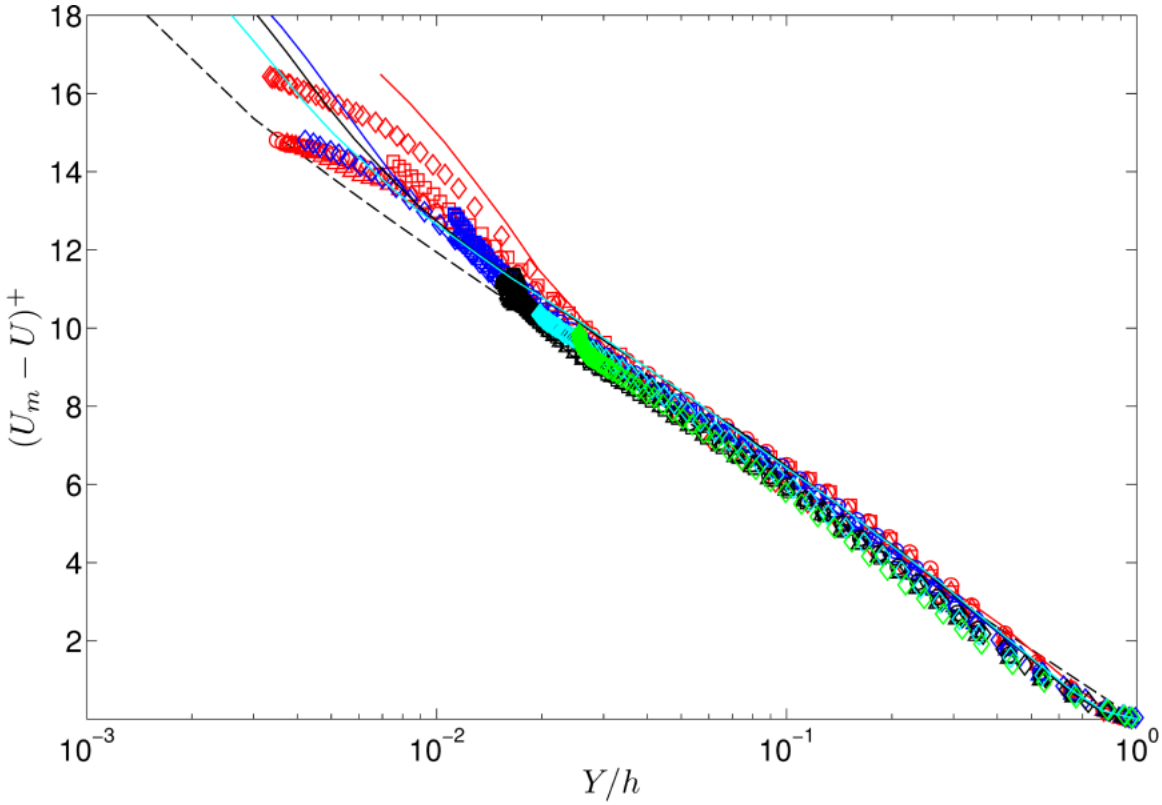

Figure 4.4: *Defect velocity plot for matched blowing ratio cases. Symbols as in table 4.1.*

affecting the outer flow by setting of the wall shear stress, consistent with Townsend's hypothesis.

To track the effects of changing k^+ on ΔU^+ these two effects are plotted in figure 4.5(a). Quantifying this value can help to determine the roughness condition, be it fully rough or transitional, as these types of roughness display different ΔU^+ behaviors. The results in figure 4.5(a) display the wide range of k^+ values from 13 to 132 (k_s^+ values of 9.7 to 380) of this study. Comparing the $BR = 0$ cases with the sand-grain roughness data of Prandtl and Schlichting (1934)[52], the data follow a similar pattern with transitional behavior seen for the lowest Reynolds number. For the $k^+ \gtrapprox 60$ the ΔU^+ behavior follows the expected logarithmic increase for fully rough conditions with $k_s \approx 1.8k$. As mentioned previously, an increase in BR results in an increase in ΔU^+, analogous to an increase in roughness effects. However, these

results show that this effective increase cannot simply be treated as an increase in k, as the $BR > 0$ cases follow separate $\Delta U^+(k^+)$ trends for each individual BR. Following the analogy for roughness, this equates to a change in overall roughness geometry and not simply an increase in k.

From the plot in figure 4.5(a), a clear dependence on the blowing ratio is evident, and an attempt to correlate the blowing ratio to the increase in ΔU^+ resulted in the following empirical correlation

$$\Delta U^+_{corrected} = \Delta U^+(1 - 1.2(BR\%)) \tag{4.3}$$

where the blowing ratio is formulated as a percentage

$$BR\% = \frac{U_{inj}}{U_m} \times 100. \tag{4.4}$$

As shown in figure 4.5(b), the ΔU^+ values for $BR > 0$ modified with equation 4.3 collapse onto the $BR = 0$ curve for the highest, fully rough Reynolds numbers. Although the formulation of the correction is simplistic, it suggests that the effects of roughness and blowing can potentially be treated in succession, at least for the mean flow.

This result encouraged extension of the correction to account for blowing in the friction coefficient. First noting that $C_f = 2\langle U^+ \rangle^{-2}$, equation 4.3 can be combined with the log-law formulation for a rough-walled surface,

$$U^+(y) = \frac{1}{\kappa} \ln(y^+) + B - \Delta U^+(k^+, L^+) \tag{4.5}$$

to account for blowing effects such that

$$C_{f_{blowing}} = 2 \left(\sqrt{\frac{2}{C_f}} - \Delta U^+ \left[\frac{1.2BR}{1 - 1.2BR} \right] \right)^{-2} \tag{4.6}$$

where C_f and ΔU^+ are the values for the rough-walled case at a particular Reynolds number and BR is again expressed as a percent. This correction, although simple, appears to capture the effects of blowing as shown in figure 4.6. The correction is more effective for the fully rough data and suggests that the effects of roughness and blowing may be treated in succession when considering mean flow quantities.

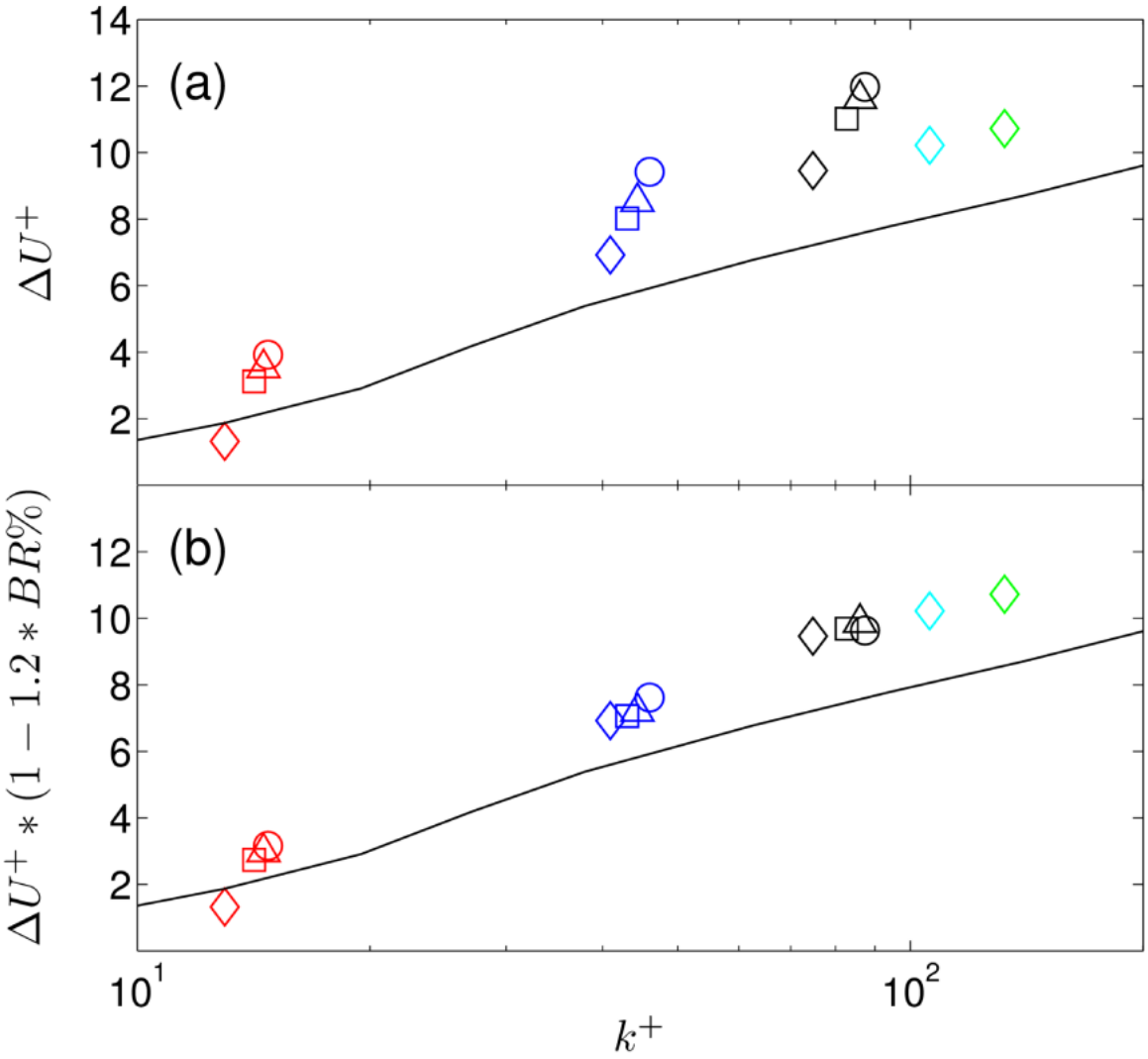

Figure 4.5: ΔU^+ *as a function of the roughness Reynolds number, the solid line indicates the sand-grain roughness of [52]. Symbols as in table 4.1.*

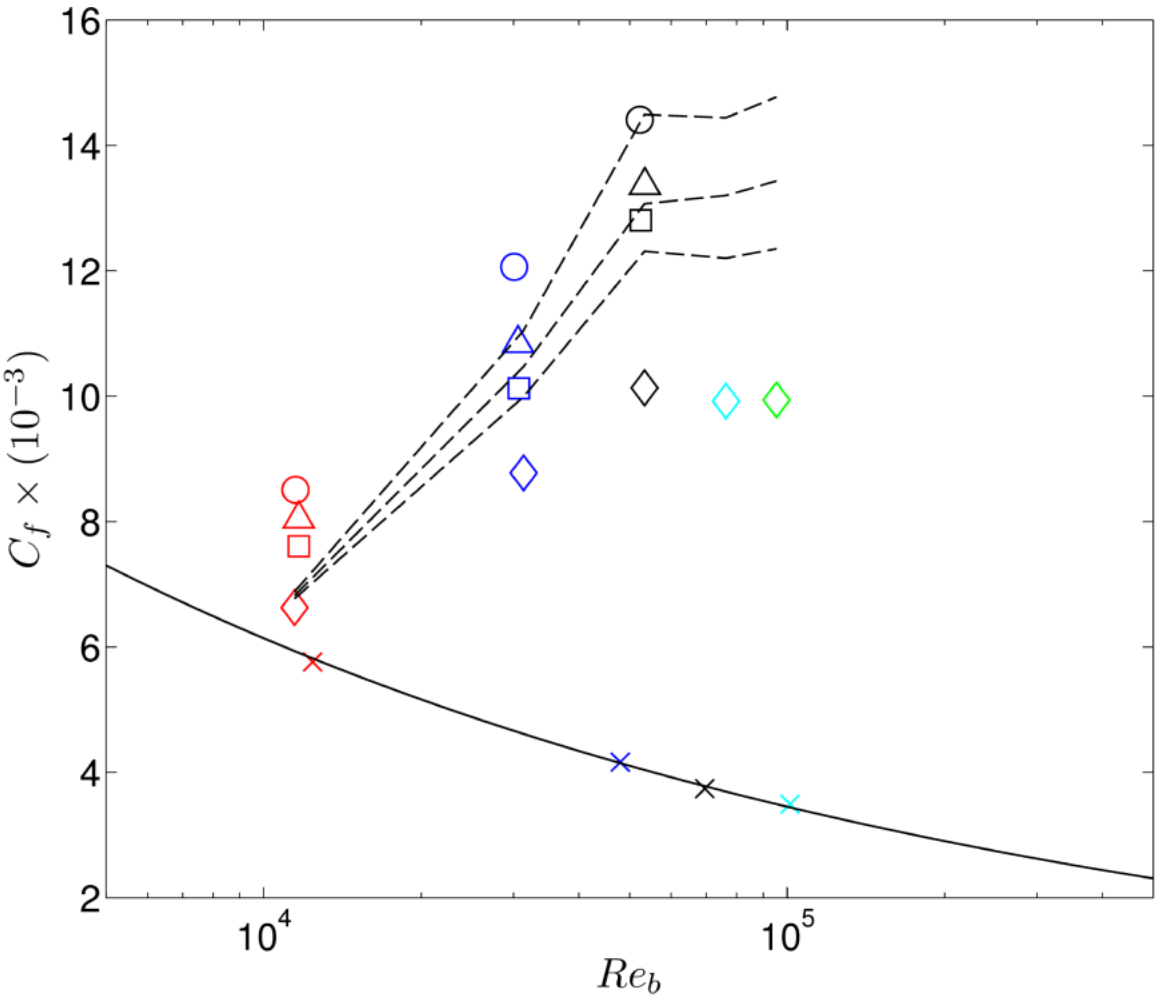

Figure 4.6: Coefficient of friction for matched BR cases. The correction of equation 4.6 has been applied for the three blowing ratios ($BR = 0.1, 0.13, 0.16\%$) and plotted as the dashed lines. Symbols as in table 4.1.

4.1.2 Turbulence Statistics

The previous section outlined how blowing effects in the presence of roughness are analogous to an increase in the roughness Reynolds number. This section focuses on the changes in the turbulence statistics due to the application of roughness and blowing boundary conditions. In particular, the streamwise Reynolds stress will be investigated.

In figures 4.7 and 4.8, the inner-scaled and outer-scaled Reynolds stress profiles are plotted. It is noted here that the highest Reynolds number cases may be subject

to spatial filtering [25] which will artificially reduce the magnitude of the streamwise Reynolds stress. Spatial filtering effects can be considered minimal below $\ell^+ \approx 20$ [37], which is the case for the two lowest Reynolds numbers. For the higher Reynolds number cases, spatial filtering effects were confined to the near-wall region [62].

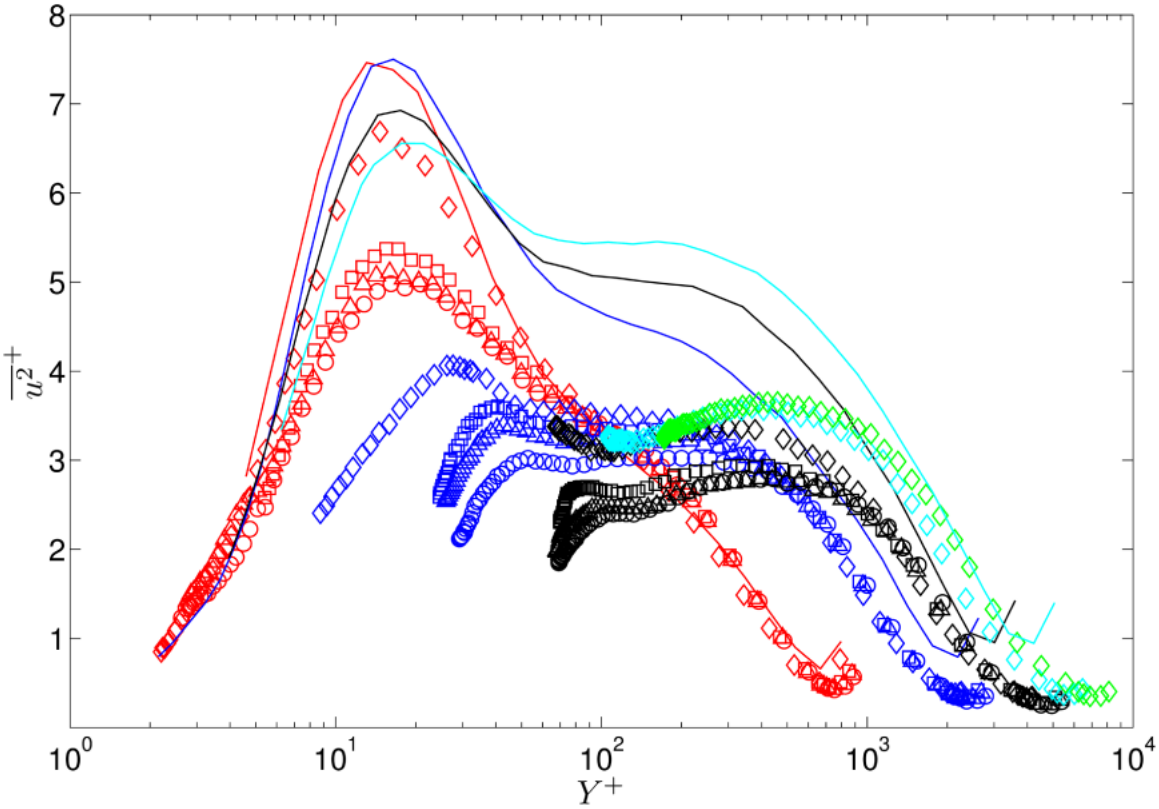

Figure 4.7: *Inner-scaled Reynolds stress for matched blowing ratios. Symbols indicate blowing rate and color indicates Reynolds number, see table 4.1.*

Figure 4.7 shows that the surface roughness serves to decrease the relative magnitude of the near-wall peak with respect to the smooth-wall cases. The $BR > 0$ cases exhibit similar trends, with increasing BR further reducing the inner-peak magnitude. For the lowest Reynolds number case, at $k^+ \approx 13$ the inner peak appears at $Y^+ \approx 15$ which suggest that the near-wall turbulence production cycle in this transitionally rough regime is largely similar to that for smooth-walled flows. Observing the fully rough cases, $k^+ > 70$, the near-wall peak moves away from the wall in inner units. This is consistent with the peak location scaling with the physical scale of

the roughness elements, rather than the viscous length, ν/U_τ. The effect of this is demonstrated in figure 4.8, which shows that for $BR = 0$ and $k^+ \geq 40$, the near wall peak occurs at $Y/h = 0.01$ ($Y \approx 0.5k$). When blowing is added, the peak moves to $Y \approx k$, with a slight increase in the distance from the wall observed with increasing BR.

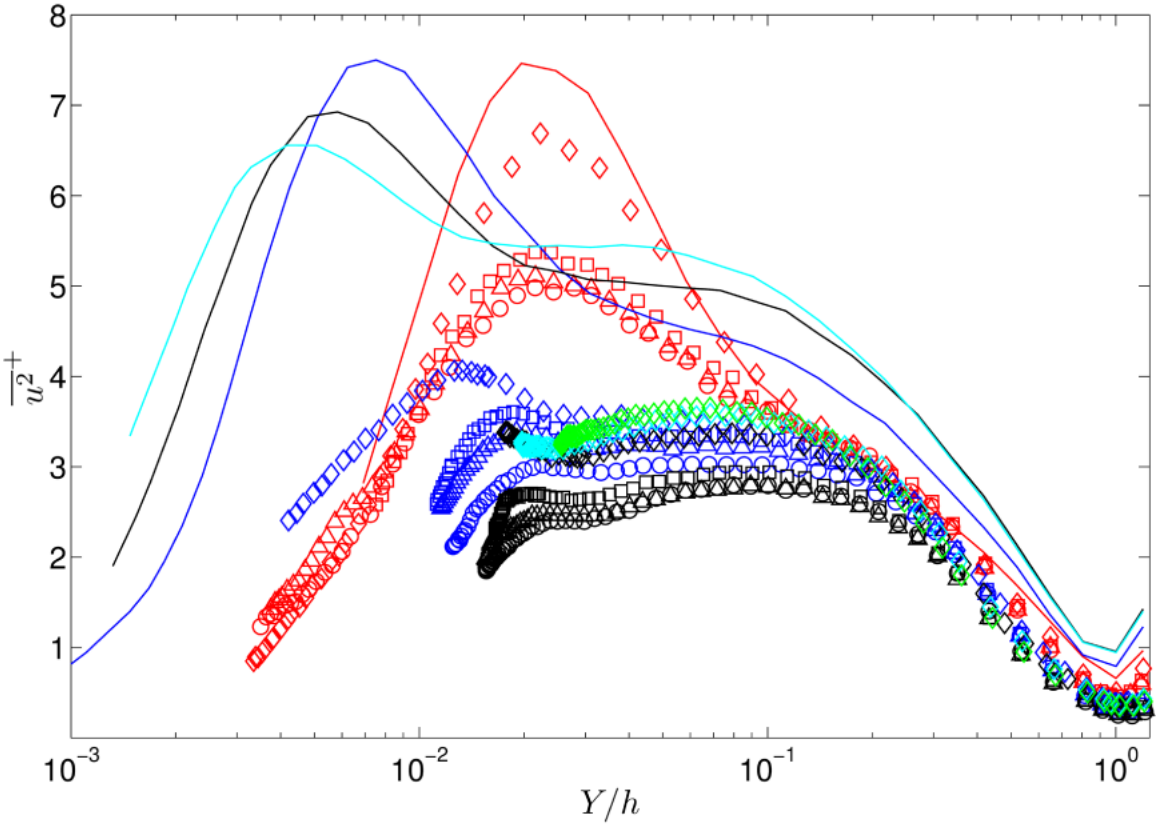

Figure 4.8: *Outer-scaled Reynolds stress for matched blowing ratios. Symbols indicate blowing rate and color indicates Reynolds number, see table 4.1.*

As with the mean flow, the addition of blowing therefore appears to act as an increase in surface roughness. Figure 4.7 reveals that the effects of roughness and blowing on u^{2+} are greatest in the near-wall region with little effect on the outer flow except through determination of U_τ. The roughness and blowing behavior observed for u^{2+} is therefore similar to that of the mean velocity profiles in section 4.1.1, which followed the behavior predicted by Townsend's hypothesis.

The adherence to Townsend's hypothesis is related to the relative height of the

roughness elements used in this study of $h/k = 51$, which exceeds the minimum value of $h/k > 40$ cited by Jiménez (2004) [26] for validity of Townsend's hypothesis. Thus it is expected that the effect of roughness should be confined to the inner layer and thus wall similarity should hold for the Reynolds stress as well as the mean flow. As shown in figure 4.8, the results for the $BR = 0$ cases do not collapse with the smooth-walled profiles in the outer layer, which themselves collapse using this scaling for $Re_\tau \geq 3000$. The lack of agreement can be explained by observing that the flow over the roughness is still developing, whereas it is fully developed for the smooth-walled cases. However, as is shown in figures 4.9 and 4.10, the three highest Reynolds number cases, with $BR = 0$ are seen to be self-similar, which describes consistency among the roughness and roughness/blowing cases, and collapse within the outer layer for $Y/h > 0.1$. The addition of blowing was found to follow this scaling behavior for $Y/h > 0.5$, which is well into the outer layer.

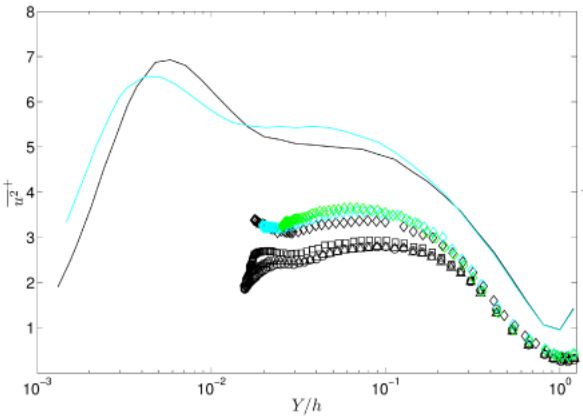

Figure 4.9: *Outer-scaled Reynolds stress for three highest Reynolds number cases. For symbols see table 4.1.*

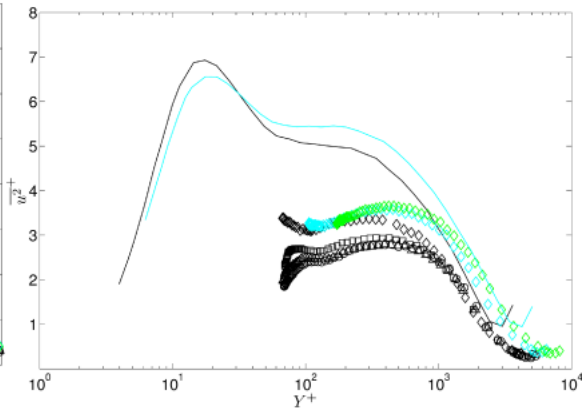

Figure 4.10: *Inner-scaled Reynolds stress for three highest Reynolds number cases. For symbols see table 4.1.*

4.1.3 Higher-Order Statistics

The skewness factor is defined as the third order central moment normalized with the second order variance

$$S_u = \frac{\overline{u^3}}{\left(\overline{u^2}\right)^{3/2}}. \tag{4.7}$$

The skewness is displayed for all Reynolds numbers and the cases with matched blowing ratios in figure 4.11. Observing the $BR = 0$ cases, some deviation is seen from collapse across the Reynolds number range. It appears that at the lowest Reynolds number, the skewness zero crossing occurs much sooner ($Y/h \approx 0.02$) than the other roughness cases ($Y/h \approx 0.1$). This is interesting because collapse is expected across all roughness run cases, as was the case for the mean velocity defect plot and the outer-scaled Reynolds stress. This is contrary to other high-Reynolds number roughness studies for turbulent boundary layers where similarity is seen far away from the wall for the Skewness factor at similar values of k^+ to those in this study [3, 17].

With regard to the blowing effects on skewness, there appears to be a positive increase in the skewness factor near the wall as blowing is increased. This is especially evident for the lowest Reynolds number case. As noted by Flack et al. (2005), positive skewness near a rough wall may reflect for higher momentum fluid being swept into the near wall region [17]. The same conclusion may also hold true for the cases of $BR > 0$ where the blowing is essentially acting as a sink for additional momentum and mixing near the wall. At any rate, for the lowest Reynolds number case at $Re_\tau \approx 700$, poor collapse is seen regardless of the blowing condition. This reflects the results from the Reynolds stress plots for $Re_\tau \approx 700$, which did not collapse with the higher Re_τ roughness and blowing cases. The higher Re cases display self-similarity, but do not show collapse with the smooth wall data until outside of $Y/h > 10^{-1}$.

The flatness or kurtosis factors for the same cases as in figure 4.11 are presented

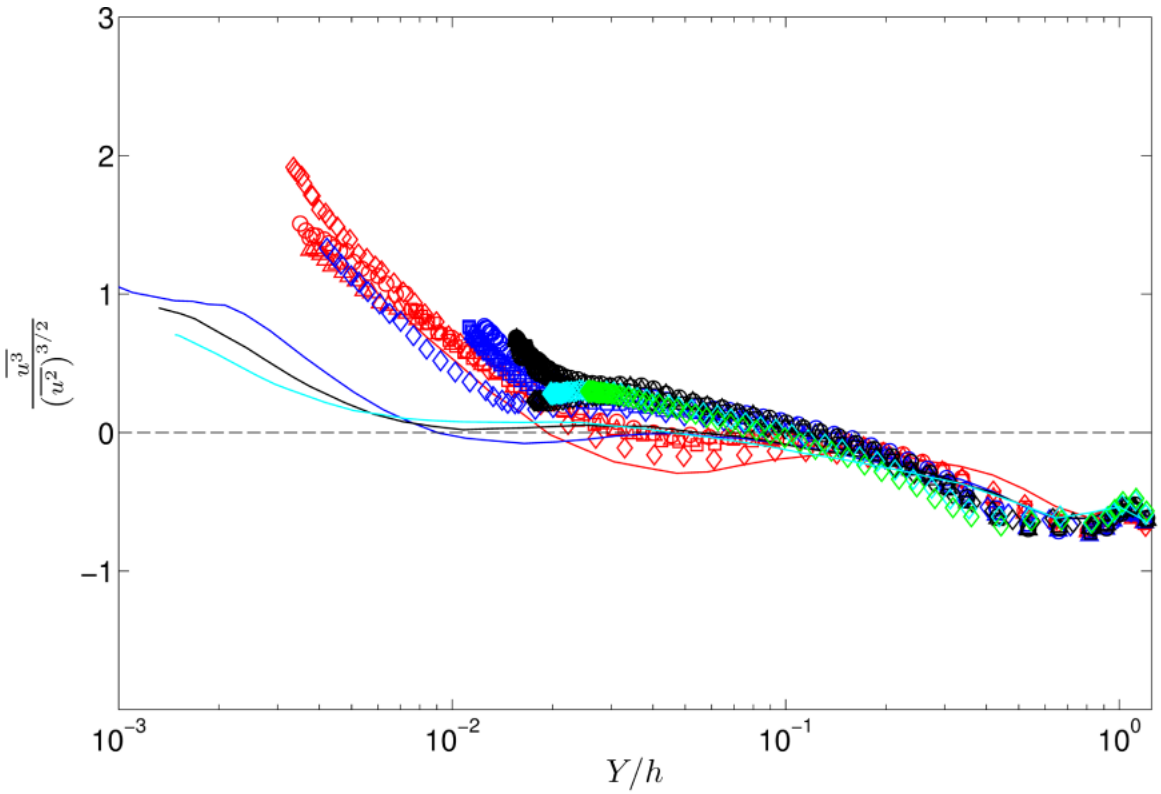

Figure 4.11: *Skewness factor S_u for roughness, and matched blowing cases. Dashed line indicates zero-crossing location. Symbols as in table 4.1.*

in figure 4.12, where the flatness is defined here as

$$F_u = \frac{\overline{u^4}}{\left(\overline{u^2}\right)^2}. \tag{4.8}$$

The flatness factor appears to collapse well regardless of Reynolds number and blowing ratio. As in the skewness plot, the $Re_\tau \approx 700$ cases are seen to deviate slightly from the higher Re_τ cases near the wall. However, the low Re_τ case does agree well with the flatness factor for the smooth wall, $Re_\tau \approx 700$, case. It appears that the flatness is relatively unaffected by roughness and blowing to any significant degree, except very close to the wall, near $Y/h < 0.04 = 2(k/h)$.

Bakken et al. (2005) notes that the sign of the third-order moment u^{3+} near the wall can be related to ejection and sweep events [7]. Furthermore, the authors

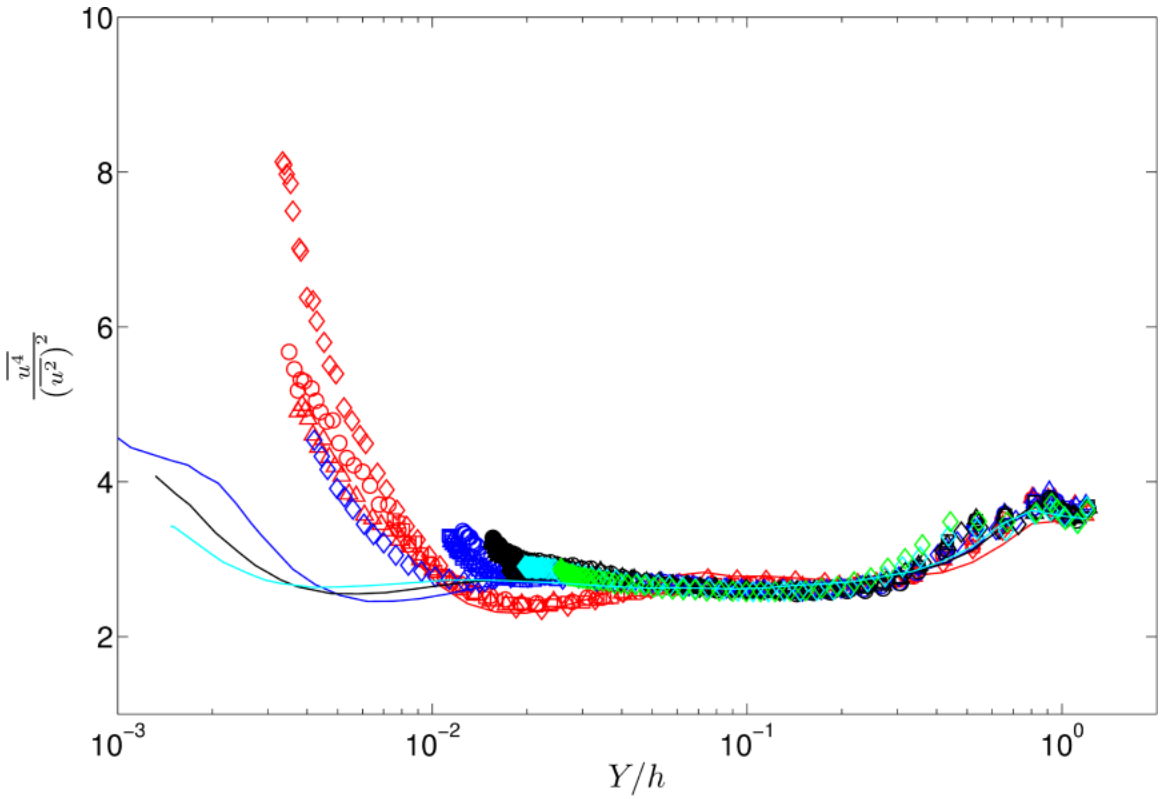

Figure 4.12: *Kurtosis or flatness factor F_u for roughness, and matched blowing cases. Symbols as in table 4.1.*

discuss the dominance of ejection events (negative u^{3+}) in smooth-wall flow outside the near-wall region of $Y^+ > 15$. This occurs because the viscous cycle is the main producer of turbulence in the flow, and directly outside the near-wall region strong ejections of fluid are observed due to transport of the turbulence away from the wall [7]. This is an effect replicated in the cases with roughness and blowing as well as the roughness only cases of figure 4.13. Negative ejections to the outer flow are also delayed as Re increases, and are shown in the figure to decrease in magnitude with increasing Reynolds number.

In addition to similar fluid ejection motions, the movement of the near-wall peak for all roughness and blowing cases seem to shift to a location $Y \approx k^+$ away from the wall, also consistent with the results of Bakken et al. (2005) [7]. Furthermore, as Re is increased, the roughness transitions to the fully rough state and the near-wall peak

is reduced, reflecting the results seen in the Reynolds stress plots which indicated a complete disruption of the viscous cycle at high Re.

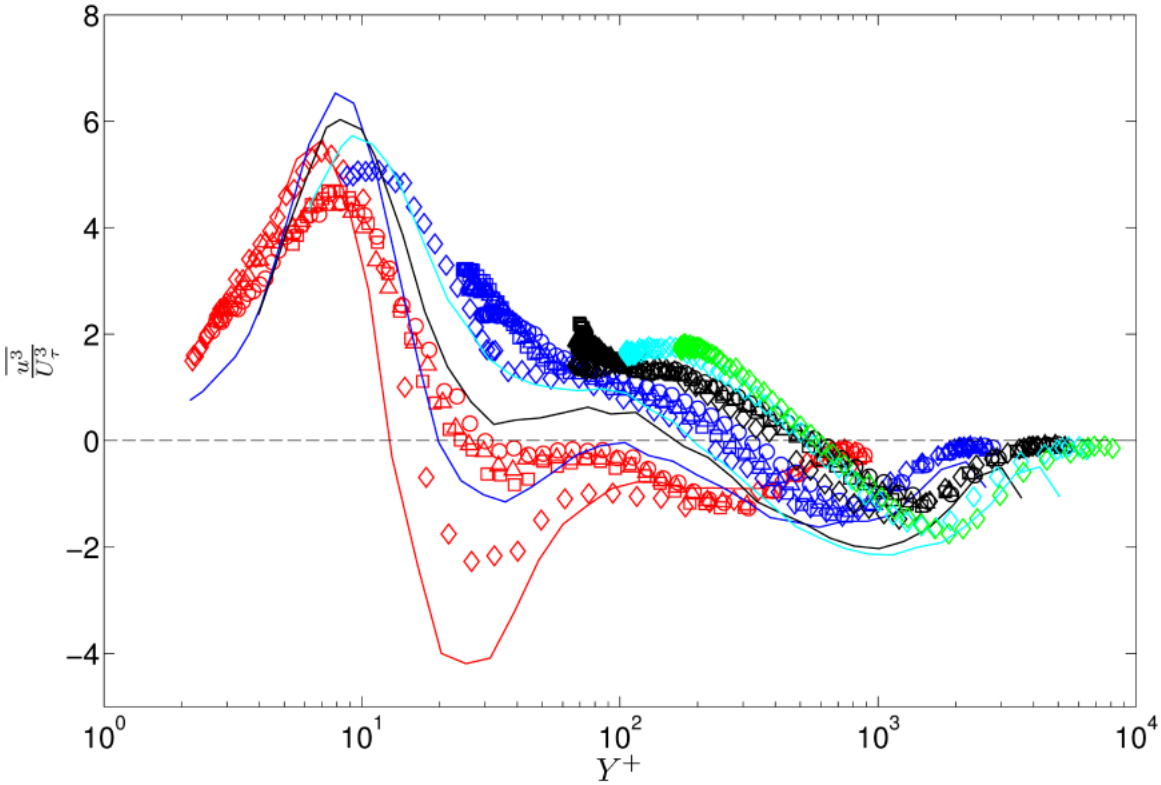

Figure 4.13: *Third-orders streamwise moments scaled with inner units. Symbols as in table 4.1.*

The outer-scaled third-order moment presented in figure 4.14 indicates that the zero-crossing point remains at a consistent wall location, independent of blowing rate for the higher Reynolds number cases ($Re_\tau > 700$). The collapse seen after $Y/h = 0.5$ regardless of Reynolds number or blowing ratio demonstrates self-similarity, but not necessarily adherence to Townsend's hypothesis. Thus the addition of blowing is not significantly affecting the third-order moment outside of $Y/h = 0.5$, but wall-similarity is not seen with the smooth-wall cases most likely due to the developing nature of the flow.

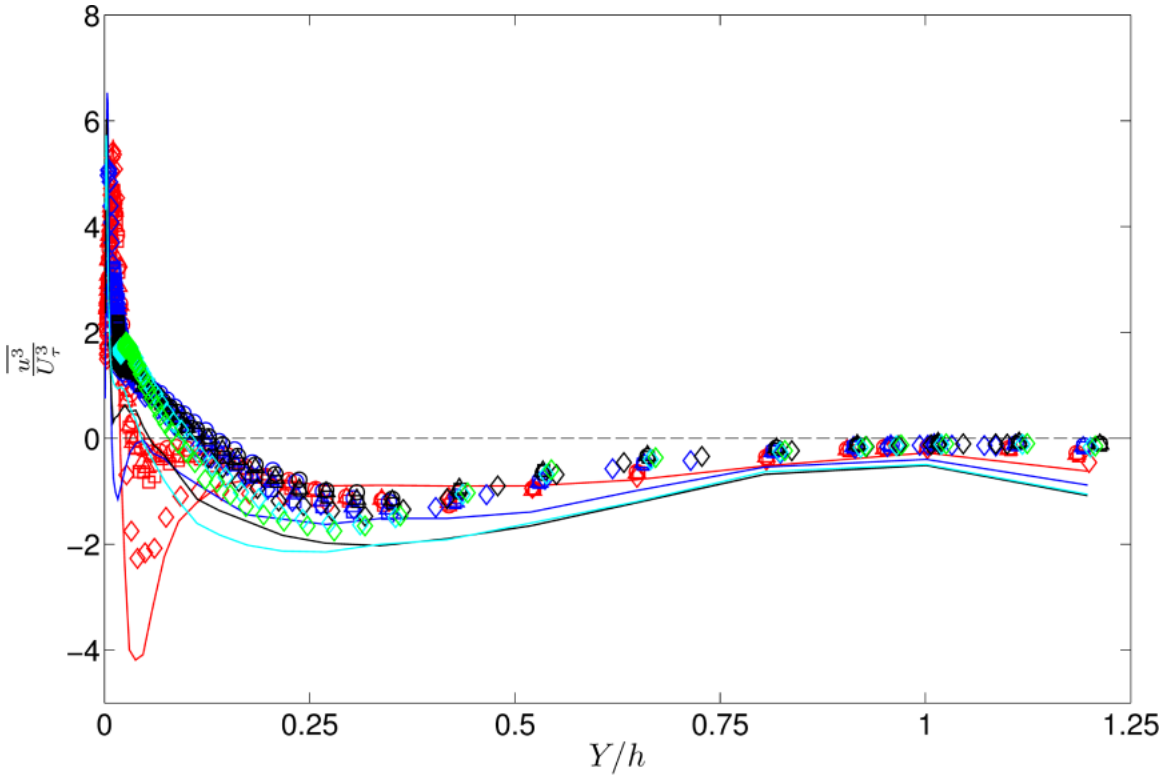

Figure 4.14: *Third-order streamwise moment, scaled in outer wall units. Symbols as in table 4.1.*

4.2 Frequency Spectra

Further investigation into the effects of roughness and blowing on the turbulence structure is performed via the power spectrum. In this section, the power-spectral density, ϕ_{uu} is calculated at each wall-normal position. To provide insight into the entire flow, Taylor's frozen flow hypothesis has been employed to examine the spectra in a pre-multiplied form as spectral maps. The method of pre-multiplication uses the streamwise wavenumber, $k_x = 2\pi f/\overline{U}$ to scale ϕ_{uu} into a form where the energy containing wavelengths in the flow are more readily apparent. The spectral maps are then generated by converting the streamwise wavenumber into a wavelength with $\lambda/h = 2\pi/(k_x h)$, and plotting $k_x\phi_{uu}$ as a contour for each wall normal position. Spectral maps generated in this manner illustrate the dependence of the pre-multiplied spectral energy on wall distance and wavelength and have the advantage of identify-

ing the wavelengths which have the greatest contribution to u^{2+} as regions of high pre-multiplied spectral value.

The spectral maps are presented in figures 4.15, 4.16, and 4.17 in a way that highlights the changes due to different boundary conditions. In subplot (a) the pre-multiplied spectrum for the smooth-wall matched Re_τ cases are displayed, and in (b) the rough wall pre-multiplied spectrum. Subplots (c) and (d) are generated by calculating the difference between rough and rough with blowing cases, $\Delta[k_x\phi_{uu}]$, for two blowing ratios $BR = 0.1, 0.16\%$, to highlight the subtle differences observed to the flow structures when $BR > 0$.

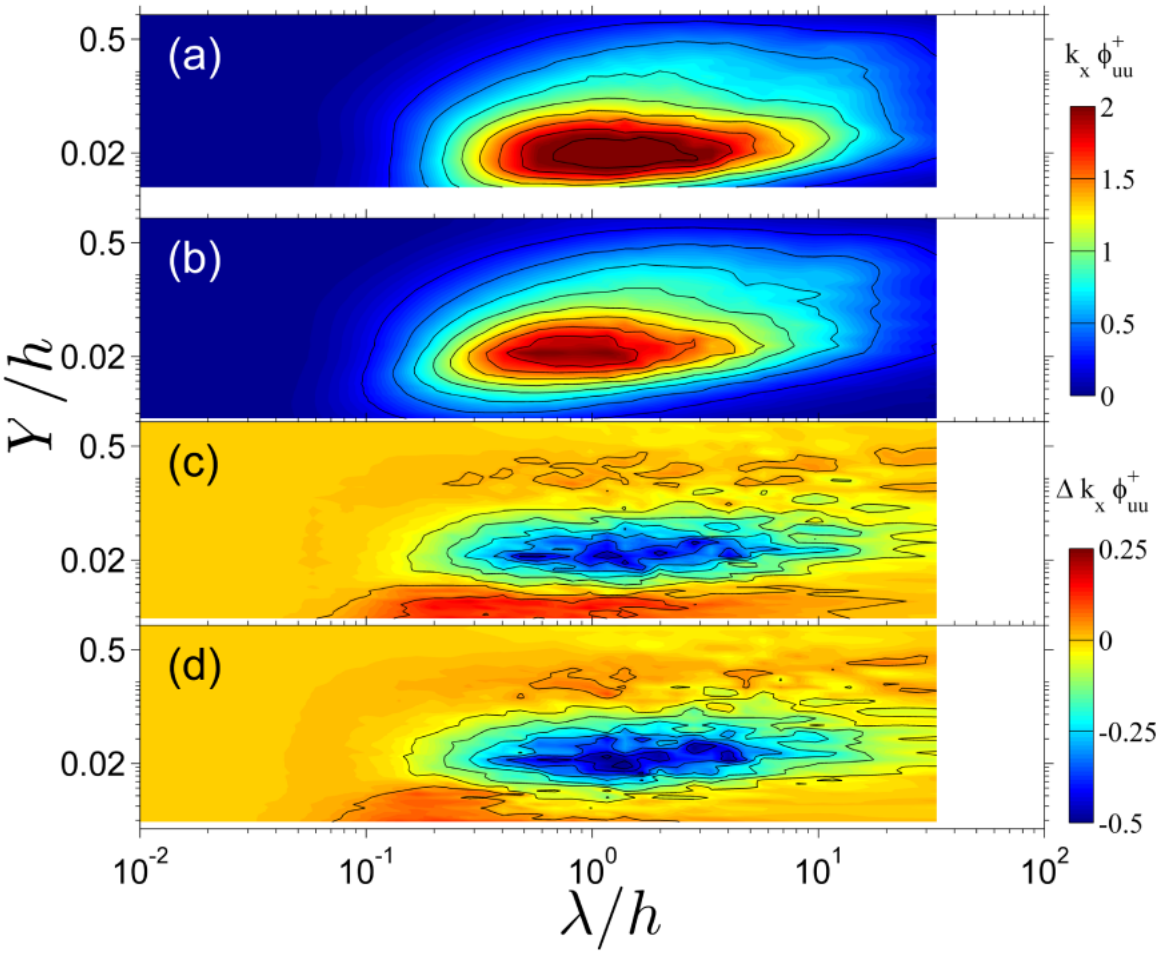

Figure 4.15: Premultiplied power spectra results for $Re_\tau \approx 700$. Spectral maps of $k_x\phi^+_{uu}$ for the (a) smooth wall (b) roughness only; and the contours of $\Delta\left(k_x\phi^+_{uu}\right)$ for (c) $BR = 0.1\% - BR = 0\%$, (d) $BR = 0.16\% - BR = 0\%$

At $Re_\tau \approx 700$ in figure 4.15, the spectral maps of both smooth and rough-wall cases are dominated by the wavelengths which form the near-wall peak in Reynolds stress, with a local maxima at $\lambda/h \approx 1$ and $Y/h = 0.025$. For this low, transitional k^+ value the effect of roughness is confined to suppression of the peak. However, at higher Reynolds numbers in figures 4.16, and 4.17 there is a much greater difference between the smooth-wall and rough-wall spectral maps. The near-wall energy site for the rough case shifts to $Y/h \approx 0.01$, which was an effect first noted in the Reynolds stress profiles of section 4.1.2. Furthermore, the wavelength of the eddies is much smaller than the near-wall energy site of the smooth-walled case, having $\lambda/h \approx 0.02$, or $\lambda \approx k$. This result is consistent with the near wall turbulence production transitioning from being driven by the wall shear, and scaling with the viscous length, to being driven by the roughness geometry and scaling with k under fully rough conditions.

Also evident in the higher Reynolds number cases are the signature of what Monty et al. (2007) termed the "dominant energy modes"[41]. These modes have recently been associated with the occurrence of large and very-large scale motions (LSMs and VLSMs) [4, 5, 8, 18, 24, 30, 69]. Although the signature of LSMs and VLSMs are also evident in the $Re_\tau \approx 700$ spectral map, due to the shift of the near-wall peak to smaller wavelengths which occurs at higher Reynolds numbers these modes are more evident in the high Reynolds number cases.

These dominant energy modes exhibit very different behavior between the smooth-wall and rough wall cases, with the long-wavelength VLSM mode dominating the smooth-walled spectral map far away from the wall and the shorter-wavelength LSM mode dominating the spectral map for the rough-walled case. The streamwise evolution of these modes from the start of the surface roughness is therefore the source of the differences between the scaled smooth-walled and rough-walled Reynolds stress profiles. Comparison of the spectral maps of the different Reynolds numbers but identical roughness boundary conditions indicates that the structure and magnitude

of the outer-layer motions maintain Reynolds number similarity

Focusing now on the effects of non-zero BR, the difference between spectral maps for two matched blowing cases of $BR = 0.1\%$, $BR = 0.16\%$ and the rough walled $BR = 0\%$ case are shown in the three figures (4.15,4.16, and 4.17) as subplots (c) and (d). These subplots were generated by interpolating data at common points on a grid made up of the wall normal position Y/h, and the wavelength λ/h for each value of $k_x\phi_{uu}$, thus allowing subtraction of the magnitude of the $BR > 0$ from the $BR = 0$ cases, and a direct comparison of the effect of blowing. For the lowest, transitionally rough, Reynolds number case in figure 4.15, the additional effects of blowing appear to be largely confined to the suppression of kinetic energy of the near-wall peak eddies, with increased suppression occurring with increasing BR. Also noticeable, however, was a slight increase in energy at wavelengths corresponding to k and in the outer layer, suggesting a shift toward increased influence of the roughness elements.

This same suppression is also evident for the two higher, fully rough, Reynolds number cases in figures 4.16 and 4.17 near the wall, with the additional blowing suppressing wavelengths of scales ranging from k to h. This suppression corresponds to the decrease in $\overline{u^2}^+$ in the near-wall peak observed in the inner-scaled Reynolds stress plots. More interesting, however, is that the decrease in $\overline{u^2}^+$ observed into the outer layer appears to be due to reduction in the strength of the LSM, suggesting that the additional blowing disrupts the formation of LSM. The magnitude of this disruption increases with increasing BR. The VLSM wavelengths, conversely, appear largely unaffected by blowing, although there is a suggestion of some enhancement of the VLSM at $Re_\tau \approx 2000$ and $BR = 0.1\%$ in figure 4.16 (c). The imperviousness of the VLSM scaling to suppression of the LSM modes indicates that the two phenomena may be unrelated, contrary to what has been proposed previously [8, 18]. Instead, it would appear that the LSM are driven by the wall boundary conditions which in the present case have been significantly altered by the addition of blowing, whereas the

VLSM are produced by the outer layer mean flow shear, which was demonstrated to scale with outer variables regardless of blowing rate.

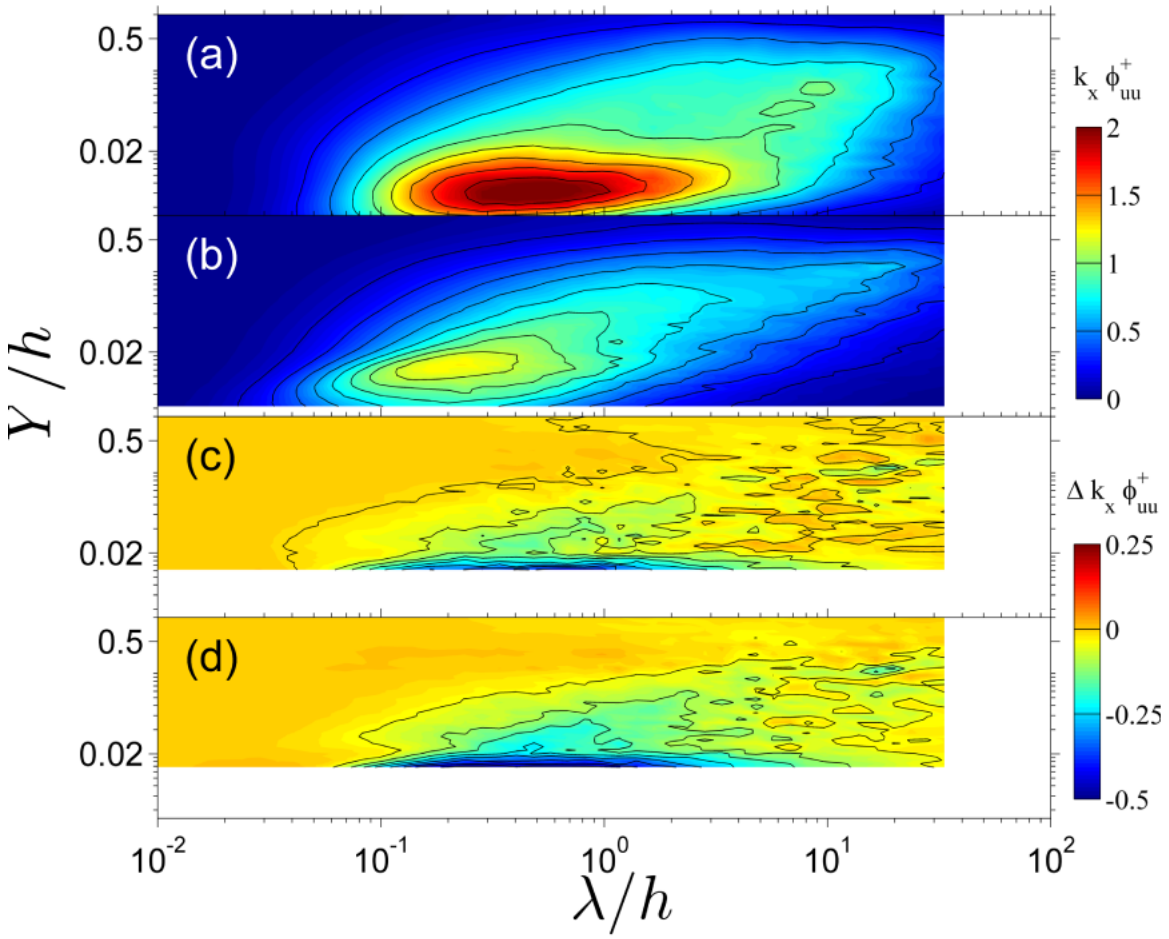

Figure 4.16: Premultiplied power spectra results for $Re_\tau \approx 2000$. Spectral maps of $k_x\phi^+_{uu}$ for the (a) smooth wall (b) roughness only; the contours of $\Delta\left(k_x\phi^+_{uu}\right)$ for (c) $BR = 0 - BR = 0.1$, (d) $BR = 0 - BR = 0.16$

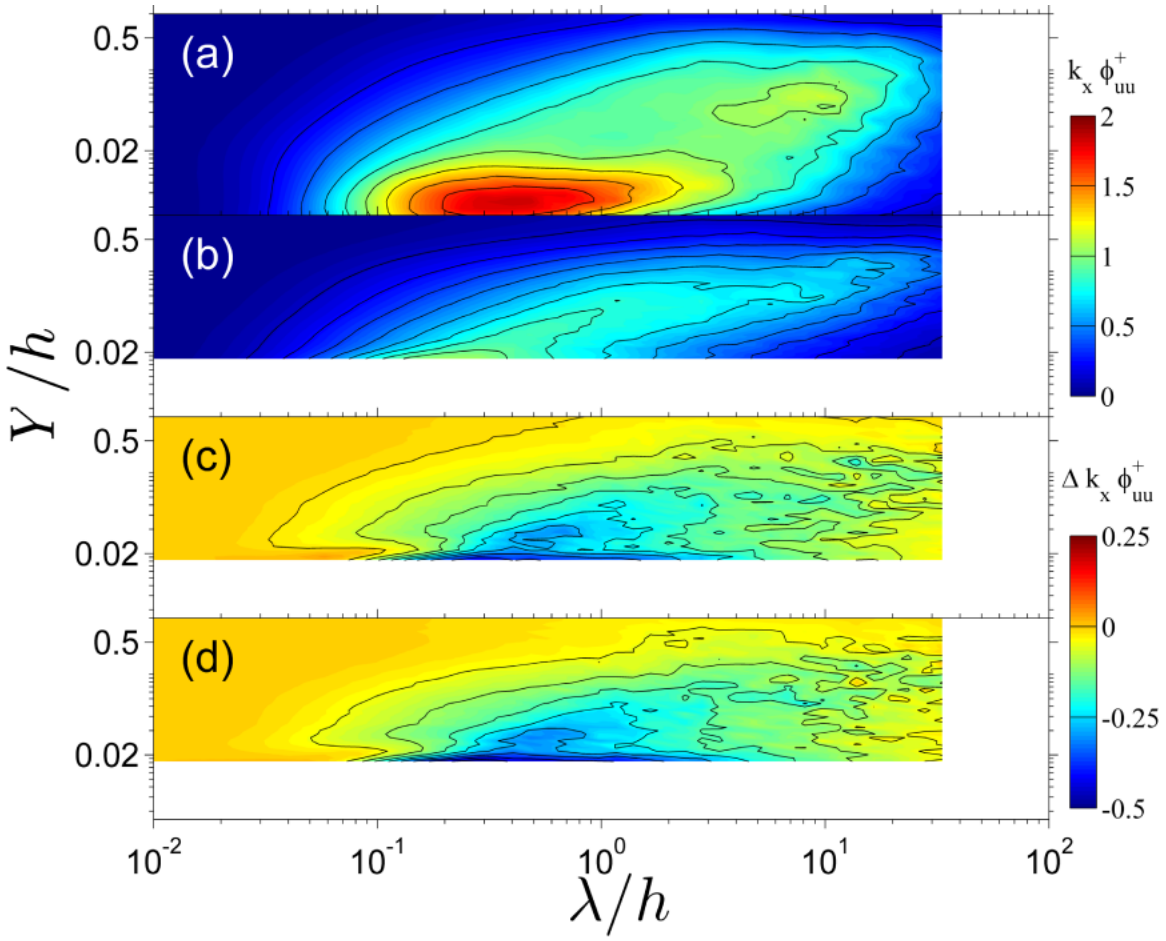

Figure 4.17: *Premultiplied power spectra for* $Re_\tau \approx 4000$. *Spectral maps of* $k_x\phi^+_{uu}$ *for the (a) smooth wall (b) roughness only; and the contours* $\Delta\left(k_x\phi^+_{uu}\right)$ *for (c)* $BR = 0 - BR = 0.1$, *(d)* $BR = 0 - BR = 0.16$

4.3 Blowing Ratio Limitations on Self-Similarity

To investigate the validity of self-similarity for higher blowing ratios than the matched BR cases, several additional experiments were carried out. Upon finishing the matched BR cases, it was postulated that some amount of blowing would cause the flow to drastically move away from self-similarity.

In figure 4.18, the defect velocity profiles are plotted with the additional test cases in which the blowing ratio was increased to $BR = 0.18, 0.45, 0.56, 0.73\%$ for the $Re_\tau \approx 700$ cases and $BR = 0.145, 0.24, 0.35\%$ for the $Re_\tau \approx 2000$ cases. This plot shows that at the lowest Re, self-similarity holds until $BR > 0.18\%$. This trend is

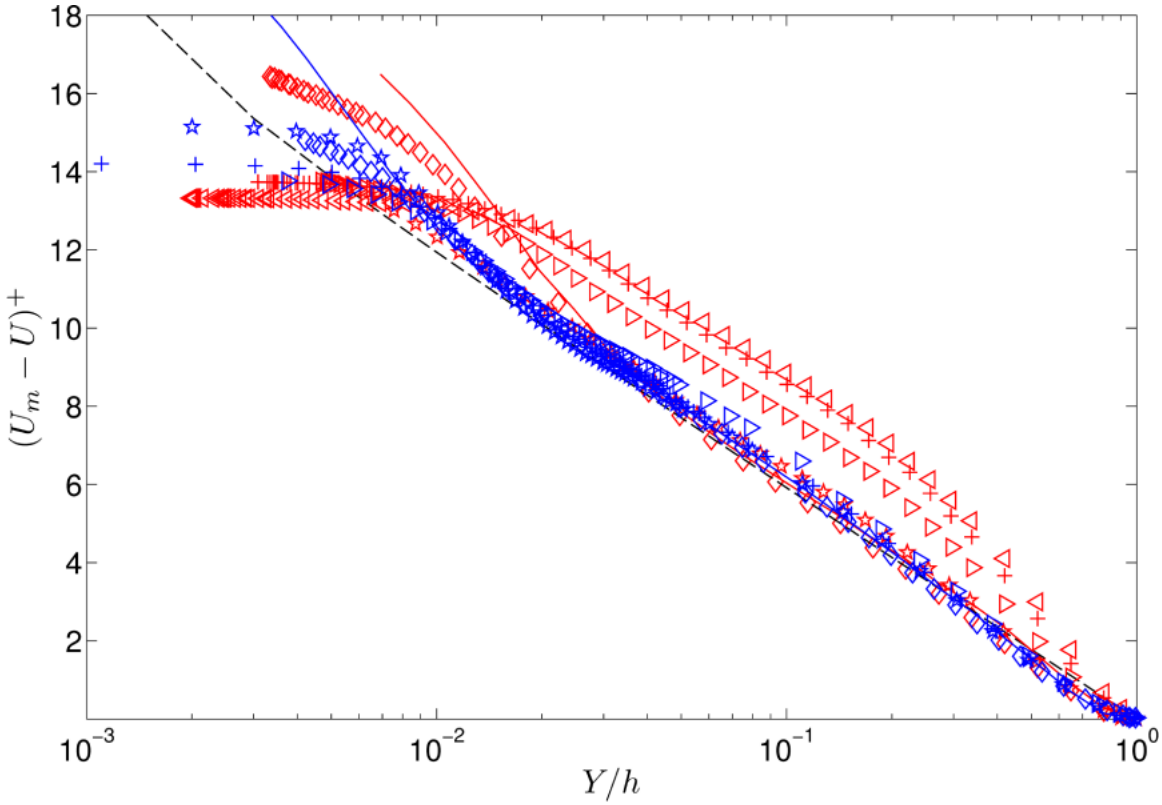

Figure 4.18: *Mean velocity defect plot for* $Re_\tau \approx 700$ *and* 2000. *Symbols indicate blowing rate, see table 4.1.*

not seen in the higher Re cases where self-similarity holds. Apparently, the ability of the flow to remain self-similar in the outer layer is Reynolds number dependent as well as BR dependent.

The same effect is seen in the Reynolds stress plots of figure 4.19. The increased blowing rate has completely disrupted the near-wall viscous cycle for the low Re case. Perhaps more interestingly, the resulting profile does not resemble the fully rough flow with blowing at higher Re, where the peak location was seen to scale with k. Instead, there is no identifiable near-wall peak for the high BR, $Re_\tau \approx 700$ cases.

To gain further insight into this phenomena, the same presentation employed in Section 4.2 will be used to examine the flow structure modifications as blowing becomes large. The difference in power spectral maps between the cases with $BR > 0$ and the $BR = 0$ case are plotted for $Re_\tau \approx 700$ in figure 4.20.

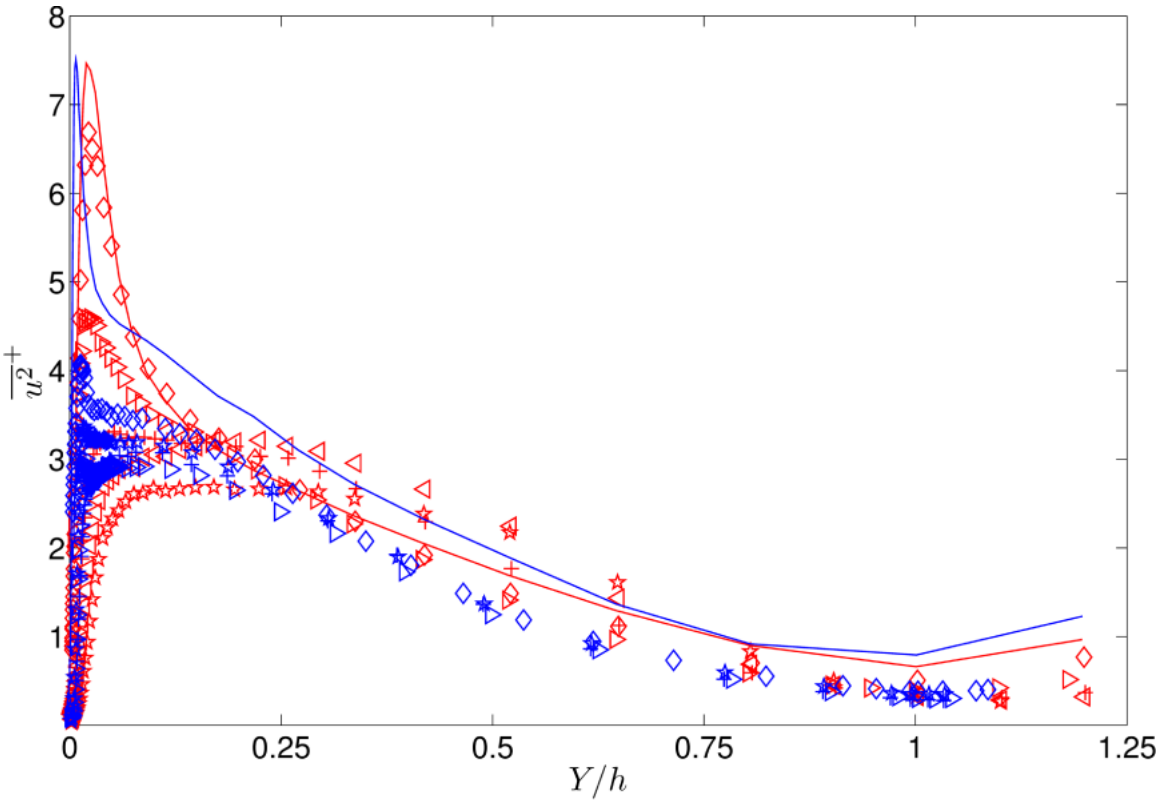

Figure 4.19: *Outer-scaled Reynolds stress for* $Re_\tau \approx 700$ *and* 2000. *Symbols indicate blowing rate, see table 4.1.*

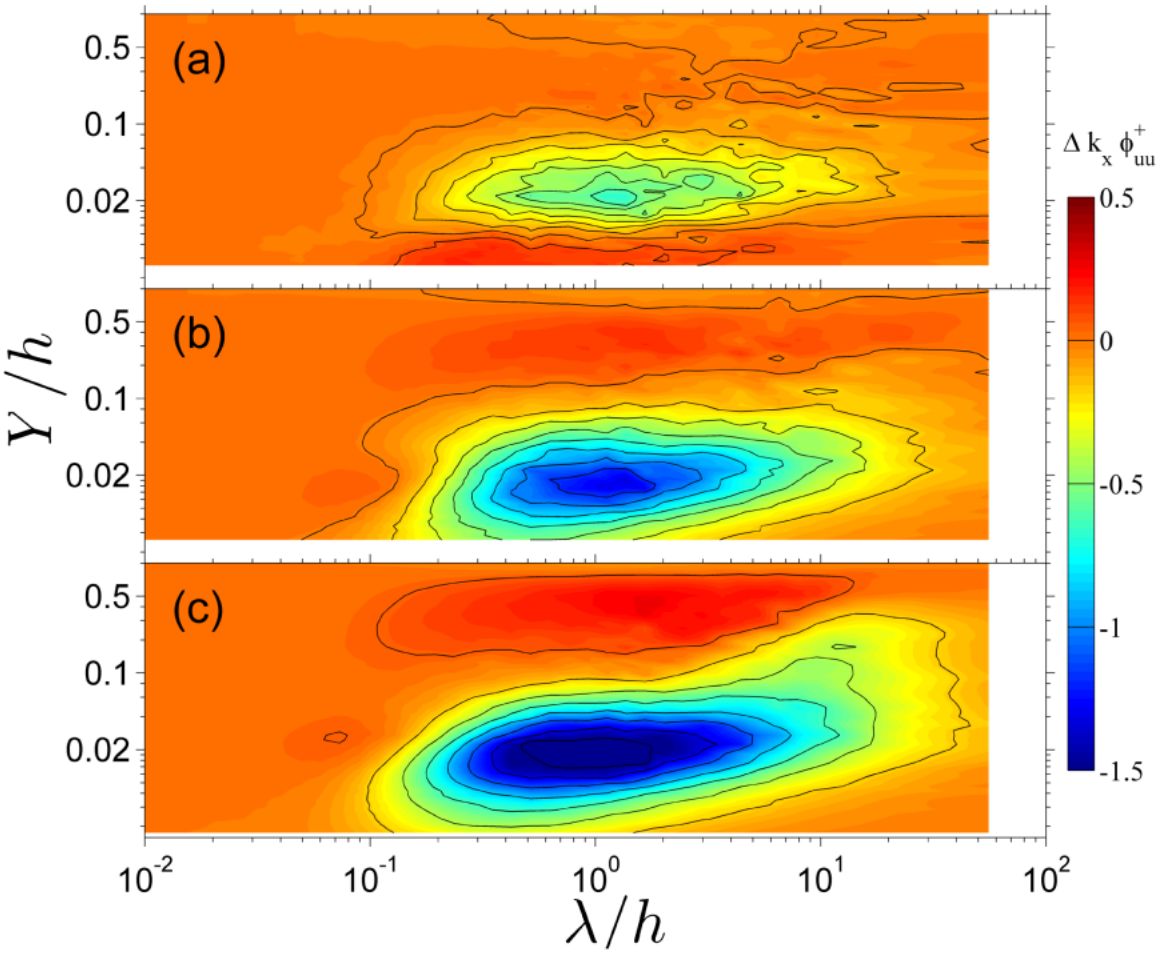

Figure 4.20: *Difference in premultiplied power spectral maps for* $Re_\tau \approx 700$ *at high blowing rates. Spectral map contours,* $k_x\phi^+_{uu}$*, are plotted at (a)* $BR = 0.18 - 0\%$*; (b)* $BR = 0.45 - 0\%$*; and (c)* $BR = 0.73 - 0\%$*.*

The lowest Reynolds number case with high blowing displays similar results to that of the Reynolds stress plots. At $BR = 0.18\%$, a decrease of the near-wall energy site is seen, but no change is observed in the outer flow. This is not the case for the next two higher blowing ratios where the energy of the near-wall is further depleted, but an energy gain is observed far into the outer flow structure. Specifically, wavelengths near the LSM signature appear to be gaining energy, and the VLSM signature is preserved. This provides further evidence to the conclusion made in section 4.2 that the VLSM and LSM motions are not be interdependent.

Lastly, the $Re_\tau \approx 2000$ cases are shown as plots of the difference in premultiplied

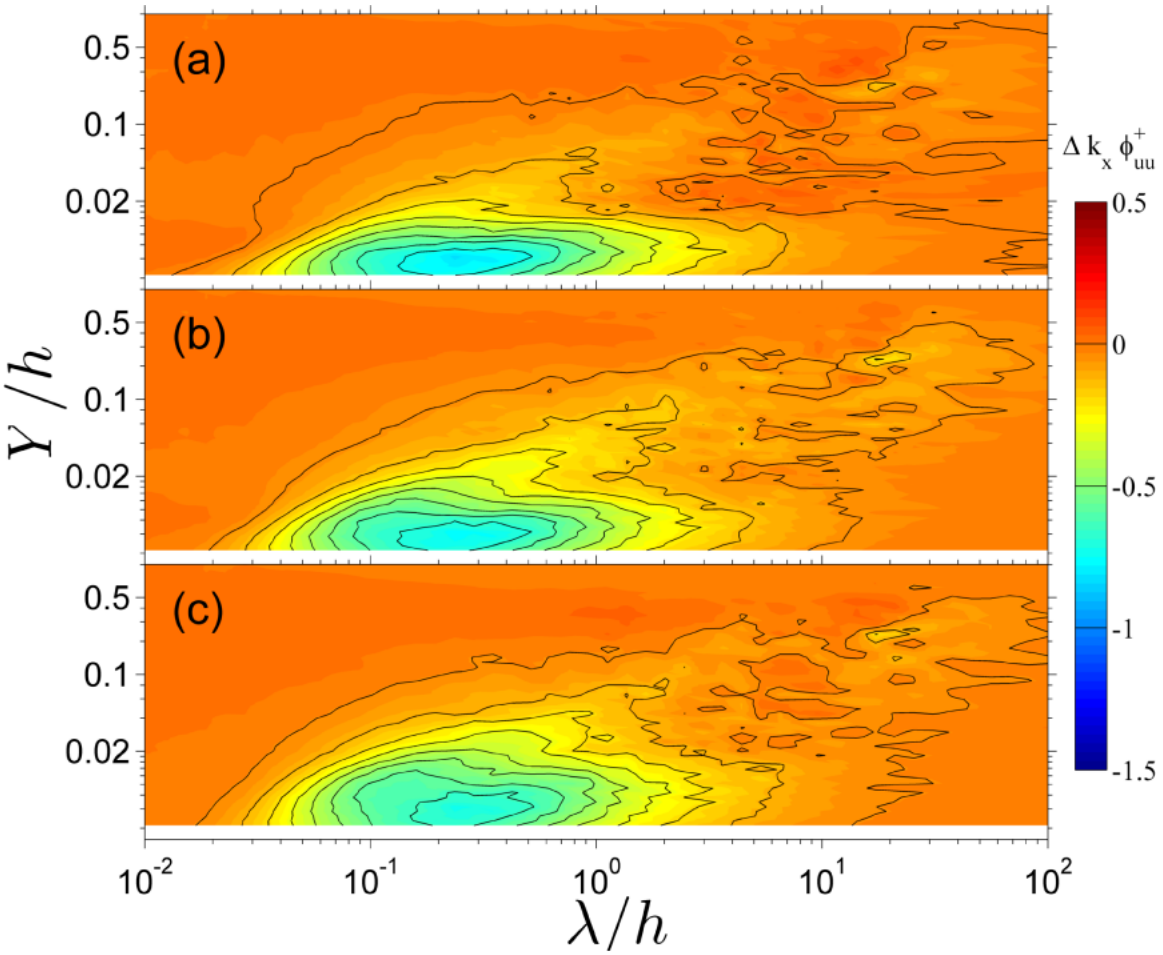

Figure 4.21: *Difference in premultiplied power spectral maps for* $Re_\tau \approx 2000$ *at high blowing rates. Spectral map contours,* $\Delta k_x \phi^+_{uu}$*, are plotted at (a)* $BR = 0.145 - 0\%$*; (b)* $BR = 0.24 - 0\%$*; and (c)* $BR = 0.35 - 0\%$*.*

power spectral maps in figure 4.21. Unlike the low speed cases, it is seen that the trends of the maps in Section 4.2 are retained, and no modification to the outer flow is observed. Furthermore, because this flow is nearly fully rough there is only slight variation in the wall-normal location of the near-wall energy site.

This section has highlighted that the ability of the flow to maintain self-similarity is dependent on the blowing ratio and the Reynolds number of the flow. Although additional testing would be required to solidify this fact, at the closest matched blowing ratio ($BR = 0.45\%$ for $Re_\tau \approx 700$ and $BR = 0.35\%$ for $Re_\tau \approx 2000$), there are significant variations in the patterns observed in the spectral difference maps.

Thus, the motions in the outer layer can be affected if enough momentum is added to the flow, specifically the LSM appear to be most responsive.

4.4 Streamwise Flow Development

To investigate the streamwise development of the flow, three sets of measurements were carried out at different streamwise locations. In this section the flow injection rates, rather than BR, are matched across Reynolds numbers. This is because of difficulties with matching BR at the test section exit where U_m varied significantly with small increases in $\dot{V}_{inj}$. The symbols used in this section are listed in table 4.2. The first set of experiments examined roughness only at the center of the test section and at the exit of the test section (x = 57 and 103.1 cm, respectively). This was preformed as a preliminary test to the addition of blowing to the flow. The mean profiles scaled with outer variables are shown in figure 4.22.

Table 4.2: Symbols for streamwise flow development plots according to Reynolds number at $x = 57$ cm.

Case	Tunnel Freq. (Hz)	Re_τ	$\dot{V}_{inj}$ (m^3/min)	Symbol
22	38	3,698	0	◇
23	38	4,034	1.133	□
24	38	4,371	1.416	△
25	38	4,707	1.841	○
26	10	672.4	0	◇
27	10	806.9	1.133	▷
28	10	874.1	1.416	+
29	10	924.6	1.841	◁
30	38	4,135	0	◇
31	38	4,673	1.133	□
32	38	4,956	1.416	△
33	38	5,043	1.841	○
34	63	7,396	0	◇

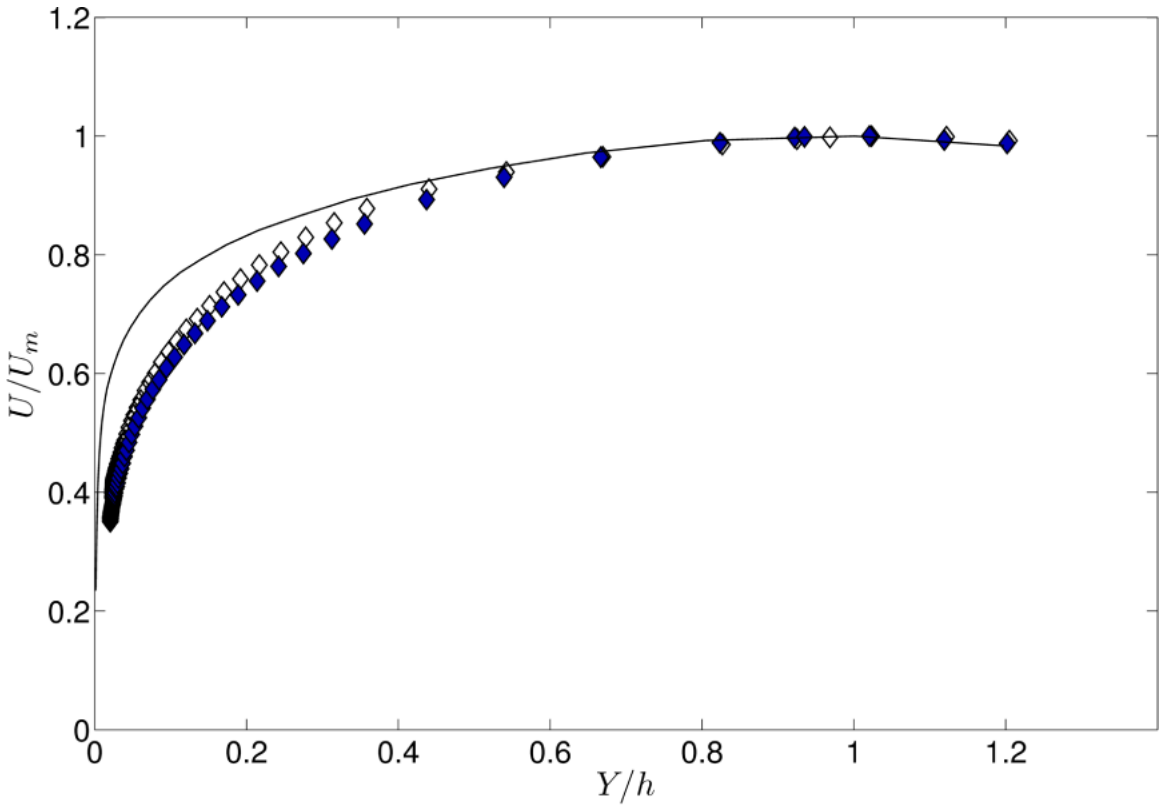

Figure 4.22: *Outer- scaled velocity for two streamwise locations at* $Re_\tau \approx 7000$. *The symbol fill indicates streamwise location, white symbols are at* $x = 54$ *cm, and blue symbols are at* $x = 103.1$ *cm. Symbol shape as in table 4.1.*

As was suspected, the flow is developing along the test section. This was anticipated at high Reynolds numbers as the relatively small boundary layer must be allowed to grow and finally merge at some distance x from the entrance. Thus, two more sets of experiments were completed to analyze the roughness development length and the effects of blowing on this length. The first set of data comes from the run cases at $Re_\tau \approx 4000$, with velocity profiles taken at the inlet, center, and exit of the test section. At this Reynolds number, a roughness only case and 3 matched blowing ratios were investigated.

In figure 4.23, the outer-scaled mean velocity is plotted for the three streamwise locations, which is denoted by the symbol fill color. Focusing on the $BR = 0$ cases, the flow is trending towards a fully-developed state, but is still developing at the test section outlet. The same trend is observed in the data for the $BR > 0$ cases,

all the way up to the maximum blowing rate. This observation must be taken with caution, however, as the addition of blowing along the length of the test section without any balancing of the mass addition means the cases with roughness and blowing are not going to reach a fully developed state. A preliminary observation is that the flow appears to be adjusting to the blowing and roughness rapidly in the streamwise direction, with little difference seen between the center and exit locations. Furthermore, the blowing rate has little effect on the distance the flow requires to develop.

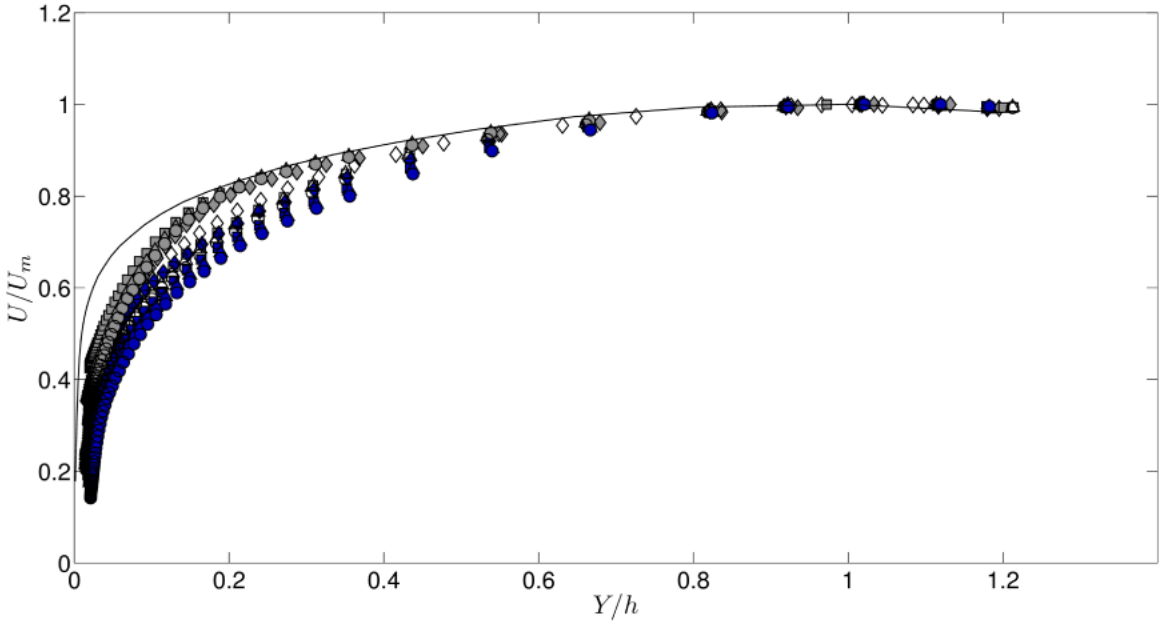

Figure 4.23: *Outer-scaled velocity for three streamwise locations at* $Re_\tau \approx 4000$*, for 3 different blowing rates. The symbol fill indicates streamwise location, gray symbols are at* $x = 16.7$ *cm, no-fill symbols are at* $x = 54$ *cm, and blue symbols are at* $x = 103.1$ *cm. Symbols as in table 4.1.*

The last set of experiments which investigated roughness and blowing effects on flow development in the test section only acquired data at the test section center and the exit. This is because after acquiring the data set presented in figure 4.23, it was noticed that the flow at the inlet was very disturbed and did not have adequate time to adjust to the new boundary conditions. This is also why no attempt has been made to provide a friction velocity (and hence inner-scaled plots) for the inlet cases.

The cases presented in figure 4.26, were acquired at a nominal $Re_\tau \approx 700$, with an attempt made to match the blowing ratios. Unfortunately, this was unsuccessful for measurements taken at the test section exit. At this location, the blowing had added a significant amount of mass to the flow relative to the mass flow provided by the channel itself. This made predicting U_m *a priori* very difficult. Therefore, the results presented in figure 4.24, matched the flow injection rate, $\dot{V}_{injected}$ instead.

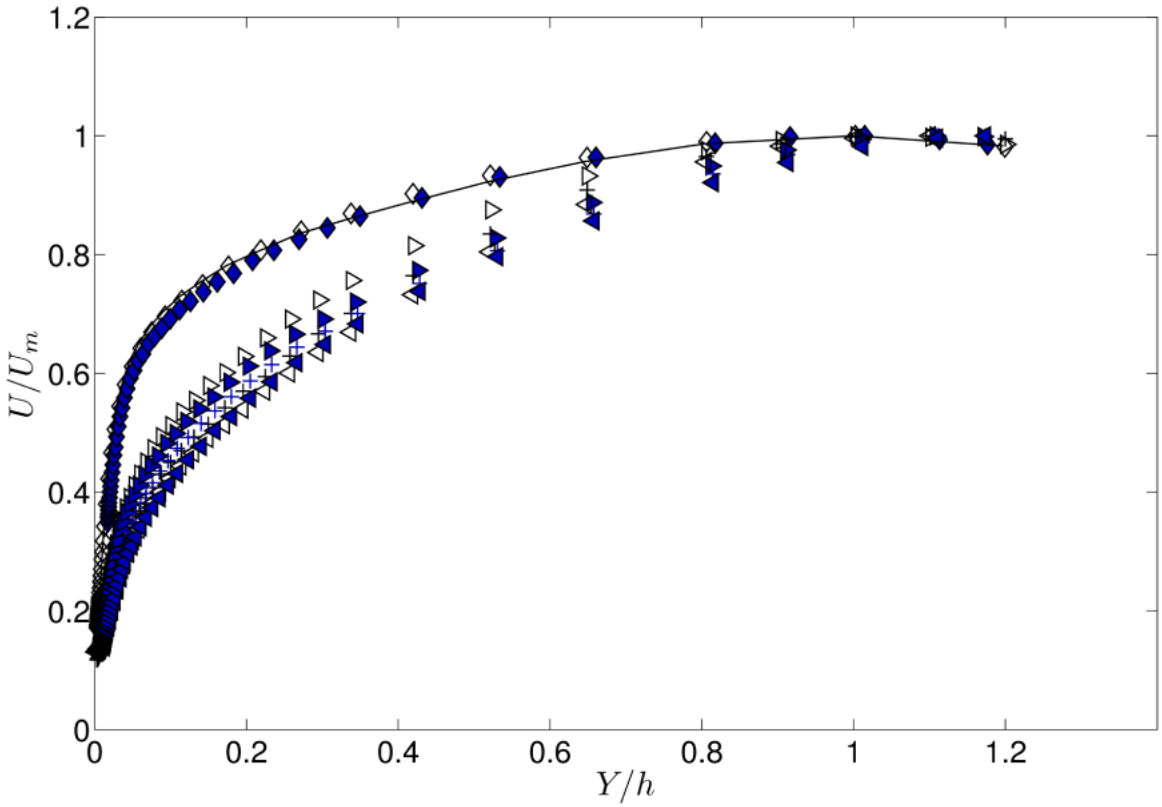

Figure 4.24: *Outer-scaled velocity for two streamwise locations at $Re_\tau \approx 700$, for 3 different flow injection rates. The symbol fill indicates streamwise location, no-fill symbols are at $x = 54$ cm, and blue filled symbols are at $x = 103.1$ cm. For symbol shapes see table 4.1.*

For the cases in figure 4.24, the flow appears to adapt well in the streamwise direction regardless of the blowing ratio selected. Indeed the blowing biases the flow away from the wall (as does the roughness) and increases U_m, but the flow appears to develop very quickly despite the blowing rate specified. This may be due to the low flow speed which allows any effects of the blowing to propagate quickly in the

y direction. To investigate this theory, an attempt has been made to determine the friction velocity for this set of cases.

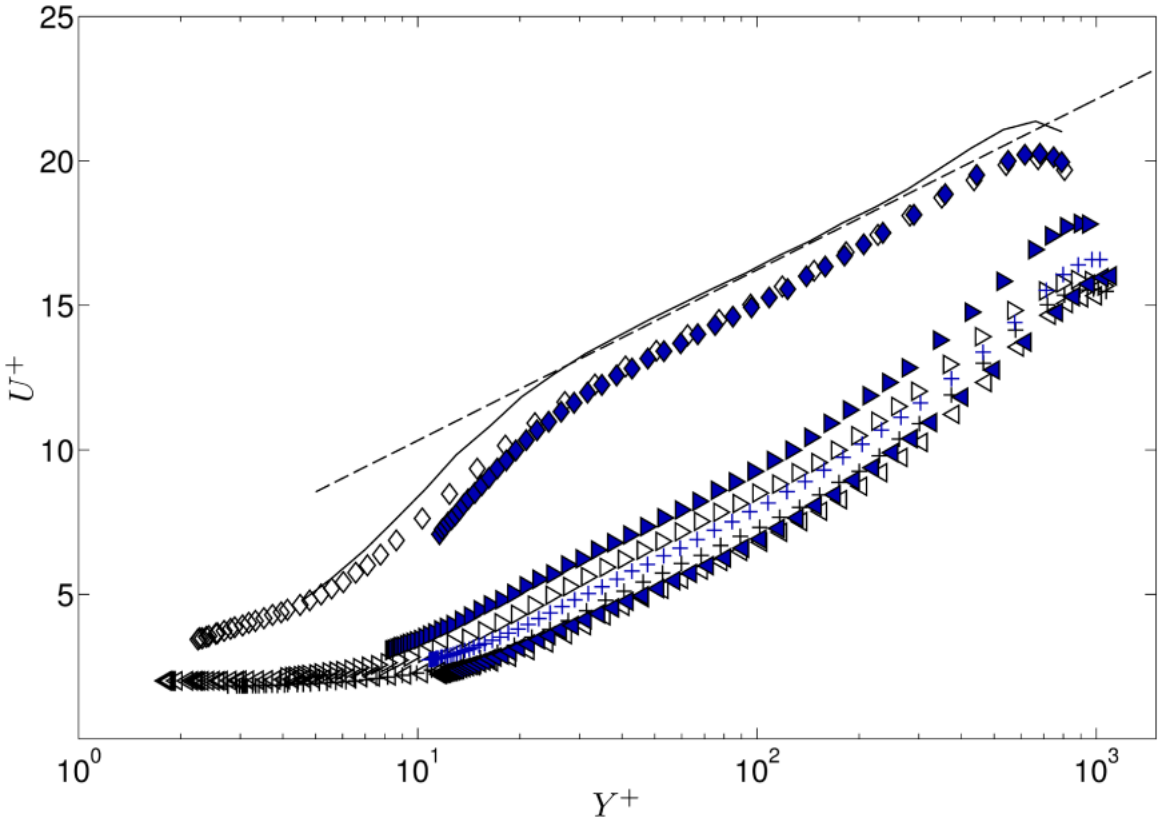

Figure 4.25: *Inner-scaled mean velocity for* $Re_\tau \approx 700$ *demonstrating friction velocity fit. Symbol shape as in table 4.1.*

As shown in figures 4.25 and 4.26, using the friction velocity as the normalizing parameter shows similar results as using only the outer scales. At low Reynolds numbers, the flow adapts to the change in boundary conditions rapidly as only slight differences are seen between measurements taken at 57 cm and $x = 103.1$ cm from the inlet.

Thus the mean profiles indicate roughness effects on the flow are adapted to swiftly at higher Reynolds numbers. This can be related to the increasing coefficient of friction as the Reynolds number is increased. The flow quickly becomes fully rough and thus independent of surface conditions. Thus the blowing ratio determines the shape of the profile, but the streamwise distance the flow requires to adapt to a change

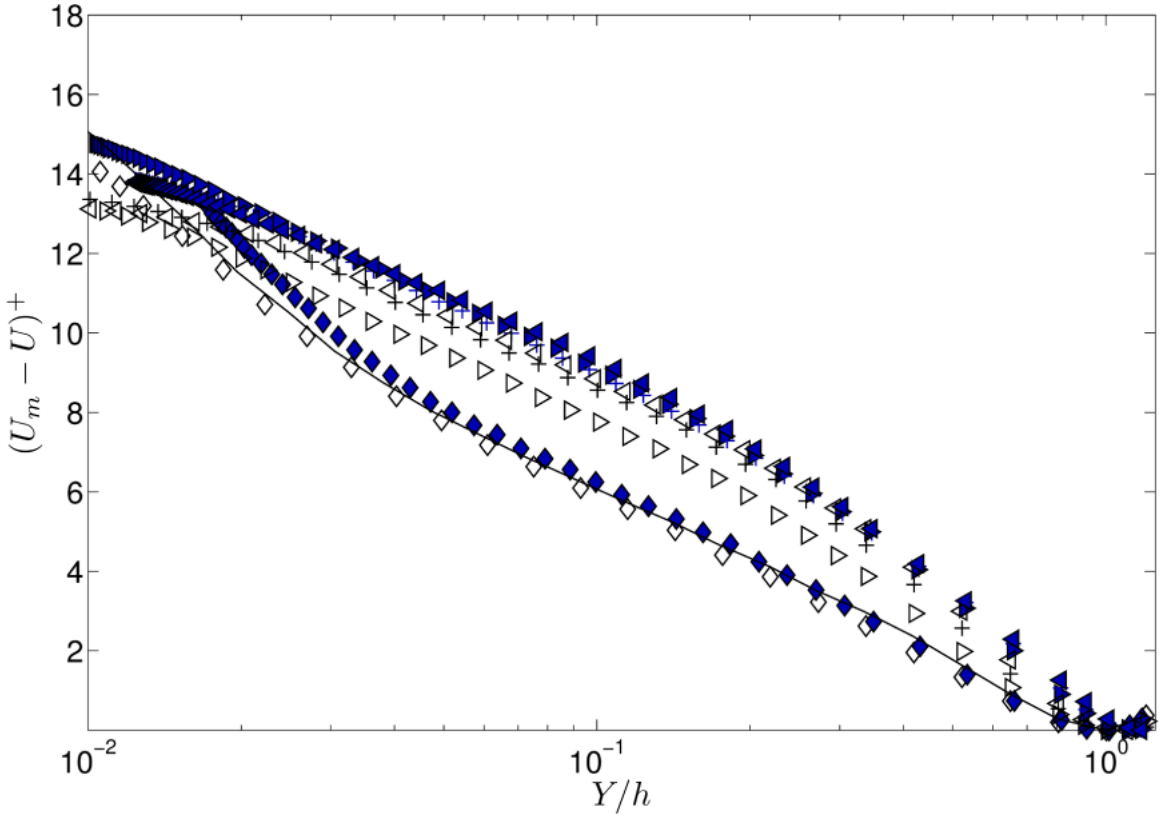

Figure 4.26: *Velocity defect plot for $Re_\tau \approx 700$ cases showing the two streamwise locations of measurement. Symbol shape as in table 4.1.*

in blowing does not depend on BR.

The Reynolds stress plots and higher-order statistics show agreement with the mean flow in that the inlet of the test section highly-disturbs the flow but the development length necessary to ensure a statistically stable flow may be relatively short. In figure 4.27, the outer-scaled Reynolds stress is plotted for two different streamwise locations. As was noted for the mean flow at this Reynolds number, the flow appears to be developing and the resulting fluctuating velocities have not converged. The only cases displaying collapse are the $BR = 0$ runs which are close to matching the smooth-wall case indicating Townsend's hypothesis may indeed be valid if the flow was allowed to continue developing.

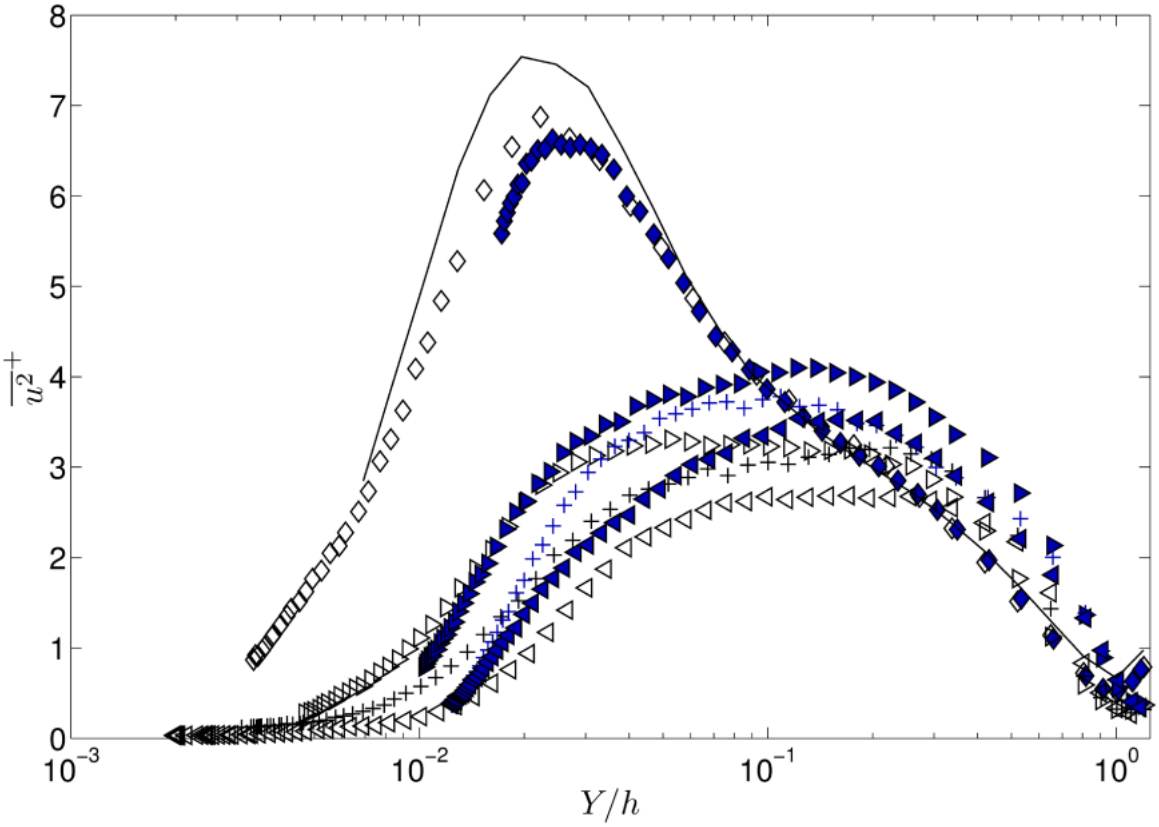

Figure 4.27: *Outer-scaled Reynolds stress for two streamwise locations at* $Re_\tau \approx 700$*, for 3 different flow injection rates. The symbol fill indicates streamwise location, no-fill symbols are at* $x = 54$ *cm, and blue filled symbols are at* $x = 103.1$ *cm. For symbol shapes see table 4.1.*

At higher Reynolds numbers, as in figures 4.28, and 4.29, self-consistency is seen

between the $BR = 0$ and $BR > 0$ cases at the exit to the test section. This result is unexpected as collapse of the rough-wall case with the smooth-wall was predicted for developed flow, in support of Townsend's hypothesis. While this result does not show explicit evidence against Townsend's hypothesis, it does indicate that further work will be necessary to establish whether wall-similarity holds in this case.

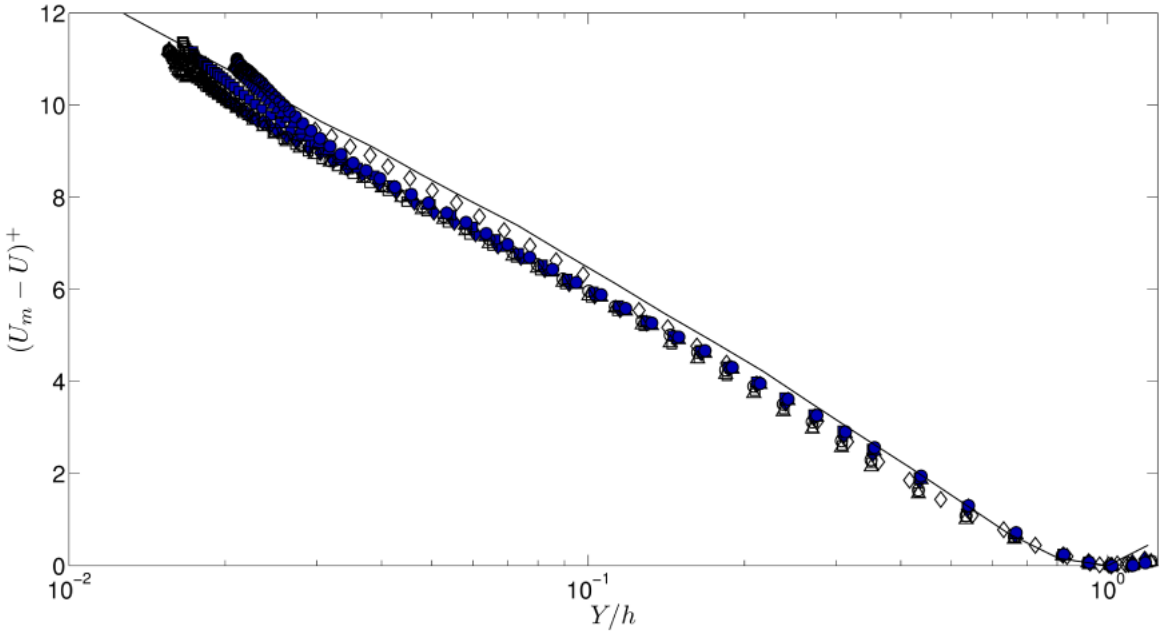

Figure 4.28: *Inner-scaled mean velocity for two streamwise locations at* $Re_\tau \approx 4000$*, for 3 different flow injection rates. The symbol fill indicates streamwise location, no-fill symbols are at* $x = 54$ *cm, and blue filled symbols are at* $x = 103.1$ *cm. For symbol shapes see table 4.1.*

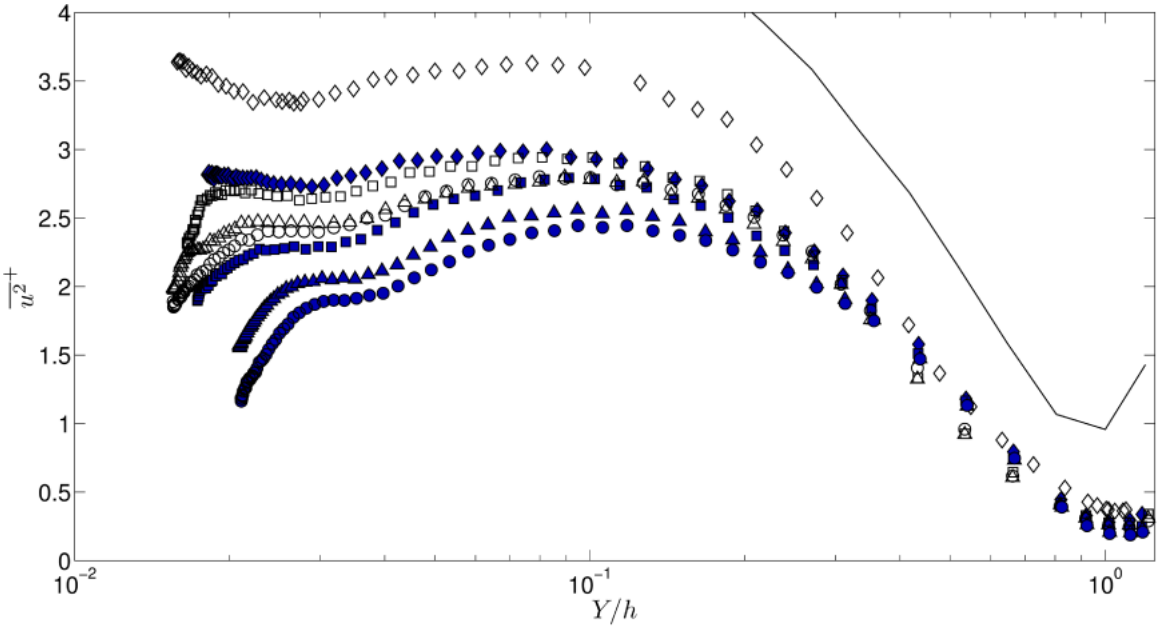

Figure 4.29: *Outer-scaled Reynolds stress for two streamwise locations at* $Re_\tau \approx 4000$ *and 3 different flow injection rates. The symbol fill indicates streamwise location, no-fill symbols are at* $x = 54$ *cm, and blue filled symbols are at* $x = 103.1$ *cm. For symbol shapes see table 4.1.*

Chapter 5

Conclusions

A turbulent channel flow wind tunnel modified using a blowing rig and roughness was employed to provide the highest roughness Reynolds number study to date for channel-type flows. With reference to computational studies in this field, smooth-wall channel flow DNS for up to $Re_\tau = 2000$ have only recently been completed [22]. However, it will be a significant amount of time before the roughness studies presented here can be accurately simulated by DNS, and it is thus important to continue experimental work of this nature. In addition to the high Reynolds number roughness data provided, this study has the added complexity of uniform flow injection over the surface, which is another effect that is difficult to simulate in computer models.

The unique data set provided here resolved the velocity profile into the roughness elements themselves, capturing the time-averaged statistics across the channel. Furthermore, this is the first time high-fidelity turbulence statistics have been available for roughness and flow injection, with the added benefit of insight into the turbulent flow structures through the use of power spectral maps. Additionally, new insight has been gained into the applicability of Townsend's hypothesis of wall similarity. It was found that the turbulence statistics may not follow wall-similarity even when the mean velocity collapses. Finally, modifications to the power spectra due to roughness and blowing were isolated and it was suggested that the LSM's are being modulated by the change in wall boundary conditions. With this compiled database, several conclusions can be drawn with regard to the flow modifications:

i The coefficient of friction calculated for the $BR = 0$ cases indicated that the highest Reynolds number cases reached the fully rough condition and were thus independent of the roughness geometry. For cases with $BR > 0$, a simple correc-

tional scheme was devised to account for the positive shift in ΔU^+ due to blowing. This scheme was further extended to C_f, where it can be used to account for the friction increase due to blowing.

ii The velocity defect plot at matched blowing ratios revealed that roughness and blowing effects in the mean flow are confined to the near-wall and are only active in setting the wall shear stress and zero plane displacement for the outer flow.

iii For transitional roughness Reynolds numbers, $k^+ < 40$, blowing decreases the near-wall peak in the Reynolds stress plots but the turbulence production cycle remains the primary producer of shear in the flow.

iv When $k^+ \geq 40$, the Reynolds stress plot peak scales on the roughness element height ($Y \approx 0.5k$ with roughness only and $Y \approx k$ with blowing) as opposed to following the smooth wall behavior where $Y^+ \approx 15$.

v For the roughness only cases, self-similarity was seen in the mean velocity plots and Reynolds stresses. However, because the flow was still developing over the roughness, the profiles did not collapse with the smooth-wall, fully-developed cases. Due to this behavior, it was estimated that the rough-wall cases support wall similarity after a sufficient development length.

vi The skewness and flatness factors were seen to collapse at $k^+ \geq 40$ regardless of blowing ratio implemented, and the zero-crossing point of the third-order moment scaled in outer units was seen to be consistent for this same condition.

vii The power spectral maps revealed that as k^+ increased, more energy was added to the flow at wavelengths which corresponded to the roughness height. Furthermore, disruption of the LSM was seen as $BR > 0$ while the VLSM remained impervious to any changes in the LSM. This indicated that the two phenomena may be

unrelated and that LSM may be driven by the wall boundary condition while VLSM are produced in the outer layer by mean flow shear.

viii The ability of the flow to maintain self-similarity was found to be BR and Re dependent with a departure from self-similarity accompanied by a large increase in the energy of the LSM. This is ancillary to the previous conclusion in which a decrease in the energy of the LSM is seen as BR is increased (but within the limits of self-similarity studied here).

ix The flow was also shown to be developing along the test section. Surprisingly the flow behavior at high Reynolds number and $BR = 0$ approaches the $BR > 0$ cases at the test section exit and showed self-similarity in both the velocity defect and Reynolds stress plots. This indicated that the flow may approach wall similarity if allowed to reach full development and that the blowing is indeed acting as additional roughness because as k^+ increases for the $BR = 0$ case it collapses with the higher k^+, $BR > 0$ behavior.

With these conclusions in hand, further studies can investigate the work completed here to study such effects as the self-similarity of the flow versus its wall similarity. Additional roughness development length will be necessary in future work as well as extension of the data set to additional roughness elements, especially those most relevant to the engineering roughness which is likely to be encountered. Currently, work is undergoing to introduce test surfaces which are geometrically similar to an ablated heat shield and sand-grain type roughnesses. With the foundation of work in the study presented here, a clear direction forward can be taken and further insight into the complicated flow field of roughness and blowing can be investigated more fully.

Appendices

5.1 Appendix A: Blowing Rig Smoke Flow Visualization

To acquire a preliminary idea about the performance of the blowing rig, and a heuristic insight into the flow-field modifications due to blowing, a series of simple smoke-flow visualizations were performed with blowing rig V.2. These visualizations were all performed at the maximum injection rate possible of approximately 1.841 m^3/min (65 CFM). The smoke was first introduced into the blowing rig with the channel and flow injection blower off. Then the channel was briefly cycled to remove any excess smoke from the channel test section which had escaped from the blowing rig. Following this the channel speed was set, and the blowing rig powered on. At the higher tunnel speeds, the large amount of turbulent mixing made tracking the evolution of flow structures with the smoke difficult. However, a quantitative idea about the dispersion of the injected gas into the tunnel was made relatively easily at two tunnel speeds, 10 and 20 Hz or 4.3 and 9.2 m/s respectively with the constant $\dot{V}_{inj}$ listed above. The images are shown in figures 5.1 and 5.2, and were acquired at the channel exit, with the flow conditioning section removed for optical access. This preliminary set of data showed that the effects of blowing could traverse a significant portion of the outer-flow, and the large amount of mixing caused the smoke to be carried far into the outer layer near the channel exit.

To gain an idea of the flow development in the streamwise direction, a set of low-speed experiments were performed at a tunnel speed of 2.5 Hz or 0.05 m/s. This low speed allowed some of the larger flow structures to be captured by the smoke flow visualization. A time evolution of the flow is shown in figure 5.3.

Also noted in figure 5.3 is the evolution of a turbulent "bulge" in the flow. It increases in size as it is convected downstream after initially forming at the wall.

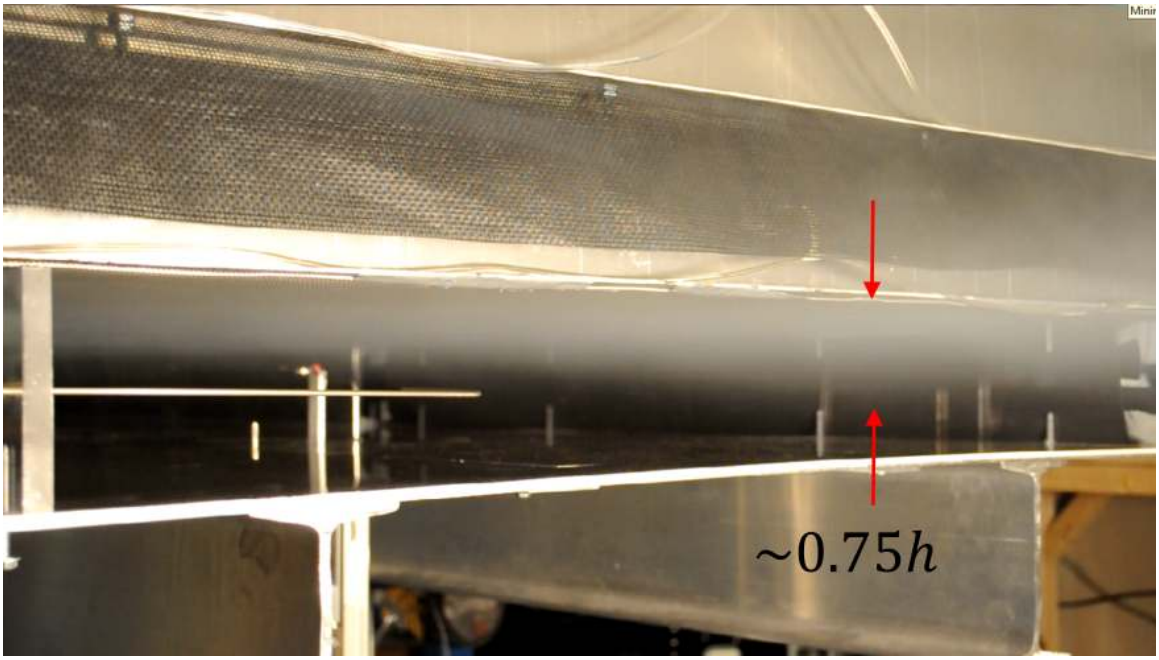

Figure 5.1: *Smoke flow visualization of blowing effects at* $U_{cl} = 4.3\ m/s$

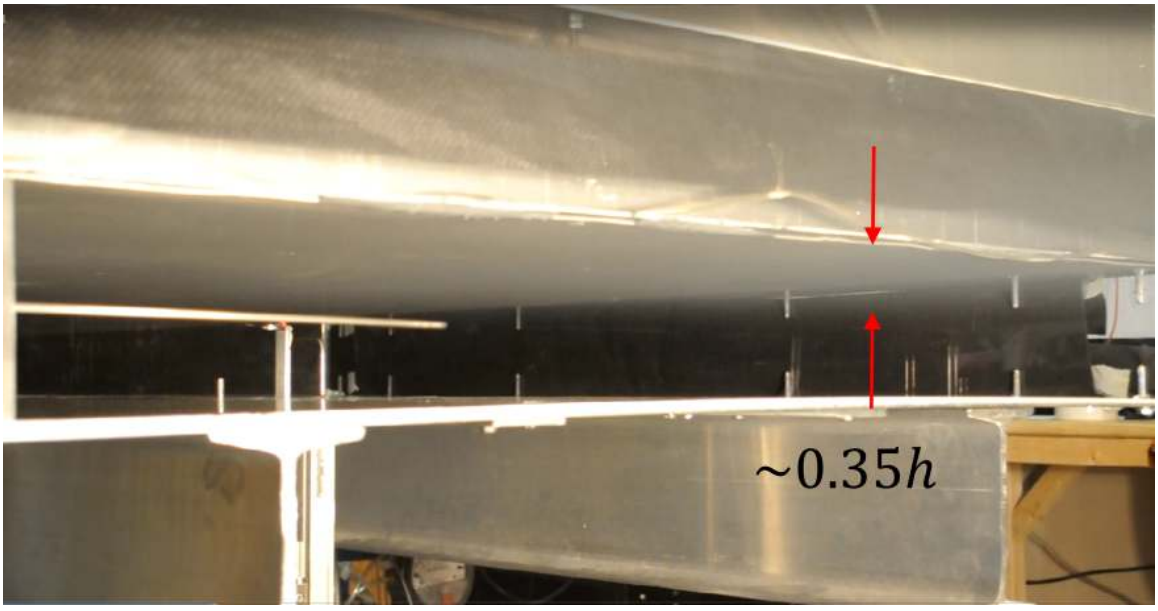

Figure 5.2: *Smoke flow visualization of blowing effects at* $U_cl = 9.2\ m/s$

This bulge eventually dissipates into the mean flow as it grows larger. Several of these bulges are seen in the images. This is visual evidence of potential modifications to the LSMs (which themselves can manifest as turbulent bulges) due to blowing and confirms some of the results seen in section 4.2, concerning the power-spectral maps.

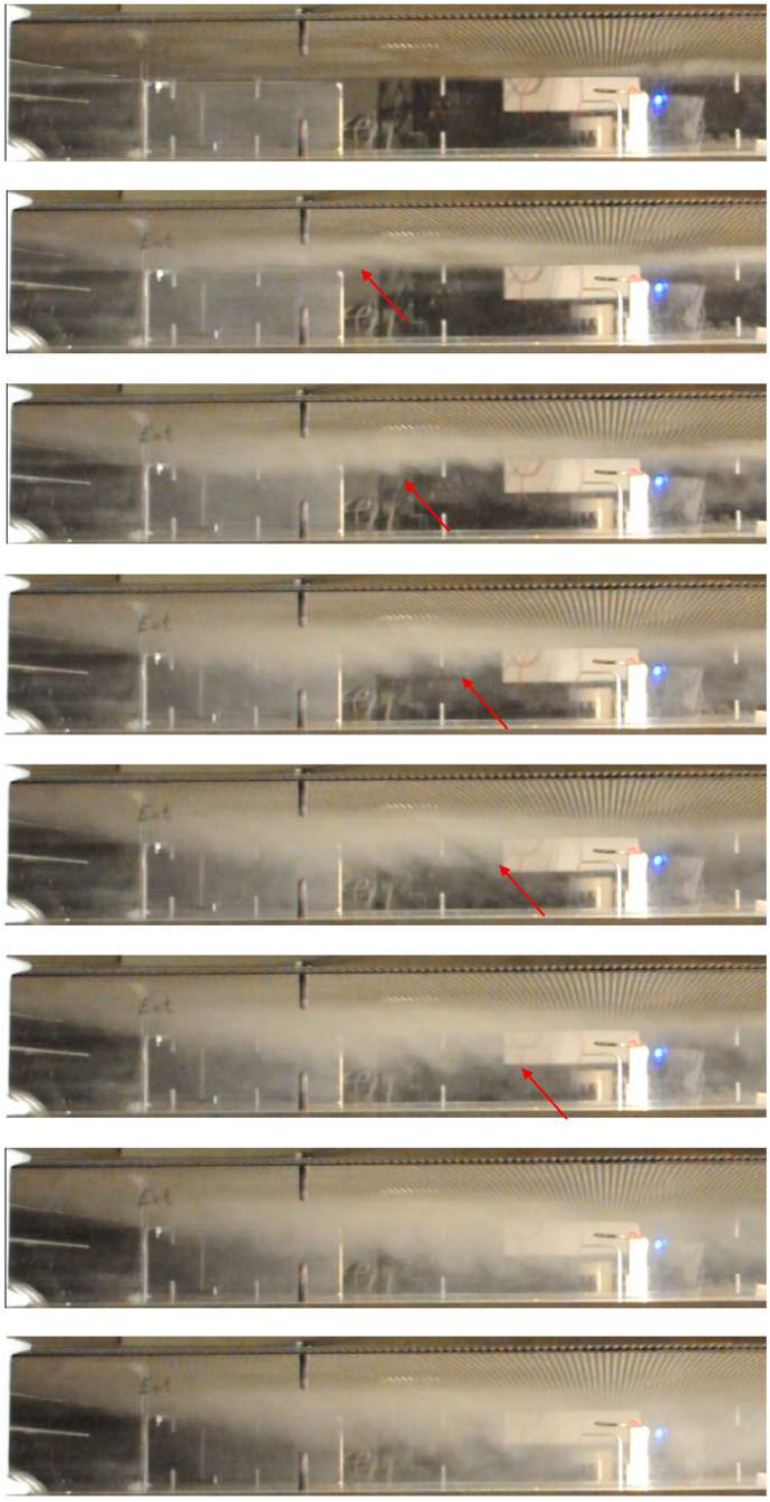

Figure 5.3: *Time-evolution of blowing effects in test section at* $U_{cl} = 0.05\ m/s$

5.2 Appendix B: Auxiliary Plots

The plots in figures 5.4, 5.5, and 5.6 demonstrate the collapse of the logarithmic portion of the wall by including the roughness function, ΔU^+.

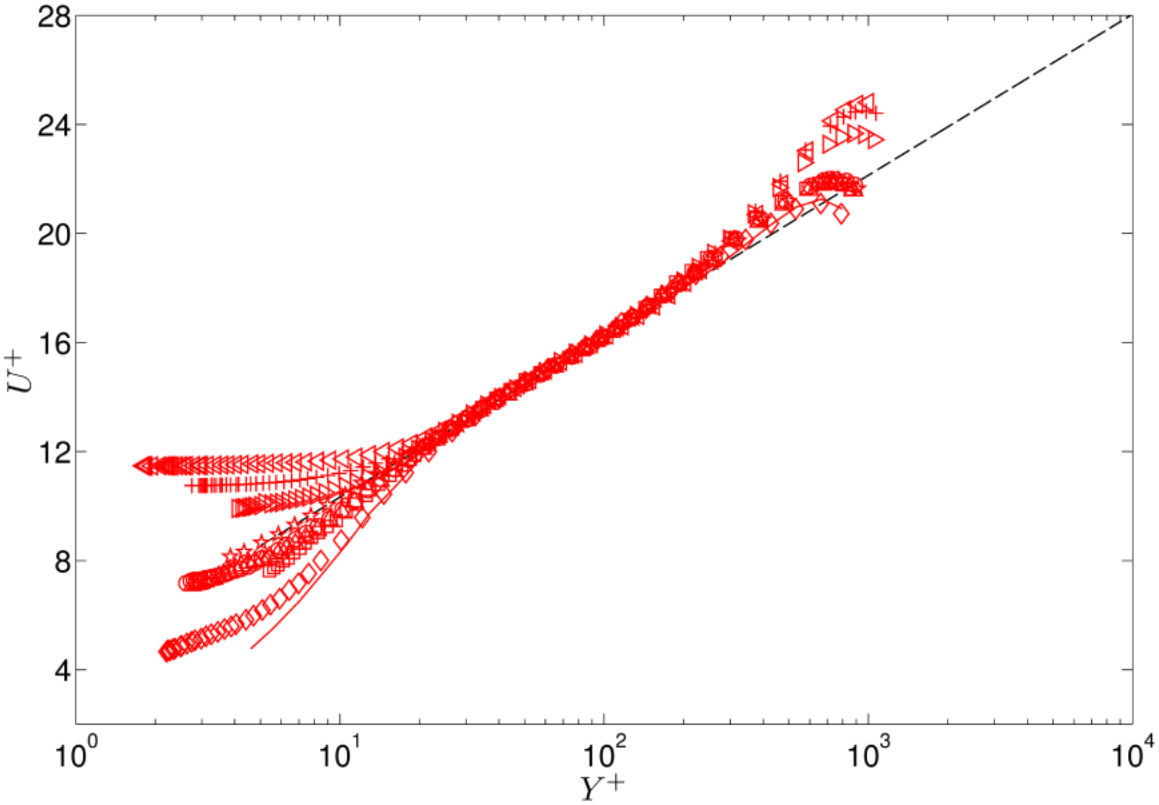

Figure 5.4: *Inner-scaled mean velocity plot with ΔU^+ shift included at $Re_\tau \approx 700$*

5.3 Appendix C: Uncertainty Analysis

To estimate the uncertainty of the hot-wire data, an error uncertainty analysis was carried out following the method outlined in Jørgensen (2002) [27].

The methodology of determining the individual uncertainties for this set of experiments is determined based upon a worse-case scenario for each Reynolds number tested. In table 5.1, the given values represent the highest speed case, for which the calculated error was the largest. Each term of table 5.1 is described in the following.

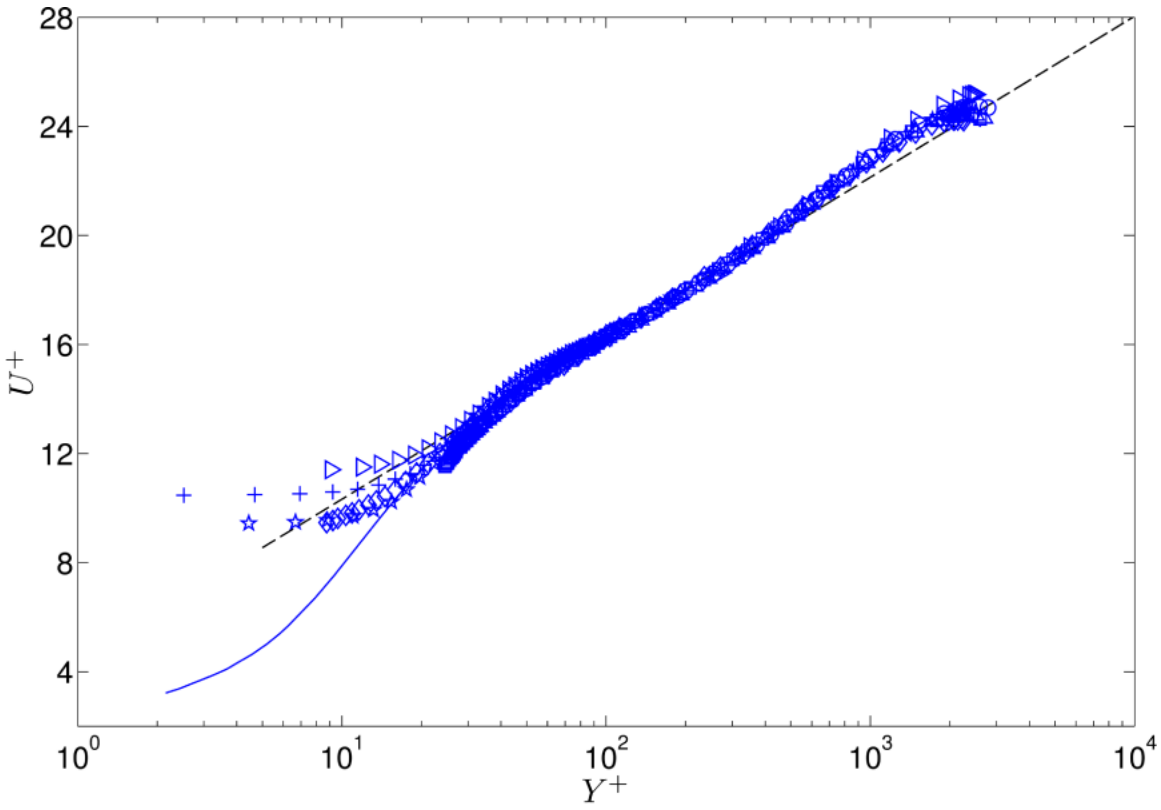

Figure 5.5: *Inner-scaled mean velocity plot with* ΔU^+ *shift included at* $Re_\tau \approx 2000$

The error due to the method of calibration is estimated to be at most 2% as given in reference [27], with

$$\Delta U_{cal} = \pm 0.02 = \pm 2\% \tag{5.1}$$

which is the relative standard uncertainty of the calibration apparatus (pitot-static tube with high-accuracy pressure transducer). The correction for linearisation occurs when a curve fit is applied to the calibration points in the form of a fourth-order polynomial. This error has a maximum value of

$$\Delta U_{fit} = \pm 0.005 = 0.5\% \tag{5.2}$$

where both the correction for the calibration equipment and the linearisation method are found as standard deviations (SDV in table 5.1).

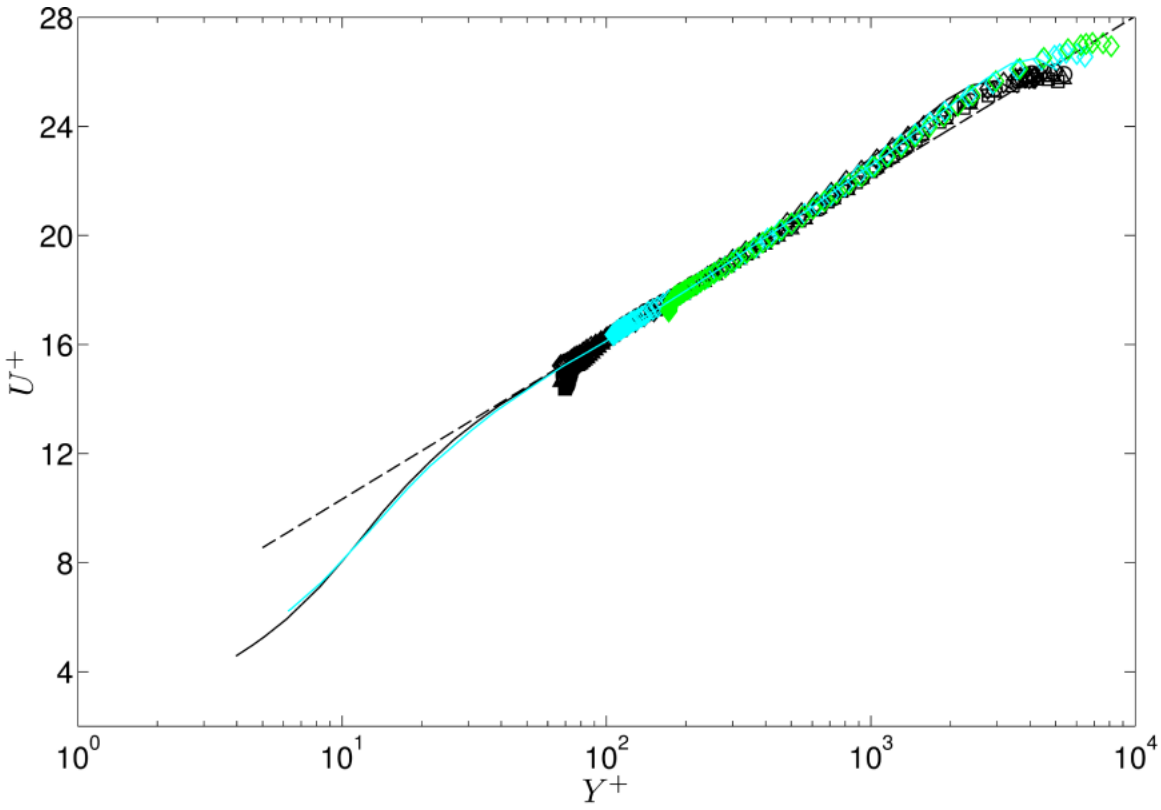

Figure 5.6: *Inner-scaled mean velocity plot with* ΔU^+ *shift included at* $Re_\tau \geq 4000$

The data acquisition system (DAQ) also has an associated error due to its limited resolution. In the formulation given, E_{AD} is the input voltage range, n is the resolution in bits, and $\partial U/\partial E$ is the slope of the inverse calibration curve near the velocity of interest.

The probe position error is not explicitly known, but it is estimated to accurately be within 1° of the streamwise direction, and hence the error due to mis-alignment is

$$1 - cos(1°) \tag{5.3}$$

Finally the maximum measured temperature variation over an entire run period was measured to be 1° Celsius, and was often much lower (0.5° C).

To determine the actual standard uncertainty, the following equation is used

Table 5.1: Uncertainty Analysis

Source of Uncertainty	Input Variants	Value	Variation Calculation	Relative Uncertainty	Coverage Factor
Calibrator	ΔU_{cal}	$\pm 2\%$	$2SDV(\Delta U_{cal})$	0.04	2
Linearisation	ΔU_{fit}	$\pm 0.5\%$	$2SDV(\Delta U_{fit})$	0.01	2
DAQ Resolution	E_{AD} n $\partial U/\partial E$	10 V 16 bit $1.32E^{-4}$ V	$\frac{E_{AD}\partial U}{U*2^n}$ $\frac{\partial U}{\partial E}$	$9.1202E-4$	$\sqrt{3}$
Probe Position	θ	1°	$1-cos(\theta)$	$1.523E^{-4}$	$\sqrt{3}$
Temperature Variations	ΔT	2°C	$\frac{\Delta T}{273}$	0.0073	$\sqrt{3}$

$$U(U_{sample}) = 2\sqrt{\sum \left(\frac{Relative\ Uncertainty}{k}\right)^2} \tag{5.4}$$

where k is known as the "coverage factor" and is given for each individual uncertainty in table 5.1. The value of $U(U_{sample})$ is the aggregated "Relative Expanded Uncertainty" and collectively characterizes the worst case error scenario. Because all hot-wire probes were calibrated in a similar method, the error analysis was performed on the data set with the most variation between pre- and post-calibrations. This was the $Re_\tau \approx 6,700$ case (highest roughness only Reynolds number). The maximum calibrated velocity varied by 2% over the course of the experiment. In figure 5.7, the error percentage calculated with the method described above is plotted. As is readily evident, the error decreases drastically with increasing velocity. This is mainly due to the thermal nature of the probe itself, as natural convection dominates the heat transfer from the probe at low velocities.

Figure 5.7 indicates that the error for most of our flows is 2% unless the measured velocity is below ≈ 3 m/s. This error has been generalized for the worse case scenario as follows by using a maximum error of 7% for flow velocities of $U < 3$ m/s, and 2% for $U > 3$ m/s.

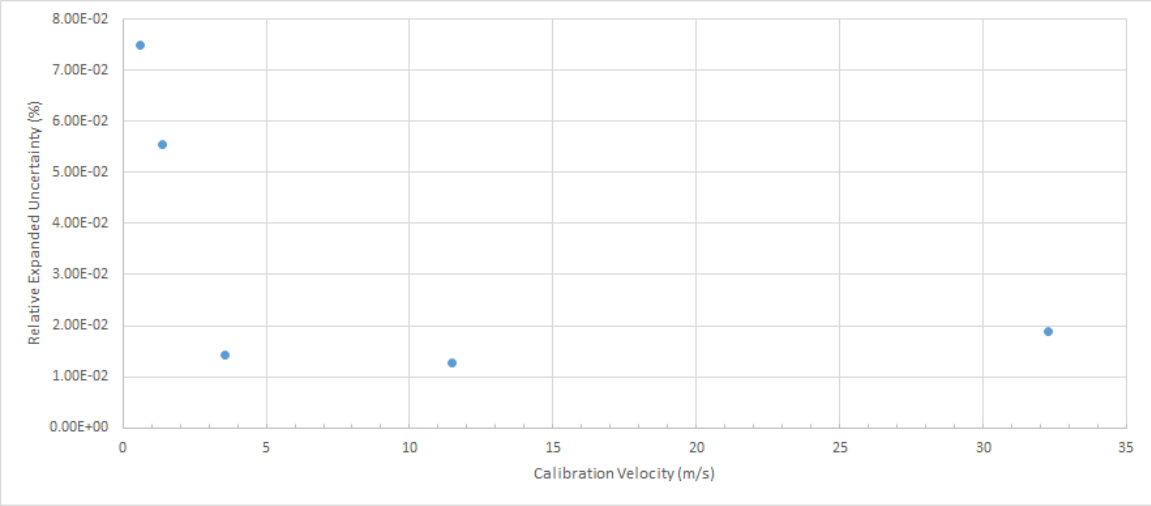

Figure 5.7: *Relative Expanded Uncertainty for the test case with the largest variability between pre- and post-calibration at* $Re_\tau \approx 6,700$.

Bibliography

[1] Akinlade, O., Bergstrom, D., Tachie, M., and Castillo, L. Outer flow scaling of smooth and rough wall turbulent boundary layers. *Experiments in Fluids*, 37:604–612, 2004.

[2] Antonia, R. and Atkinson, J. *High order moments of Reynolds shear stress fluctuations in a turbulent boundary layer*. Department of Mechanical Engineering, University of Sydney, 1972.

[3] Antonia, R. and Åge Krogstad, P. Turbulence structure in boundary layers over different types of surface roughness. *Fluid Dynamics Research*, 28.2:139–157, 2001.

[4] Bailey, S. C. C., Kunkel, G. J., Hultmark, M., Vallikivi, M., Hill, J. P., Meyer, K. A., Tsay, C., Arnold, C. B., and Smits, A. J. Turbulence measurements using a nanoscale thermal anemometry probe. *J. Fluid Mech.*, 663:160–179, 2010.

[5] Bailey, S., Hultmark, M., Smits, A., and Schultz, M. Azimuthal structure of turbulence in high Reynolds number pipe flow. *J. Fluid Mech.*, 615:121–138, 2008.

[6] Baker, R. and Launder, B. The turbulent boundary layer with foreign gas injection-i. measurements in zero pressure gradient. *International Journal of Heat and Mass Transfer*, 17.2:275–291, 1974.

[7] Bakken, O., Krogstad, P., Ashrafian, A., and Andersson, H. Reynolds number effects in the outer layer of the turbulent flow in a channel with rough walls. *Phys. Fluids*, 17, 2005.

[8] Balakumar, B. J. and Adrian, R. J. Large- and very-large-scale motions in channel and boundary-layer flows. *Phil. Trans. R. Soc. A*, 365:665–681, 2007.

[9] Çuhadaroğlu, B., Akansu, Y. E., and Ömür Turhal, A. An experimental study on the effects of uniform injection through one perforated surface of a square cylinder on some aerodynamic parameters. *Experimental Thermal and Fluid Science*, 31:909–915, 2007.

[10] Chin, C. C., Hutchins, N., Ooi, A. S. H., and Marusic, I. Use of direct numerical simulation (DNS) data to investigate spatial resolution issiues in measurements of wall-bounded turbulence. *Meas. Sci. Technol*, 20(11):115401, 2009.

[11] Chung, Y. M. and Sung, H. J. Initial relaxation of spatially evolving turbulent channel flow with blowing and suction. *AIAA Journal*, 39(11):2091–2099, 2001.

[12] Clauser, F. The turbulent boundary layer. *Advanced Applied Mechanics*, 4:1–51, 1956.

[13] Dean, R. Reynolds number dependence of skin friction and other bulk flow variables in two-dimensional rectangular duct flow. *ASME J. Fluid Eng.*, 100:215, 1978.

[14] Dey, S. and Nath, T. K. Turbulence characteristics in flows subjected to boundary injection and suction. *Journal of Engineering Mechanics*, 136(7):877–888, 2010.

[15] Dirling, R. A method for computing rough wall heat transfer rates on reentry nosetips. In *AIAA Paper 73-763, AIAA 8th Thermophysics Conference, Palm Springs, California*, 1973.

[16] Estejab, B. An investigation of the reynolds number dependence of the near-wall peak in canonical wall bounded turbulent channel flow. Master's thesis, University of Kentucky, 2011.

[17] Flack, K. A., Schultz, M. P., and Shapiro, T. A. Experimental support for townsends reynolds number similarity hypothesis on rough walls. *Physics of Fluids*, 17:035102, 2005.

[18] Guala, M., Hommema, S. E., and Adrian, R. J. Large-scale and very-large-scale motions in turbulent pipe flow. *J. Fluid Mech.*, 554:521–542, 2006.

[19] Haddad, M., Labraga, L., and Keirsbulck, L. Turbulence structure downstream of a localized injection in a fully developed channel flow. *Journal of Fluids Engineering*, 128:611–617, 2006.

[20] Healzer, J. M., Moffat, R., and Kays, W. The turbulent boundary layer on a rough, porous plate: experimental heat transfer with uniform blowing. Technical Report HMT-18, Stanford University CA Thermosciences Division, 1974.

[21] Holden, M., Bergman, R., Harvey, J., Duryea, G., and Moselle, J. Studies of the structure of attached and separated regions of viscous/inviscid interaction and the effects of combined surface roughness and blowing in high reynolds number hypersonic flows. Technical Report CUBRC-88682, Calspan UB Research Center Buffalo NY, 1988.

[22] Hoyas, S. and Jiménez, J. Scaling of the velocity fluctuations in turbulent channels up to $Re_\tau = 2003$. *Phys. Fluids*, 18(1):011702, 2006.

[23] Hultmark, M., Ashok, A., and Smits, A. A new criterion for end-conduction effects in hot-wire anemometry. *Measurement Science and Technology*, 22.5:055401, 2011.

[24] Hutchins, N. and Marusic, I. Large-scale influences in near-wall turbulence. *Phil. Trans. R. Soc. A*, 365:647–664, 2007.

[25] Hutchins, N., Nickels, T. B., Marusic, I., and Chong, M. S. Hot-wire spatial resolution issues in wall-bounded turbulence. *Journal of Fluid Mechanics*, 635:103–136, 2009.

[26] Jiménez, J. Turbulent flows over rough walls. *Annu. Rev. Fluid Mech.*, 36:173–196, 2004.

[27] Jørgensen, F. *How to measure turbulence with hot-wire anemometers-a practical guide*. Dantec Dynamics, P.O. Box 121, Tonsbakken 16-18, DK-2740 Skovlunde, Denmark, 01 2002.

[28] Kármán, T. V. Mechanische änlichkeit und turbulenz. *Nachrichten von der Gesellschaft der Wissenschaften zu Göttingen, Mathematisch-Physikalische Klasse*, pages 58–76, 1930.

[29] Kasagi, N. Progress in direct numerical simulation of turbulent transport and its control. *International Journal of Heat and Fluid Flow*, 19:125–134, 1998.

[30] Kim, K. C. and Adrian, R. J. Very large-scale motion in the outer layer. *Phys. Fluids*, 11(2):417–422, 1999.

[31] Kornilov, V. Distribution of mean velocity in turbulent boundary layer over permeable surface with air blowing. *Thermophysics and Aeromechanics*, 19.1:9–16, 2012.

[32] Krogstad, P.-Å., Antonia, R., and Browne, L. Comparison between rough- and smooth-wall turbulent boundary layers. *J. Fluid Mech.*, 245:599–617, 1992.

[33] Krogstad, P.-Å. and Kourakine, A. Some effects of localized injection on the turbulence structure in a boundary layer. *Physics of Fluids*, 12(11):2990–2999, 2000.

[34] Kunkel, G. and Marusic, I. Study of the near-wall-turbulent region of the high-reynolds-number boundary layer using an atmospheric flow. *J. Fluid Mech.*, 548:375–402, 2006.

[35] Laws, E. and Livesey, J. Flow through screens. *Annu. Rev. Fluid Mech.*, 10:247–266, 1978.

[36] Leonardi, S., Orlandi, P., Smalley, R., Djenidi, L., and Antonia, R. Direct numerical simulations of turbulent channel flow with transverse square bars on one wall. *Journal of Fluid Mechanics*, 491:229–238, 2003.

[37] Ligrani, P. and Bradshaw, P. Subminiature hot-wire sensors: development and use. *J. Phys. E: Sci. Instrum.*, 20:323–332, 1987.

[38] Mills, A. and Huang, X. On the skin friction coefficient for a fully rough flat plate. *J. Fluid Eng.*, 105:364–365, 1983.

[39] Monkewitz, P., Duncan, R., and Nagib, H. Correcting hot-wire measurements of stream-wise turbulence intensity in boundary layers. *Phys. Fluids*, 22:091701, 2010.

[40] Monty, J. P. *Developments in Smooth Wall Turbulent Duct Flows*. PhD thesis, University of Melbourne, 2005.

[41] Monty, J. P., Stewart, J. A., Williams, R. C., and Chong, M. Large-scale features in turbulent pipe and channel flows. *J. Fluid Mech.*, 589:147–156, 2007.

[42] Monty, J., Hutchins, N., Ng, H., Marusic, I., and Chong, M. A comparison of turbulent pipe, channel and boundary layer flows. *J. Fluid Mech.*, 632:431–442, 2009.

[43] Nagib, H. M. and Chauhan, K. A. Variations of von kármán coefficient in canonical flows. *Physics of Fluids*, 20:101518, 2008.

[44] Nikitin, N. and Pavel'ev, A. Turbulent flow in a channel with permeable walls. direct numerical simulation and results of three-parameter model. *Fluid Dynamics*, 33(6):826–832, 1998.

[45] Nikuradse, J. Laws of flow in rough pipes. *Washington: National Advisory Committee for Aeronautics*, 1950.

[46] Perry, A. and Abell, C. Asymptotoic similarity of turbulence structures in smooth- and rough-walled pipes. *Journal of Fluid Mechanics*, 79(04):785–799, 1977.

[47] Perry, A. and Joubert, P. Rough-wall turbulent boundary layers. *Journal of Fluid Mechanics*, 37:383–413, 1969.

[48] Perry, A. and Li, J. Experimental support for the attached-eddy hypothesis in zero-pressure gradient turbulent boundary layers. *Journal of Fluid Mechanics*, 218:405, 1990.

[49] Perry, A., Lim, K., and Henbest, S. An experimental study of the turbulence structure in smooth- and rough-wall boundary layers. *J. Fluid Mech.*, 177:437–466, 1986.

[50] Pope, S. B. *Turbulent Flows*. Cambridge University Press, 2000.

[51] Prandtl, L. Report on investigation of developed turbulence. Technical report, NACA Report TM-1231, 1925.

[52] Prandtl, L. and Schlichting, H. Das wiederstandagesetz rouher platten. *Werft Reederer Hafen*, 15:1–4, 1934.

[53] Prandtl, L. Über flüssigkeitsbewegung bei sehr kleiner reibung. *Int. Math. Kongr Heidelberg, Leipzig*, 1904.

[54] Raupach, M. R., Antonia, R., and Rjagopalan, S. Rough-wall turbulent boundary layers. *Appl. Mech. Rev.*, 44:1–25, 1991.

[55] Reynolds, O. An experimental investigation of the circumstances which determine whether the motion of water shall be direct or sinuous, and the law of resistance in parallel channels. *Proceedings of the Royal Society of London*, 35(224-226):84–99, 1883.

[56] Reynolds, O. On the dynamical theory of incompressible viscous ffluid and the determination of the criterion. *Philosophical Transactions of the Royal Society of London*, 186:123–164, 1895.

[57] Schetz, J. A. and Nerney, B. Turbulent boundary layer with injection and surface roughness. *AIAA Journal*, 15.9:1288–1294, 1977.

[58] Schlatter, P. and Örlü, R. Assessment of direct numerical simulation data of turbulent boundary layers. *J. Fluid Mech.*, 659:116–126, 2010.

[59] Schultz, M. and Flack, K. The rough wall-turbulent boundary layer from the smooth to the fully rough regime. *J. Fluid Mech.*, 580:381–405, 2007.

[60] Segalini, A., Örlü, R., Schlatter, P., Alfredsson, P., Rüedi, J.-D., and Talamelli, A. A method to estimate turbulence intensity and transverse taylor microscale in turbulent flows from spatially averaged hot-wire data. *Exp. Fluids*, 51:693–700, 2011.

[61] Simpson, R. A generalized correlation of roughness density effects on the turbulent boundary layer. *AIAA Journal*, 11:242–244, 1973.

[62] Smits, A. J., Monty, J. P., Hultmark, M., Bailey, S. C. C., Hutchins, N., and Marusic, I. Spatial resolution correction for wall-bounded turbulence measurements. *J. Fluid. Mech*, 676:41–53, 2011.

[63] Sumitani, Y. and Kasagi, N. Direct numerical simulation of turbulent transport with uniform wall injection and suction. *AIAA Journal*, 33:1220, 1995.

[64] Tavoularis, S. *Measurement in Fluid Mechanics*. Cambridge University Press, 2005.

[65] Townsend, A. A. *The Structure of Turbulent Shear Flow*. Cambridge University Press, Cambridge, UK, 1976.

[66] Vigdorovich, I. and Oberlack, M. Analytical study of turbulent poiseuille flow with wall transpiration. *Physics of Fluids*, 20:055102, 2008.

[67] Voisinet, R. Influence of roughness and blowing on compressible turbulent boundary layer flow. Technical report, Naval Surface Weapons Center, White Oak Lab, Silver Spring, MD, June 1979.

[68] Zanoun, E. S., Durst, F., and H., N. Evaluating the law of the wall in two-dimensional fully developed turbulent channel flows. *Phys. Fluids*, 15:3079–3089, 2003.

[69] Zhou, J., Adrian, R. J., Balachandar, S., and Kendall, T. M. Mechanisms for generating coherent packets of hairpin vortices in channel flows. *J. Fluid Mech.*, 387:353–396, 1999.

Mark A. Miller

EDUCATION

B.S. Department of Mechanical Engineering
University of Kentucky
Lexington, Kentucky, USA,
August 2011

HONORS AND AWARDS

2012 NASA Space Technology Research Fellow (NSTRF) at University of Kentucky

2011 University of Kentucky College of Engineering Leadership Class Invitee

2011 NASA Kentucky EPSCOR Space Grant Recipient

RESEARCH POSITIONS

June 2012-Aug. 2012 NASA Student Internship
Ames Research Center, Mountain View CA

Aug. 2011-May 2012 Graduate Research Assistant
Experimental Fluid Dynamics Laboratory, Lexington KY.

May 2010-Aug. 2011 Undergraduate Research Assistant
Experimental Fluid Dynamics Laboratory, Lexington KY.

Summer 2009, 2010 Mechanical Engineering Internship
Lexmark International, Lexington KY

PUBLICATIONS

Zhang, H.B., Miller, M.A., Bailey, S.C.C., Martin, A., (2013) "Investigation of Turbulent Structure Modification by Momentum Injection Into Turbulent Flow Over a Rough Surface" accepted for publication, 51st AIAA Aerospace Sciences Meeting, January 7-10, Grapevine, Texas.

Miller, M.A., Martin, A., Bailey, S.C.C., (2012) "Investigation of Turbulent Structure Modification by Momentum Injection Into Turbulent Flow Over a Rough Surface" 65th APS Annual Division of Fluid Dynamics Meeting, November 18-20, San Diego, California.

Miller, M.A., Zhang, H.B., Martin, A., Bailey, S.C.C., (2012) "Investigation of Blowing Effects on Turbulent Flow Over a Rough Surface" 37th AIAA Dayton-Cincinnati Aerospace Sciences Symposium, March 5, Dayton, Ohio.

Miller, M.A., Bailey, S.C.C., Martin, A., (2012) "Experimental Investigation of Blowing Effects on Turbulent Flow Over a Rough Surface" 5th AFOSR/NASA Ablation Workshop, February 28-March 1, Lexington, Kentucky.

Miller, M.A., Bailey, S.C.C. and McDonough, J.M. (2011) "Experimental Investigation of the Instantaneous Connection Between Freestream Turbulence Wavenumber and Klebenoff Modes During Bypass Transition" 2011 KIEC - KY EPSCoR Joint Conference, Louisville, Kentucky.